EXPERIMENTAL EVALUATION OF LOW-COST, PORTABLE, AND RAPID NONDESTRUCTIVE EVALUATION METHODS FOR TIMBER DISTRIBUTION POLES

by

Erica Barber

A thesis submitted to the faculty of
The University of North Carolina at Charlotte
in partial fulfillment of the requirements
for the degree of Masters of Science in
Civil Engineering

Charlotte

2016

Approved by:

_____
Dr. Matthew J. Whelan

_____
Dr. David Young

_____
Dr. Janos Gergely

ABSTRACT

ERICA BARBER. Experimental evaluation of low-cost, portable, and rapid nondestructive evaluation methods for timber distribution poles. (Under the direction of DR. MATTHEW J. WHELAN)

Power line workers have long been required to climb timber utility poles to perform maintenance. Although routine pole inspection and maintenance programs are in place to optimize asset management and reduce the risk posed to workers, such work continues to be dangerous. Conventionally, power line workers have conducted visual and manual inspections on timber utility poles prior to performing maintenance, but these inspection practices have been found to be unreliable. Nondestructive evaluation methods have been developed in attempt to improve the accuracy of these pre-maintenance inspections, but these methods often require costly specialized equipment as well as extensive analysis to determine the condition of the timber and can expose the pole to conditions leading to decay-causing fungi. This study is conducted to establish a basis for developing a low-cost, quick, portable nondestructive testing device that can be routinely utilized by power line workers to assess the safety of poles prior to accessing supported electrical infrastructure. A review of related literature is conducted and four nondestructive test methods (guided stress wave propagation, experimental modal analysis, acoustic resonance, infrared thermography) are selected for evaluation through full-scale controlled experimental tests conducted in a laboratory environment. The development of the experimental test bed, procedures used for data collection for each test method, and destructive characterization of decay below the ground line are documented. Analysis of test data is focused on vibration-

based methods for condition assessment of the timber utility poles. An analytical model of the installed timber poles is created using the Rayleigh-Ritz method and parameter identification through optimization-based model updating is pursued using two approaches to develop a method for condition assessment of the tested poles. Verification of the analytical model is conducted by comparing the predicted natural frequencies and mode shapes to experimental estimates obtained from experimental modal analysis. Additionally, the destructive profiling of section properties below the ground line is used to validate the nondestructive test results. Both parameter identification approaches are determined to be promising for the detection of severely decayed poles; however, the introduction of a parameter to explicitly model the loss of stiffness and mass from decay below the ground line is found to result in lower prediction errors and accurate estimation of section loss. Remaining challenges and recommendations for future research to promote the development of a low-cost, rapid, and portable device for condition assessment of in-service timber distribution poles are discussed.

ACKNOWLEDGEMENTS

Thank you to Duke Energy Corporation for their funding of this study and research assistantship and to my Thesis Committee, Dr. Matthew Whelan, Dr. David Young, and Dr. Janos Gergely for their support, advice, and guidance throughout every phase of this study. Thanks also to Mr. Mike Moss, Dr. Youngjin Park, Mr. Adam Howe, and Mr. Corey Rice for their assistance during the development of the experimental test bed and the installation, testing, and removal of the timber distribution poles. A final thanks to all of my family and friends who supported and encouraged me through out this process.

TABLE OF CONTENTS

LIST OF FIGURES

LIST OF TABLES

CHAPTER 1: INTRODUCTION

The history of utility poles dates back to the 1840's when the telegraph machine was developed by Samuel Morse. In 1843, Morse requested funds from Congress to install an experimental telegraph line from Baltimore, Maryland to Washington, DC. After failing to successfully install underground lines, Morse erected wood poles to carry the lines aboveground. In the years following 1844 when the experimental line was completed, timber poles were constructed throughout the country to carry telegraph, telephone, and other utility wires [Bibber, 1944]. Timber utility poles are often referred to as the backbone of the electrical distribution network and remain in widespread use with estimates of over 180 million in service timber utility poles in the United States alone [Mankowski et al., 2002].

Given that utility poles support elevated infrastructure prone to failure and obsolescence, utility workers are routinely required to climb these poles to perform maintenance work. However, accessing supported infrastructure by climbing aged poles may be dangerous because the strength of the poles could be compromised by decay and structural instability. Currently, modern bucket trucks are often utilized to safely access infrastructure on utility poles, which decreases the danger posed to workers. However, in some situations, such as when bucket trucks cannot safely reach the utility poles, power line technicians must still climb the timber poles to perform

maintenance work.

In an effort to ensure the safety of power line technicians and the resiliency of the electrical distribution network, routine pole inspection and maintenance programs have been developed by power companies and service providers to characterize the health and estimate the structural capacity of in-service poles for asset management. As a result of the large number of in-service poles, such formal inspections typically occur on a 10 year cycle, which may require workers performing maintenance on electrical infrastructure to access the tops of poles that have not been properly assessed in as long as a decade [Birtz, 1979, Daugherty, 1998, Morrell, 2016]. In an attempt to improve the safety of utility workers, the Occupational Safety and Health Administration (OSHA) has developed guidelines for assessment techniques required for workers to determine whether a pole is safe to climb prior to performing maintenance work [OSHA, 2014]. Unfortunately, a structurally unstable pole or a pole with compromised strength cannot always be detected using these conventional methods or by visual inspection. For instance, the exterior surface of a pole can crack during the drying process, exposing its interior to decay. Such decay can quickly spread without leaving visible evidence on the exterior surface, leading to unexpected structural reductions and, possibly, failure. Additionally, decay is most often found in the sections of poles below the ground line, where there is enough oxygen and moisture to create the adverse environment promoting accelerated rates of decay. Subsequently, excavation is often required before such decay can be identified in a pole [Craighead et al., 2001].

Decay in timber utility poles is the result of moisture and fungi, which can be in-

troduced to the pole through cracks that form in the pole during the drying process. Poles are usually treated with a preservative to mitigate the risk of decay-causing fungi; however, the effectiveness of the preservative is limited by time and environmental exposure. Holes in the pole such as those created by woodpeckers, termites, or conventional inspection practices can also be used as an ingress for decay-causing fungi. The sections of the pole below ground line are especially susceptible to decay because the amount of oxygen and water present below ground line creates a perfect environment for fungal development and growth [Craighead et al., 2001]. The location of decay in a cross section can be categorized into three types: shell rot, pocket rot, and heart rot. Shell rot (Figure 1.1) affects the circumference of a pole and can be identified through a visual inspection of the affected section, which is typically only possible after excavation of the soil around the pole is performed. Pocket rot (Figure 1.2) affects the interior cross section of the pole without affecting the circumference. Decayed portions of the cross section of a pole identified by soft, discolored wood are circled in Figure 1.2b with the smallest circle including a small amount of section loss. Heart rot is similar to pocket rot but occurs within the core, or the heart, of the pole. Heart rot and pocket rot are both more difficult than shell rot to identify through visual analysis.

1.1 Overview of Research Effort and Anticipated Contributions

Advanced nondestructive evaluation methods have been developed to detect decay and to profile interior section properties in utility poles and other timber structural members. However, these methods often require costly specialized equipment and

a)  b) 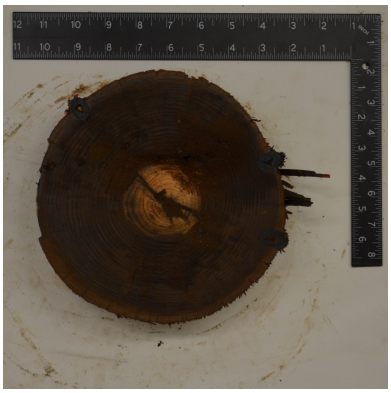 c) 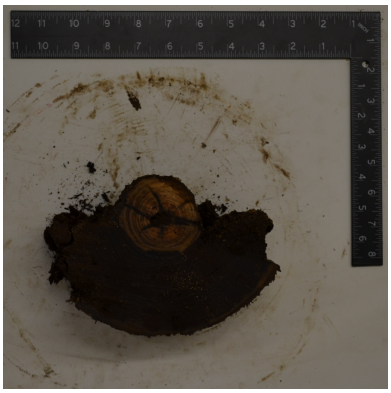

FIGURE 1.1: Typical case of shell rot decay below ground in timber distribution poles: a) exterior of pole; b) healthy cross section outside of region of decay; c) decayed cross section

a)  b)  c) 

FIGURE 1.2: Typical case of pocket rot decay below ground in timber distribution poles: a) exterior of pole; b) healthy cross section outside of region of decay; c) decayed cross section

extensive analysis to determine the condition of the timber. The purpose of this study is to identify a low-cost and portable nondestructive test method that can be quickly used by utility workers to determine the condition of a pole prior to climbing. Such a device must be easily operable, quick, and rugged and must have the ability to detect decay present in a pole below the ground line without excavating the soil around the pole.

This study evaluates nondestructive evaluation methods to determine the most promising techniques for utility workers to use to quickly and accurately assess the

condition of timber utility poles below the ground line. This study is part of a phase I research effort aimed at selecting one or more techniques to develop a cost effective, durable, and reliable portable device that utility workers can utilize to quickly determine the condition of a pole prior to climbing it to access electrical infrastructure.

The experimental test bed, procedures and test setups for four nondestructive evaluation techniques that were utilized to assess the condition of ten full-scale timber utility poles and destructive testing of the pole cross sections are documented to develop the experimental database. Analysis of test data is then focused on vibration-based methods for condition assessment using the measured natural frequencies. A Rayleigh-Ritz model is developed to analytically predict natural frequencies of timber poles embedded in elastic soil and model updating strategies are explored for detection and classification of decay below the ground line.

1.2 Organization of Thesis

The outline of this thesis is as follows:

- Chapter 1 provides an introduction to the relevance and challenges of rapid, in-service inspection of timber distribution poles.
- Chapter 2 presents a literature review on current and past nondestructive evaluation techniques utilized to assess the condition of wood structures and their applicability to timber utility poles.
- Chapter 3 provides information on the development of an experimental test bed

to assess the application of viable nondestructive testing techniques to timber poles. Test setups, instrumentation, and procedures used for each method are documented and the material properties and structural condition of the ten poles included in the experimentation are characterized through destructive testing.

- Chapter 4 describes the use of experimental modal analysis to estimate the dynamic properties of the timber pole through vibration testing. In addition, an analytical model is developed using the Rayleigh-Ritz Method to allow for rapid prediction of the natural frequencies and mode shapes of timber poles with specified material and geometric properties as well as soil foundation conditions.

- Chapter 5 presents two structural identification techniques used to assess pole health from vibration measurements by optimizing parameters in the Rayleigh-Ritz model using measured natural frequencies.

- Chapter 6 summarizes conclusions of the research effort and provides recommendations for future work in this area.

CHAPTER 2: LITERATURE REVIEW

2.1 Timber Poles in Electrical Distribution Networks

Today, there are estimates that as many as 180 million in-service timber utility poles are present in the United States for support of the nation's electrical distribution network [Mankowski et al., 2002]. Southern pine, first used in the 1890's, has been one of the most prevalent species used for wood poles in the U.S., comprising 75% of the nearly 4 million poles produced in 1990 (Figure 2.1) [Birtz, 1979]. Despite its popularity, southern pine is predominantly used for poles that are less than 60 feet in height. Situations requiring taller poles generally utilize tree species that are more easily available in greater heights, such as Douglas fir or western red cedar [Crosby, 2011].

Wood in general is a orthotropic material, meaning that the mechanical properties of wood are dependent on the orientation of the wood grain. For instance, one publication by the United States Federal Highway Administration (FHWA) specifies southern yellow pine structural properties to range from 221 MPa to 18,345 MPa for elastic modulus and from 0.078 to 0.291 for Poisson ratio, depending on both moisture content and grain direction [Murray, 2007]. When conducting structural analysis on a wood structure, grain orientation must be taken into account due to the large variance in mechanical properties such as elastic modulus. Likewise, the applica-

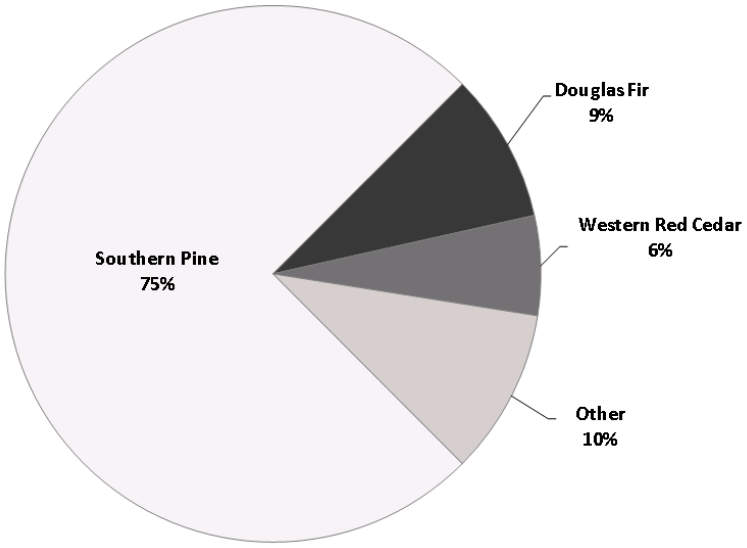

FIGURE 2.1: Percentages of tree species used for distribution poles in 1990

tion of many conventional nondestructive evaluation techniques on timber structural elements presents challenges due to the orthotropic nature of the material.

Across the range of the timber utility poles used in service today, those utilized for the support of distribution lines typically range from 35 to 50 feet in height [SCS, 2013, Daniels and Jones, 2009]. Important wood distribution pole characteristics, such as height, diameter, and species, are governed by the American National Standards Institute Standard O5.1 [ANSI, 2015]. However, individual utility companies will often exceed the ANSI O5.1 design minimums. Similarly, the American Wood Protection Association (AWPA) provides specifications for acceptable wood preservative characteristics [Morrell, 2016]. Preservatives have been used for decades to treat wood prior to utility pole installation in order to enhance the durability of the wood to environmentally driven decay. According to a 2002 survey of 244 utility companies, Pentachlorophenol (Penta), Chromated Copper Arsenate (CCA), and Creosote are reported to be the most popular preservatives used. The preservatives were re-

portedly used on 63%, 16%, and 16%, respectively, of the 42 million in service poles surveyed [Mankowski et al., 2002]. The development of wood preservatives began in the early 1700s, with Creosote treatments patented in 1836 [Freeman et al., 2003] and largely the most prevalent wood preservative used for decades. Penta production began in the United States around 1930 and CCA was first patented in 1938 but their widespread use as a preservation treatment for timber utility poles did not begin for several more decades. Today, the installed poles that are of most concern are those reaching the end of their useful lifespan. Many utility companies consider the service life of utility poles to be 30 to 40 years, therefore the poles of most concern today are those typically treated with Creosote [Morrell, 2016].

2.1.1 Structural Design Requirements and Failure Criteria

All utility poles must be structurally capable of supporting the loads from electrical components, including insulators, transformers, communication lines, and mechanical devices used to support the electrical infrastructure, such as crossarms. Additionally, utility poles must be capable of resisting often significant wind and ice loads specific to the installation region. When combined with safety factors, the loads from electrical and weather components develop the required strength for design of a utility pole. During the initial design process, the American National Standard Institute's (ANSI) O5.1 document specifies pole load-carrying capacites based on pole classes, which it also specifies based on pole species, dimensions, and tolerances [Crosby, 2011].

Criteria for condition assessment of timber distribution poles is also specified in design codes and is based on a comparison of the estimated nominal strength of the

pole accounting for deterioration relative to the initial strength. In accordance with the National Electrical Safety Code (NESC), the nominal strength should not be less than 2/3 of its original value for an in service utility pole located in an area with combined ice and wind district loading [Potvin, J., 2014]. Similarly, in areas with extreme wind or extreme ice with concurrent wind loading, a stricter criteria limits the reduced strength to no less than 3/4 of the original value [RUS, 2013]. If the estimated strength of a deteriorated utility pole is assessed to be less than the minimum allowable value, measures should be taken to replace the pole or to improve the strength of the pole through retrofitting.

Section loss from decay is the most common reason for the reduction in structural capacity of a timber distribution pole over its service life. Poles are normally treated with preservatives to mitigate the risk of decay-causing fungi, but cracks often form during drying after being treated, which can expose the unpreserved center of the pole to agents causing decay. Furthermore, ingress of moisture and fungi leading to decay may be introduced into a pole already installed through holes such as those created by woodpeckers, termites, or conventional inspection practices. Decay is often found in sub-grade portions of poles that are at a point below the ground line where the amount of oxygen and water create a perfect environment for fungi to develop and grow [Craighead et al., 2001].

2.1.2 Conventional Inspection Practice

Utility pole inspection and maintenance programs are in place to routinely determine the structural condition of in service timber utility poles. Formal inspection

procedures often include the excavation of the soil around the pole, which allows for an inspection of the pole below-grade where rot and decay are most prevalent. When significant excavation occurs, approximately 99% of structurally deficient wood poles are detected by conventional inspection practice [Daugherty, 1998]. However, despite the effectiveness of conventional inspection practices, periodic inspections are often based on a 10 year cycle [Birtz, 1979, Daugherty, 1998, Morrell, 2016]. This length interval between inspections is a result of the extensive number of poles in-service and the limited resources available to provide more frequent inspection. As a result of such a long inspection interval, distribution poles are susceptible to the development of adverse structural conditions that may pose a risk to linemen servicing electrical components supported by these poles.

When utility poles are serviced between inspections, linemen utilize relatively crude nondestructive inspection techniques prior to beginning maintenance work on the pole. Typically, these inspections are visual and manual. Visually, the above-grade portion of the pole is examined for the presence of cracks or splits, holes, insect damage, decay, and other forms of damaged wood [RUS, 2011]. In some cases, samples from an increment borer may also be examined visually to determine the condition of the wood in the interior of the pole. Manual examinations include using a screwdriver or pole prod to test the pole at the ground line for decay, along with what is known as the tap or hammer test. The combined use of hammer tests and prodding is commonly known as "sound and bore" testing. According to the Occupational Safety & Health Administration (OSHA), the utility pole should be rapped sharply with a 3 pound hammer starting near ground level and extending approximately 6 feet up

the pole during the sounding test. The condition assessment for this hammer test is performed subjectively by the lineman by listening to the acoustic waves developed during the hammer impact on the pole surface. When striking sound wood, the hammer rebounds more and produces a clearer sound than when hitting an area with internal decay. OSHA also recommends a mechanical rocking test, which involves the utilization of pike pole or rope to apply a horizontal force to the pole and rock it back and forth in a direction perpendicular to the line. The utility pole is considered unsafe if it cracks during the rocking test [OSHA, 2014].

When combining visual examinations, bore tests, and hammer tests, poles with unacceptable levels of decay have been found in one study to be effective only about 60% of the time unless excavation of the soil around the pole is performed. Additionally, when solely utilizing visual examinations and hammer tests to determine the condition of a pole, this study indicates that the findings are "almost worthless" [Daugherty, 1998]. Despite the limited reliability of the "sound and bore" method for pole inspection performed by linemen prior to servicing electrical infrastructure supported by timber poles, these techniques remain prevalent in use. The reason for this reliance on the methods is that, to date, no proven nondestructive evaluation technique or commercial system has been developed for inspection of timber poles that is rapid enough to perform that it does not present a burden on the lineman, simple enough to perform that it does not require an engineer or trained inspector, and low enough in cost that it can be provided to entire fleets of maintenance personnel.

2.2 Nondestructive Evaluation (NDE) of Structural Timber

Several nondestructive evaluation methods have been developed for assessing the condition and estimating the remaining strength of in-service utility poles. Through the utilization of sonic and ultrasonic waves, microdrills, and even x-rays, existing technologies can evaluate the physical properties of wood, which in turn can be analyzed to estimate the strength of a deteriorated utility pole without requiring the excavation of the soil around the pole. The principles behind these nondestructive evaluation techniques will be reviewed here to summarize the current state of the art and to identify key challenges that must be overcome to produce a rapid and low-cost system for pole inspection.

2.2.1 Formal Inspection Programs

Typically, formal inspections include sounding, boring, and excavation. Sounding is conducted by striking the pole with a short mallet and listening for any indications of decay. Boring is then conducted using a increment borer or resistograph to profile section loss within the cross section of the pole in areas subject to decay as detected by sounding. Excavation is useful for visually observing and measuring external shell rot below the ground line. However, it should be noted that both boring and excavation can introduce or accelerate decay in the pole by penetrating its preservative layer or by disturbing its surrounding environment. The purpose of these visual and semi-destructive inspection practices is to obtain an estimate of the extent of decay in the cross section, from which an equivalent reduced circumference of the pole can be estimated by utilizing references similar to Figure 2.2 and Tables 1, 2, and 3,

which are often provided by utility companies. Once the reduced circumference of a deteriorated pole is estimated, it is compared to its original circumference in order to determine the remaining safety factor of the pole (Table 4). As a safety factor of 4 is typically integrated into the design process of timber utility poles, the safety factor associated with the reduced circumference should not be less than 2.65 in areas with combined ice and wind district loading in accordance with the NESC. Similarly, the nominal safety factor estimated for an in-service pole should not be less than 3 in areas with extreme ice with concurrent wind loading. Numerous nondestructive evaluation tools directed towards enhancing formal inspection programs have been commercialized and were recently evaluated by the Electric Power Research Institute [Potvin, J., 2014] with various levels of success. The remainder of this literature review is directed towards low-cost, rapid, and portable methods suitable for use by a lineman and not necessarily tailored to formal inspection programs.

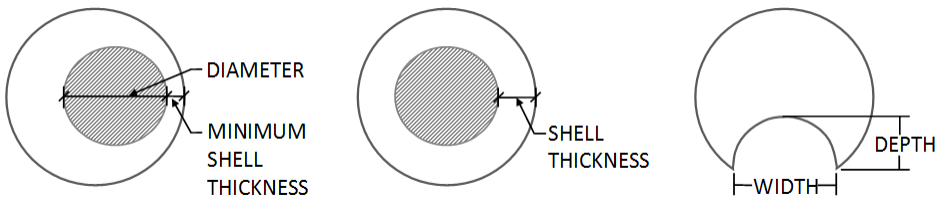

FIGURE 2.2: Measurement of internal pocket decay (left), heart rot (middle), and external pocket decay (right)

2.2.2 Mechanical Stress Wave Propagation

Mechanical stress wave propagation methods utilize the measurement of signal characteristics from sonic or ultrasonic stress waves resulting from an impulsive force or surface deformation applied to material under test. Sonic stress waves are generated

Table 1: Equivalent reduction in circumference of 30 to 40 inch circumference poles for internal pocket decay [RUS, 2013, Bureau of Reclamation, 1992]

Pocket Diameter (in)	**Minimum Shell Thickness (in)**	**Reduction in Circumference (in)**
3	1	2
	2	1
	3	1
4	1	3
	2	1
	3	1
5	1	4
	2	2
	3	1

Table 2: Equivalent reduction in circumference of 30 to 40 inch circumference poles for heart rot [RUS, 2013, Bureau of Reclamation, 1992]

Measured Shell Thickness (in)	**Reduction in Circumference (in)**
3	2
3.5	1
4	0
4.5	0

by a mechanical impact, usually produced by a hammer, and are audible to the human ear with frequencies between 10 and 20 kilohertz [Krautkrämer and Krautkrämer, 2013]. Ultrasonic stress waves are similar to sonic stress waves, but have shorter wavelengths and higher frequencies and are generated using a piezoelectric transducer. When an impact excitation is applied, the local displacement travels through the wood in the form of compressive waves (P-waves), shear waves (S-waves), surface waves (Rayleigh waves), and bending waves [Malhotra and Carino, 2003, Jozi et al., 2014]. Numerous techniques for nondestructive evaluation of timber distribution poles have been developed from mechanical stress wave measurements, including the pulse

TABLE 3: Equivalent reduction in circumference of 30 to 40 inch circumference poles for external pocket decay [RUS, 2013, Bureau of Reclamation, 1992]

	Width of Decay Pocket (in)					
Depth of Decay Pocket (in)	1	2	3	4	5	6
1	1	1	2	2	3	5
2	1	2	3	4	5	7
3	1	2	4	5	6	8
4	2	3	4	5	7	9
5	2	3	4	6	8	10

TABLE 4: Safety factors of 30 to 40 inch circumference poles by reduced circumference [RUS, 2013, Bureau of Reclamation, 1992]

Original Measured Circumference (in)	**Reduced Circumference (in)**					
SF4	SF3.5	SF3	SF2.65	SF2.5	SF2	SF1.5
30.0	28.7	27.3	26.1	25.6	23.8	21.6
31.0	29.7	28.2	27.0	26.5	24.6	22.3
32.0	30.6	29.1	27.9	27.4	25.4	23.0
...	...	...	...	...	...	...
37.0	35.4	33.6	32.3	31.6	29.4	26.6
38.0	36.3	34.5	33.1	32.5	30.2	27.4
39.0	37.3	35.4	34.0	33.3	31.0	28.1

velocity method, sonic echo method, and bending wave method. These methods will be summarized in the following subsections.

2.2.2.1 Pulse Velocity Method

In the Pulse Velocity Method, the measurement is based on recording the arrival of the P-waves traveling across the cross section of a pole by placing a sensor diametrically across from the point of impact or transmitting transducer, as shown in Figure 2.3. By measuring the difference in time from the generation of the source wave to the arrival at the opposite side of the cross section and using a geometric measurement of the path length, the P-wave velocity, v_p, can be calculated.

When a stress wave reaches an interface with a lower mechanical impedance, it will reflect from this surface rather than continue to propagate in the original direction. As a result, if a hollow cavity is present in the cross section then any stress wave arriving at the other side of the cross section must travel around the cavity. Consequently, discontinuities in the wood will increase the apparent travel time of the stress wave and will decrease the calculated v_p [Popovics, 2003]. For isotropic materials, the P-wave velocity is related to the Poisson ratio, ν, elastic modulus, E, and mass density, ρ, by Equation 1. Although wood is anisotropic, this equation can still be used to approximate the relationship between the P-wave velocity and the material properties in the direction of the propagating stress wave. Furthermore, although the P-wave velocity is not directly related to the material strength, the strength and condition of a timber pole in both the axial and flexural direction is influenced by the elastic modulus. Reductions in pole strength due to material degradation in the section will be reflected in the bulk elastic modulus and so corresponding reductions in the P-wave velocity can be used to infer the likelihood that there may be a structural deficiency and susceptibility to structural failure. However, with the conventional Pulse Velocity Method, it is difficult to determine the size of decay and the location of decay [Hasenstab et al., 2006].

$$v_p = \sqrt{\frac{E(1-\nu)}{\rho(1+\nu)(1-2\nu)}} \tag{1}$$

An advantage of the Pulse Velocity Method is the ability to move the source and receiver pair locations around the diameter of the pole so as to assess multiple paths

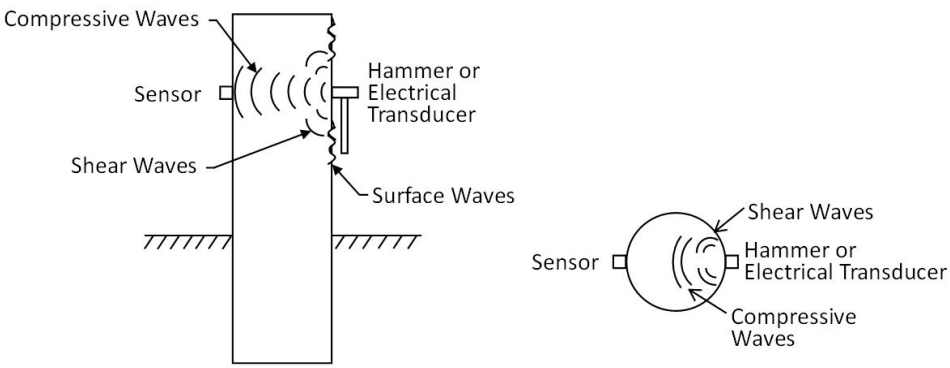

FIGURE 2.3: Schematic of the Pulse Velocity Method applied for condition assessment through the cross section of a pole

through the cross section of a single pole at several elevations. Building on this concept, tomography can be applied with multiple pulse velocity readings to generate an image of the tested cross section through inverse modeling (Figure 2.4), although this process can be challenging to apply and time consuming. Additionally, the Pulse Velocity Method can only be used to evaluate the exposed length of a pole, so it is an unsuitable method for assessing sub-grade portions of installed timber distribution poles without excavation.

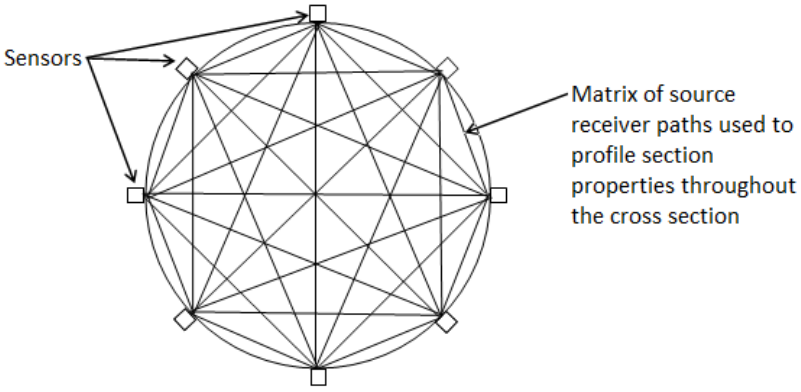

FIGURE 2.4: Analysis of source and receiver locations to measure stress wave propagation paths used to develop tomographic images

2.2.2.2 Sonic Echo Method

Another mechanical stress wave technique is the Sonic Echo Method, which uses measurement of reflections of stress waves to evaluate material properties for condition assessment. Similar to the Pulse Velocity Method, stress waves are introduced in the pole by an impact force and when traveling through the pole are reflected by differences in material and geometric properties [Krause et al., 2015]. The principle difference to the Pulse Velocity Method is that the time between subsequent reflections, or the frequency of the stress wave reflections, is used to estimate the P-wave velocity rather than the time of the first stress wave arrival. This approach is advantageous as it requires only measurement from the receiving transducer and permits the source and receiver to be positioned at the same surface, which allows for unique test configurations that can not be used with the Pulse Velocity Method. For example, the Sonic Echo Method can be applied to measure P-waves traveling longitudinally down the length of the pole and into the region below the ground line. In this configuration, the impact force is applied to the free end (or top) of the pole (Figure 2.5). Once introduced, the P-wave travels the length of the pole to the pole butt, where it is reflected back towards the top of the pole. The surrounding soil has lower mechanical impedance than the pole, therefore the P-wave does not significantly propagate into the soil. If decay or other discontinuities are present in the pole, a portion of the P-wave will be reflected before it reaches the pole butt. A sensor affixed near the impact location records the displacement, velocity, or acceleration of

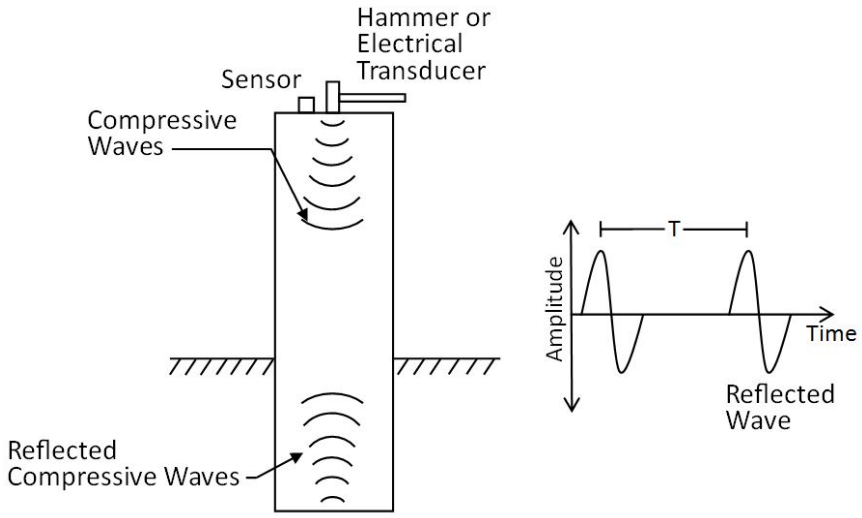

FIGURE 2.5: Longitudinal stress waves introduced at the top of the pole and reflected from the butt of the pole in the Sonic Echo Method

the returning P-wave for analysis [Jozi, 2015].

The Sonic Echo Method uses the frequency of the stress wave reflections, f, to determine an estimate of the P-wave velocity. This frequency corresponds to the inverse of the time, T, required for the stress wave to travel from the top of the pole to the butt and back again. The distance the stress wave travels in this period is then twice the length of the pole, L. With this dimension and time information, the P-wave velocity can be obtained from the frequency measurement by Equation 2. With a measurement of the P-wave velocity, the bulk elastic modulus of the pole can be estimated using Equation 3, which is a rearranged form of Equation 1. This estimation of the elastic modulus of the wood can be used for a coarse assessment of the structural condition of the pole. However, since the measurement is essentially an average over the entire length of the pole, this approach is not appropriate for identifying moderate levels of localized decay.

$$v_p = \frac{2L}{T} = 2Lf \tag{2}$$

$$E = v_p^2 \rho \frac{(1+\nu)(1-2\nu)}{(1-\nu)} \tag{3}$$

In addition to estimating the longitudinal elastic modulus, the Sonic Echo Method can be used to determine the presence of decay in a pole. Higher attenuation rates have been reported when decay is present [Krause et al., 2015], so a measure of the decay rate of subsequent reflections can also be used to characterize the health of the pole. Also, when significant decay is present in the cross section, the longitudinally propagating stress waves will be reflected at this decay, which results in a reduction in the reflection period, or an increase in the frequency of the stress wave reflections. The location of decay producing this premature reflection can be determined by generalizing the path length to d and rearranging Equation 2 as shown in Equation 4. In this equation, d is the distance from the top of the pole to the decay, T_d is the travel time associated with the P-wave traveling from the top of the pole to the decay and back, and f_d is the corresponding frequency of this stress wave reflection. When such decay is present along the length of the pole, this frequency as well as the frequency associated with stress waves traveling to the butt of the pole and back will often both be present in the measurement spectrum.

$$d = \frac{v_p T_d}{2} = \frac{\nu_p}{2f_d} \tag{4}$$

While it is possible to determine the location of decay in a pole, another significant

shortcoming is the difficulty of determining the size or severity of any decay identified. The amplitude of the reflected wave is not sensitive to the longitudinal size of the defect. In addition, the further from the impact a defect is, the larger it must be in order to be detected through the Sonic Echo Method [Huang et al., 2010]. The principal disadvantage of the Sonic Echo Method is that the top of the pole must be accessible in order to utilize this method in the traditional manner.

2.2.2.3 Bending Wave Method

In addition to pulse velocity and sonic echo techniques, the Bending Wave Method has received significant attention as a potential mechanical stress wave method for nondestructive evaluation of timber distribution poles. Unlike the previous two methods, it utilizes bending waves to determine the condition of the pole instead of P-waves. In order to induce bending waves, the pole is impacted on its side, as shown in Figure 2.6, and multiple sensors are placed along the length of the pole to record the propagation and reflection of the bending waves as they travel down the length of the pole [Krause et al., 2015, Jozi, 2015]. This ability to generate the impact force near the ground line while analyzing waves that are propagating to the region below the ground line is a practical advantage of the Bending Wave Method that is responsible for its popularity. As with the previous stress wave methods, any pockets of decay will create premature stress wave reflections, while in a healthy pole the bending waves will reflect at the butt of the pole. When a pole is impacted, numerous bending waves of dissimilar frequencies are created and interfere with each other. Due to this interference, the velocities of bending waves are not constant, but are a function

of frequency and wavelength, which complicates the analysis process [Krause et al., 2015]. A mathematical technique known as the Short Kernel Method has been proposed as a tool for identifying individual wave frequencies and their velocities, their echoes, and the point from where they are reflected [Jozi, 2015].

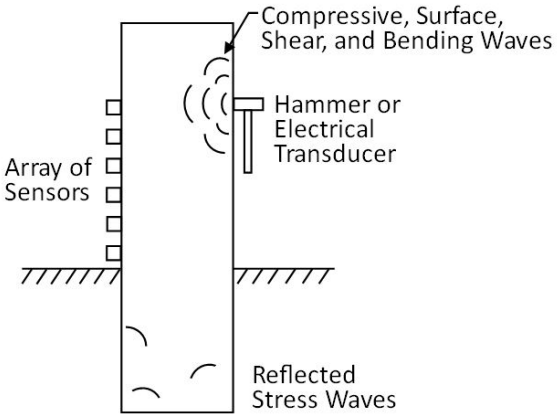

FIGURE 2.6: Stress waves introduced into a pole and measured by a linear array of sensors in the Bending Wave Method

A study conducted by North Carolina State University utilized the Short Kernel Method to determine the condition of timber piles by analyzing bending waves traveling at the frequency of peak magnitude in the measurement signals. The waves occurring at this kernel frequency are isolated from the recorded data and are analyzed to determine wave speed and the corresponding elastic modulus. Significant differences were identified in bending wave speed estimates made between those calculated using the Short Kernel Method and those obtained experimentally. However, the equation used in the study to calculate the bending wave speed does not take into account the dispersion of the measured bending waves and, therefore, it cannot accurately calculate bending wave speed. Subsequently, the study determined that values obtained using the Short Kernel Method were inaccurate [Kim et al., 2000].

While the Short Kernel Method analyzes the signal corresponding to one main frequency, Wavelet methods can be used to individually analyze each recorded signal regardless of the frequency content [Subhani et al., 2011]. Wavelet methods are best utilized in conjunction with an array of multiple sensors distributed over an area of interest and therefore must rely on reflected bending waves to assess subgrade portions of timber utility poles, which introduces challenges in processing and data collection as such wave reflections can be caused by reasons other than decay. One study using isotropic analytical pole models and experimental pole assessments found that Wavelet methods are capable of accurately detecting decay and decay severity using the reflections of bending waves [Yan, 2015]. However, the results and conclusions have yet to be validated through systematic experimental testing.

2.2.3 Experimental Modal Analysis and Structural Identification

Experimental Modal Analysis is a nondestructive evaluation technique that relies on principles of structural vibration to measure dynamic properties of a structure, including natural frequencies, damping ratios, and mode shapes. Such modes for timber distribution poles occur naturally under dynamic excitation of the pole, which can be achieved by the application of an impact force or a controlled actuator, such as an electrodynamic shaker. The free vibration response of the pole is typically measured by accelerometers or geophones. Experimental Modal Analysis is similar to Stress Wave Propagation methods in that both techniques rely on the relationship between vibration waves and the structure to which they are applied. However, stress waves occur at a much higher frequency than structural vibrations, which typically

occur at frequencies less than 100 Hertz.

Once the free dynamic response of a pole is measured, a Fourier transformation is conducted in order to determine the dynamic properties of the pole [Damgaard et al., 2013], which can be compared to experimental measurements or analytical estimates of the dynamic properties of a healthy pole. The presence of pole damage is suggested when the measured natural frequencies are less than those of the reference values for the healthy pole, as the decrease in natural frequencies corresponds to increased deflections in the mode shapes of a pole and decreased pole stiffness [Baraneedaran et al., 2009]. Through the iterative process of structural identification, parameters of analytical prediction models can be adjusted until correlation between experimentally measured parameters and the model is maximized. Analysis of the corrected parameters in the model can be used to estimate the location and extent of damage or decay.

One study investigating the potential use of experimental modal analysis for pole testing utilized free vibration testing of suspended poles without considering the embedment condition at the ground support. This study was conducted on full-size red pine distribution poles suspended in the air to estimate the first natural frequency and, subsequently, the dynamic modulus of the pole. A generally strong correlation was found between this dynamic modulus estimate and the elastic modulus determined from static bending tests, although ring shake present on one of the poles was not identified during testing because only the first natural frequency of the pole was used to estimate the dynamic modulus [Barclay et al., 1999].

Multiple patents have been awarded since the 1980s that utilize vibration testing

and experimental modal analysis as a basis for determining the condition of timber utility poles. The first patent, awarded to Unisearch Limited in 1983, details a testing process similar to that previously described. The condition analysis method described in the patent involves using three measured natural frequencies of the pole. These measurements are compared to one another and if a harmonic relationship is observed, the pole is considered healthy [Dunlop, 1983]. Harmonic relationships are also described in a later patent as a way to detect the condition of a timber structural member, although the relationships analyzed are between those of the surface vibrations and shear vibrations of the pole. This patent uses electrodynamic shakers to excite a pole and then analyzes the recorded data through discrete Fourier transformations before comparing the frequency or amplitude of the vibrations [Hosgood et al., 1989].

Several patents also detail the use of computer programs to expedite the modal analysis process, often by using Fourier transformations of digitally recorded measurements to determine natural frequencies. One of these patents describes condition assessment of the pole using a very simplified approach to structural identification where at least two natural frequency measurements are used to iteratively quantify the value of a rotational spring at the base of a linearly tapered analytical beam model and the geometry of the pole [Franklin et al., 1990]. In this process, Equation 5 is used to mathematically calculate the natural frequencies ($f(i)$) of the analytical model of the pole (Figure 2.7) which are used in conjunction with structural identification to optimize the predictions of the analytical model to match the measurements obtained from the tested pole. Parameters in the model include pole length (L), moment of

inertia (I) and cross sectional area (A) at the ground line, elastic modulus (E), density (ρ) and a relationship (β'(i)) between the eigenvalue specific to the boundary conditions for each mode (β(i)) and the taper of the pole (ξ), defined by Equation 6. In the approach described in the patent, the dimensional and material properties of the pole are assumed and the parameters for the taper and β values specific to the spring constant for the rotational spring at the base of the pole are iteratively adjusted until the prediction model optimally agrees with the natural frequency measurements. The estimated spring constant is proposed as a means of assessing the condition of the pole below the ground line. However, this approach adopts a number of assumptions in the model, such as perfectly rigid soil support, assumes all decay can be represented by the rotation base spring, and neglects the presence of supported electrical infrastructure on the pole.

$$f(i) = \frac{[\beta'(i)]^2}{2\pi L^2}\sqrt{\frac{EI}{\rho A}} \tag{5}$$

$$\beta'(i) = \beta(i)(1-\xi) = \beta(i)(1-\frac{d_{min}}{d_{max}}) \tag{6}$$

‘

X-POLES by Cinetix SRL is one commercial device that implements timber pole condition assessment using experimental modal analysis. The physical characteristics of the pole, including the height, diameter, and additional supports, are required as inputs to the device prior to testing. Through analysis of a digital photograph, the device has built-in capability to be able to automatically estimate the height

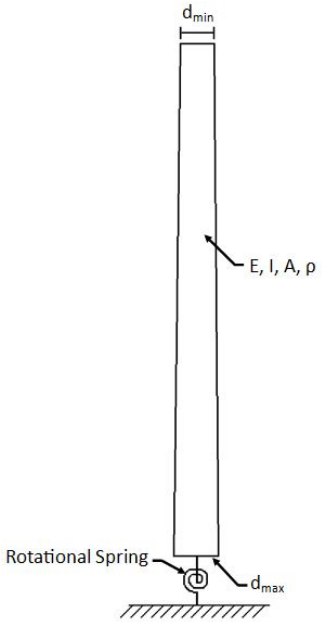

FIGURE 2.7: Schematic of linearly tapered pole model with simplified boundary condition utilized to assess timber distribution pole conditions in Powertech Labs Inc. Patent

of the pole and the diameter of the pole at the height of both the device and the applied impulse excitation. Structural vibrations of the pole due to an applied impulse excitation are detected by the device, which analyses the recorded response of the pole to estimate the first three natural frequencies. The physical characteristics of the pole are then used to numerically predict what these first three natural frequencies would be for a healthy pole of the same geometry. An output signal is provided to indicate whether or not the pole meets established safety parameters that are developed as intervals around the predicted natural frequencies. The measured modal parameters and recorded pole characteristics may also be stored for future reference or further processing [Piazza et al., 2014].

2.2.4 Infrared Thermography

Infrared thermography measures the amount of radiation emitted from objects and

then converts these readings into temperatures that are typically portrayed as a processed image with a color intensity map. After the image is obtained, the surface temperature distribution is analyzed to determine if there are any internal material discontinuities, which are typically indicated by lower temperatures due to reduced efficiency of thermal conductivity in the degradated material [Burcham et al., 2011]. Infrared thermography has been used in a number of nondestructive evaluating applications, including inspection of electrical components, aerospace composites, tank and silo monitoring, and building envelope surveys [Hellier, 2001]. Both active and passive thermography methods have been used for quality assurance and quality control in the production of wood panel materials by providing a means to nondestructively detect defects. Active thermography uses radiators to heat the material to be tested, while passive thermography tests a material that already has a sufficient temperature gradient due to ambient or existing process heat sources. In both cases, areas surrounding defects will cool slower and hotspots can be readily identified in the thermographic pictures. A study of the effectiveness of thermographic inspection for this wood panel production process revealed that both the active and passive methods were capable of revealing defects in the wood. However, while this application is relevant and promising to the scope of the current study, the panels tested did not have the same thickness typical of timber utility poles [Meinlschmidt, 2005].

Another thermographic technique is known as pulsed thermography and has been described as one of the most effective techniques to detect decay in wood [López et al., 2014]. In this technique, wood is subjected to a heat source and the speed at which the heat travels through the wood is examined through its resulting effects on the

surface temperature of the wood. The presence of internal defects typically alters one or more of the thermo-physical properties of the wood (e.g. density, specific heat, thermal conductivity, etc.) and consequently, the rate of heat transfer is different than that exhibited in sound wood. This relative difference in heat transfer is reflected on the surface of the material as a thermal contrast. It is noted that thermal contrasts resulting from discontinuities at a greater depth from the surface of the wood will take longer to appear and therefore it is important in the pulsed thermography method to record the time between heat application and appearance of thermal contrast. Experimentally, the paper presents results from 2 cm thick oak and beech dimensional lumber samples that were exposed to varying time periods of heat, during which infrared images were captured every 60 seconds. After the heat was applied, images were captured every 15 seconds during the cooling process and images were post-processed to create three-dimensional thermal maps of wood samples at the time of image capture. With the analysis of these thermal maps in comparison to the location of the mechanical voids in the wood, it was concluded that infrared thermography easily detects surface and near-surface defects, although larger defects further from the surface were also recognized with relative ease. In this study, defects considered to be near-surface are those located at a depth of 2 millimeters or less from the surface of the wood, whereas deep defects were classified as being located as deep as 8 millimeters from the surface of the wood [López et al., 2014].

A more recent study evaluated the effect of wood density on surface temperature as well as the effectiveness of using infrared thermography to detect wet internal defects, dry internal defects, and the voids that are a result of insects such as termites. Wet

defects can be defined as those with a higher moisture content than the sound wood and dry defects are those with the same moisture content as the sound wood. The wood samples in the experiment were manufactured from dimensional pine lumber and were heated in an oven at 80 degrees Celsius for 30 to 45 minutes. Once heated, the samples were removed from the oven and infrared images were captured every 30 seconds during the cooling process. The study concluded that dry internal defects larger than 4 square centimeters can be detected up to depths of 1 centimeter while 1 square centimeter wet defects and larger can be detected up to depths of 1.5 centimeters. However, the study found that small dry defects such as those created by termites cannot be differentiated from sound wood using the thermographic measurements obtained [Conde et al., 2012].

A pair of papers exploring the possibility of utilizing infrared thermography to detect discontinuities in wood utility poles was published in 2001. The first paper utilizes an analytical model to estimate the effectiveness of thermographic wood analysis. Inputs in the model include a generated temperature gradient and thermal wood properties including density, thermal conductivity, specific heat, thermal diffusivity, and convection coefficient. Another input, moisture content, is described as 15% for sound wood and 30% for decayed wood. With the defined model geometry and thermal properties adopted by the study, different heating methods were applied to the model to predict the potential for identifying internal defects in wood by measurement of thermal radiation emitted at the exterior surface of the wood. One heat application method studied involved simulating the application of heat in through-holes present in timber distribution poles that are usually used by workers to fix hooks prior to

climbing the pole for maintenance. Additional simulated heat application methods included heat applied from the exterior of the pole or through microwave heating. This analytical study ultimately concluded that infrared thermographic analysis was only suitable as a nondestructive inspection method for defects near the surface of the wood, though further study is suggested [Wyckhuysea and Maldaguea, 2001a].

The second paper also utilized an analytical model, although the model was revised to reduce the number of variables and to simplify the model by adopting different model geometry. Moisture contents of 21%, 30%, and 40% were studied, along with the previously mentioned surface heating method and the microwave heating method. The results of the model suggests that the applied heat can only be transmitted through wood for a limited distance unless the heat is applied for a long time. For instance, it was estimated that in order to develop a 1 degree Celsius temperature change at a distance of 6 cm from the heat source, the heat must be applied for more than 2000 seconds. To confirm the simulation results, experiments reflecting the conditions simulated in the models were conducted. The experiments largely confirmed the results of the models by showing that dry defects are largely undetected by infrared thermography and that discontinuities at deeper depths in the wood require a long exposure to a heat source [Wyckhuysea and Maldaguea, 2001b].

2.2.5 Other NDE Methods

Additional techniques for determining the condition of timber utility poles include microdrilling, bore sampling, and radar methods. These techniques may prove to be helpful when determining the presence of discontinuities in utility poles, however, they

are not always considered effective and may not be appropriate for rapid nondestructive assessment. Microdrilling and bore sampling penetrate into the cross section of the pole, which can open a pathway for decay into the core even if the pole has been treated with preservatives. Microdrills, as the name suggests, are drills consisting of diametrically small bits, some of which are smaller than 0.06 inches. The drill pushes the bit into wood at a constant speed and the resistance that the drill experiences is recorded along the path of the drill bit [Brashaw et al., 2006]. Decay can be detected through microdrilling, as decayed wood provides less resistance than healthy wood. Bore sampling is an inspection method that utilizes a hollow increment borer to drill into the pole and remove a sample from the interior of the cross section to allow for visual examination of the condition of the tested pole. Bore sampling is relatively inexpensive and can be used to test a portion of the pole below grade, but it can introduce decay into the core of a pole. The x-ray method can detect early stages of decay, though it is expensive and time consuming. Additionally, workers must excavate around the base of the pole in order to detect subgrade decay [Pines, 1997] and radar based testing often includes high costs and significant post-processing of collected data.

Acoustic resonance techniques have also been research as a tool for nondestructive evaluation of timber poles. As an improvement on the conventional "sound and bore" inspection routine currently used, the vibroacoustic method relies on a microphone, rather than an inspector's ear, to capture the sound of a pole being struck. One study developed signal processing algorithms for condition assessment of timber pole sections by recording the impact sounds of a large number of in-service poles that

were also characterized by conventional inspection methods to determine the actual condition. When utilized, the algorithms rated pole strikes on a scale of 0 to 10 to quantify the relative extent of decay. Upon testing, two of the developed algorithms estimated the condition of poles with an accuracy of 97.7%, although the analysis discounted a series of poles that were tested in wet conditions. This suggests that the technique may be challenging to apply over a range of operational and environmental conditions encountered in the field. The study suggested that testing a pole three times and analyzing the resulting sound with the algorithms could improve testing accuracy to greater than 99% [Craighead et al., 2001]. The authors of this study developed a prototype portable hand-held meter for British Telecom to perform the pole assessment using their acoustic resonance technique, however, it is unknown whether this device has been used in routine practice.

CHAPTER 3: DEVELOPMENT OF AN EXPERIMENTAL TESTBED FOR EVALUATION OF NDE TECHNOLOGIES FOR DISTRIBUTION POLES

For this study, a full-scale experimental test bed was developed to evaluate candidate techniques for rapid nondestructive assessment of timber distribution poles with decay below the ground line. Specifically, nondestructive approaches were explored in order to identify pole condition assessment techniques viable for use by linemen to supplement the conventional sound and bore inspection methods. Viable assessment techniques were to be investigated for their potential to address the condition assessment challenge as well as for their potential to be developed into a low-cost, portable, and rugged instrument for routine field use. Specifically, such a device would need to be: 1) Easily operable for those with limited training and engineering background, 2) Operational without requiring soil excavation, 3) Capable of being conducted with minimal setup and operation time, and 4) complementary to the existing conventional inspection techniques. This chapter documents the preparation of the experimental test bed, the instrumentation and methodology used to collect nondestructive test data for each of the four techniques, and destructive characterization of the pole specimens to quantify the actual extent of deterioration in each pole.

3.1 Description of Experimental Testbed

A concrete-lined geotechnical testing pit in the UNC Charlotte EPIC Structural HighBay Lab was used for the development of the experimental test bed. This cylin-

drical pit is 10 foot in diameter, 10 foot deep, and features a submersible pump installed in a square basin at its base to allow for extraction of pore water from the soil in the pit. A locally sourced, poorly graded red mortar sand with a mean grain size around 0.016-inches was selected to serve as a representative soil medium in the test bed. Preparation of the pit was conducted by first lining the bottom of the pit with a geotechnical membrane, which was extended approximately two feet up the wall of the pit (Figure 3.1a). On this first membrane layer, a metal grate was placed over the sump pump basin to protect the sump pump from the pressure of the sand and the installed poles. A second layer of geotechnical membrane was placed over the sump pump grate prior to the installation of the sand. In order to achieve generally uniform compaction and density of the sand throughout the depth of the pit, the sand was installed in lifts (Figure 3.1b), each of which was manually leveled and lightly compacted before the soil was saturated with water (Figure 3.1c). After saturation, the sump pump was used to remove the water from the pit prior to installing the next lift of sand. The saturation of the pit encouraged uniformity of the soil density and the suction pressure developed during extraction of the water encouraged compaction of the soil. The first lift was approximately a 6 inch depth of loose fill and the subsequent six lifts used to fill the remainder of the pit varied from 1 to 2 feet in depth (Figure 3.1d).

Water was again introduced and pumped from the pit prior to installing the timber utility poles. The resulting moisture content of the sand ensured its stability during the augering process for the pole installation. Each hole was augered using a skid steer with a 4 foot long, 16 inch diameter auger bit and a bit extension to reach the desired

FIGURE 3.1: Preparation of geotechnical testing pit at EPIC Structural High Bay Laboratory: a) installation of geosynthetic filter to protect submersible pump b) adding a lift of red mortar sand to the pit, c) flooding pit with water to saturate and compact soil through drainage cycles, d) fully filled soil pit

installation depths (Figure 3.2a). The poles were placed in the augered holes using a crane to lift the pole tops (Figure 3.2b)and, when additional support was required to prevent fracture of severely decayed poles, a telescopic hauler was used to lift the butt of the pole to prevent excessive stress in the pole during installation. Each pole in the experimental test program was installed with an embedment depth corresponding to the original depth of embedment in the field. This original embedment would be identified by visible residual soil and discoloration as well as the presence of plugs from microdrill inspections performed at the ground line (Figure 3.2c). Once the poles were in place (Figure 3.2d), the extracted sand was replaced in the holes and

FIGURE 3.2: Installation of timber distribution poles in experimental test bed: a) augering holes with skid steer, b) lifting poles with overhead crane c) measuring pole dimensions and marking pole, d) installing pole to original depth of embedment

was compacted through the use of water and hand compactors. To prevent collapse of the holes, each pole was installed individually prior to augering the next hole. During the pole installation, two soil moisture sensors were placed in the walls of two holes at a depth of 18 inches, as shown in Figure 3.3. The soil moisture sensor placed adjacent to Pole 5 was a Decagon Model STE Digital Sensor capable of measuring soil temperature, electrical conductivity, and volumetric water content, while the soil moisture sensor placed adjacent to Pole 7 was a Decagon Model 10HS Analog Sensor capable of measuring volumetric water content.

A total of ten timber distribution poles of various age and extent of deterioration

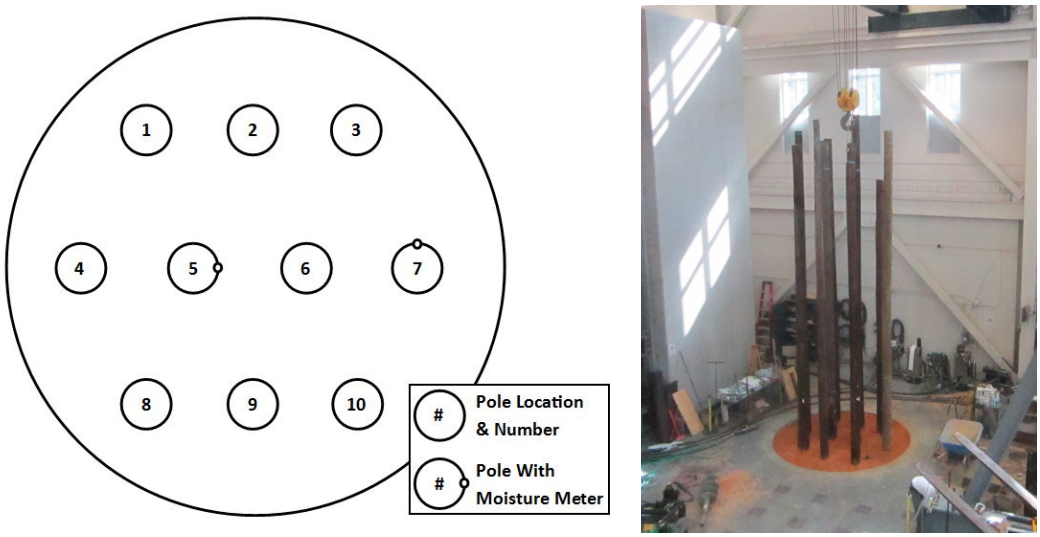

FIGURE 3.3: Location of ten timber distribution poles and moisture meters installed in experimental test bed

below the ground line were installed in the experimental test bed (Figure 3.3). Of the poles tested, one pole (Pole 7) was a new pole treated with CCA preservative, while the remaining poles were originally treated with Creosote preservative and were removed from years of service in the field. The timber species of all poles was likely southern yellow pine. Prior to installation, the pole lengths and the circumferences at the top and base of the pole were measured and the installed depth of embedment was recorded after installation. These geometric characteristics of the timber poles are presented in Table 5. The condition of each pole in the region below the ground line was also photographed (Figure 3.4). Individual data sheets for each pole containing the geometric properties, pole markings, inspection tags, and estimates of timber properties are provided in Appendix A.

3.2 Summary of Instrumentation and Procedures used for Collection of Nondestructive Test Measurements

Four techniques were selected for further study based on the complexity and cost

TABLE 5: Geometric characteristics of timber distribution poles included in th experimental test program

Pole Number	Length	Base Circumference	Top Circumference	Embedment Depth
1	30'-0"	38 1/4"	25"	5'-9"
2	29'-11"	36"	25 3/4"	4'-4"
3	26'-9 1/4"	35 1/4"	24 1/4"	5'-10"
4	30'-0"	33 7/8"	21 7/8"	5'-5"
5	29'-10 1/2"	30 3/4"	24 1/4"	5'-10"
6	28'-5 1/2"	36 3/4"	23 1/2"	6'-4"
7	30'-1"	29"	23 1/4"	5'-10"
8	30'-0"	36"	27 1/2"	6'-6"
9	29'-9 1/2"	27 1/4"	17 3/4"	5'-0"
10	29'-8"	29 3/4"	21 3/4"	6'-4"

1 2 3 4 5 6 7 8 9 10

FIGURE 3.4: Photographs of the condition below the ground line for the timber distribution poles included in the experimental test program

of required sensing technologies and the ability to automate the analysis of measurements in a simplified microcontroller. These techniques included guided stress wave propagation, experimental modal analysis, acoustic resonance testing, and infrared thermography. Each of the nondestructive tests were performed under both unsatu-

rated and saturated soil conditions. First, tests were conducted on the poles after the sump pump was used to remove water that was introduced into the test bed during pole installation and the test bed was allowed to dry. After tests were completed, water was reintroduced to the test bed until the soil was saturated, at which time the soil moisture sensors were used to collect temperature, moisture, and conductivity data of the soil. The average soil temperature and volumetric water content during the unsaturated tests were 72.1°F and 8.4%, while for the saturated test the soil temperature was measured as 62.6°F and the average measured volumetric water content was 28.6%. The suite of nondestructive test experiments were conducted again on the timber poles in saturated conditions to provide an opportunity to investigate the sensitivity of each method to changes in the soil condition.

3.2.1 Guided Stress Wave Propagation

The guided stress wave testing included an array of six PCB Model 353B31 accelerometers, which are ± 100g full scale range single axis accelerometers. The first accelerometer was installed 1 inch above the pole's ground line with the remaining five sensors longitudinally spaced 6 inches apart up the pole (Figure 3.5b). Additional components of the mechanical stress wave propagation assembly include 0.5-inch and 1-inch long 10-32 threaded rods, 1.5-inch long 1/4-20 threaded rods, and 0.25-inch thick 90 degree angles with 1-inch legs that were cut into 1-inch sections. The 1-inch 10-32 threaded rods were used to attach the PCB Accelerometers to the poles at the locations indicated in Figure 3.6. First, holes approximately 0.5-inches deep, and slightly smaller in diameter than the 10-32 threaded rods, were drilled at the loca-

tions responding to the sensor locations. Next, the threaded rods were screwed into the holes. To permit biaxial measurement, the accelerometers were either threaded directly onto these rods to measure stress waves in the transverse direction or were fastened to the angles to record motion in the longitudinal direction. A hole on one leg of the angle was threaded to allow for the 0.5-inch 10-32 threaded rods to secure the accelerometers directly to the angles. A through-hole on the other leg of the angle was drilled to allow for the angles to be fastened with a nut to the threaded rod installed in the pole.

a) 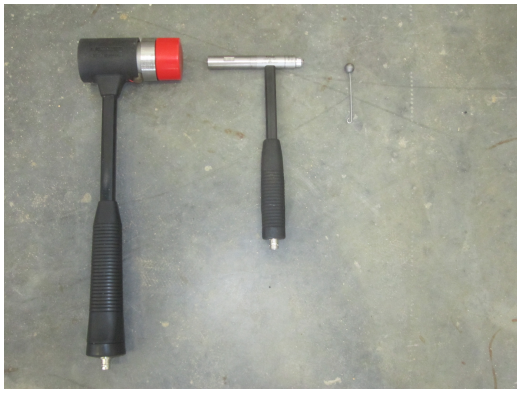 b) 

FIGURE 3.5: Guided stress wave testing: a) impactors used to strike poles during guided stress wave testing; b) photograph of guided wave test setup

In addition to the brackets used to mount the accelerometers to the pole, strike brackets were installed to permit application of impacts with similar force characteristics in either the transverse or longitudinal directions. Strike brackets were made by utilizing the same L1x1x1/4 angle sections that were used to fasten the sensors to the pole. Unlike the sensing brackets, the strike brackets have only one through hole

drilled on one leg to allow for the bracket to be fastened to the pole by threaded rod and nut.

Strikes were applied in both the transverse and longitudinal directions as shown in Figure 3.6. Since the accelerometers only measure the structural response of the pole in one direction, stress waves were generated with the array of accelerometers oriented in two different directions. Motion perpendicular to the surface of the pole was measured when the accelerometers were oriented in the horizontal direction (Figure 3.6a) and motion parallel to the longitudinal axis of the pole was measured when the accelerometers were oriented in the vertical direction (Figure 3.6b). Impacts in both the horizontal direction and the vertical direction were generated at locations in-line with the row of accelerometers and at an azimuth angle of 90° in the cross section (Figure 3.6c).

The impactors utilized during testing (Figure 3.5a) include a PCB Piezotronics 086D20 short sledge impulse hammer with a medium hardness (red) plastic tip, a PCB Piezotronics 086C03 impulse hammer with a hard stainless steel tip, and a 12 mm diameter steel ball impactor. Each impactor excites frequencies over a different bandwidth with the short-sledge hammer concentrating energy below 300 Hz, the small impulse hammer distributing energy up to 2 kHz, and the steel ball impactor distributing energy up to 20 kHz. Corresponding estimated contact durations for each impactor are: 3333 μS for the short-sledge hammer, 500 μS for the small impulse hammer, and 50 μS for the steel ball impactor. A photograph of the guided wave testing setup is presented in Figure 3.5b.

In summary, testing was performed with accelerometers in both the horizontal

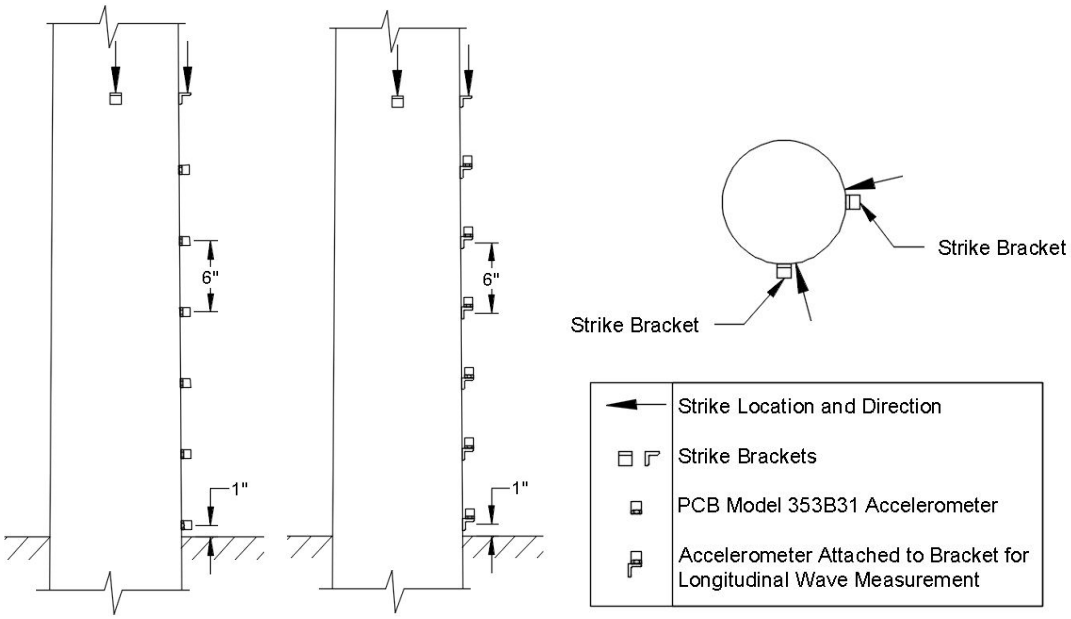

a b c

FIGURE 3.6: Stress wave testing sensor and impact locations and orientations: a) horizontal accelerometer layout; b) vertical accelerometer layout: c) cross sectional locations for both accelerometer layouts

and vertical directions by three impactors striking both horizontally and vertically, resulting in 24 unique combinations of sensor orientation, hammer type, hammer orientation, and impact location for each of the tested poles. A total of five impacts over a duration of 0.1 seconds per impact were recorded for each of the testing configurations by each impactor. Signal conditioning and data acquisition of the transducer output from the accelerometers and the impulse hammers was performed by a 24-bit National Instruments PXIe-4497 dynamic signal analyzer. A sampling rate of 204.8 kHz per channel was used and sampling was initiated with an analog reference trigger with a pre-trigger delay of 1000 samples.

3.2.2 Experimental Modal Analysis

The second nondestructive test performed was vibration testing to extract estimates of the natural frequencies of the poles by experimental modal analysis. Figure 3.7 shows the sensor locations for the modal testing and the location of the applied impulse excitation, which were both located 6 feet above the ground line. In this test setup, two PCB Piezotronics 333B52 single-axis accelerometers were located orthogonal from each other around the surface of the pole and were affixed using tacky wax. These accelerometers feature a $\pm$ 5g full-scale range, 1000 mV/g sensitivity, and 0.5 to 3000 Hz measurement bandwidth. A PCB Piezotronics 086D20 short-sledge impact hammer with a soft plastic (brown) tip was used to strike each pole fifteen times at a location that was equidistant from both accelerometers at 135 degrees from each sensor. The accelerometer and impact hammer signals were signal conditioned and sampled using a National Instruments PXIe-4497 dynamic signal analyzer that was set to sample over a 5 second duration at a rate of 1 kHz for each impact. Due to the single impact location on the pole, only one axis of the pole is being excited, as indicated by the dashed line in Figure 3.7. The use of two accelerometers attached to the pole on either side of this axis to measure the vibrational response serves to null unintentional excitation of out-of-plane modes by averaging. Additional information of the vibration test setup is presented in Chapter 4, where complete modal analysis of a pole is presented to determine the sensor and impact locations.

Examples of the excitation force measured from the impact hammer in both time and frequency domain are presented in the left-hand side of Figure 3.8. When the

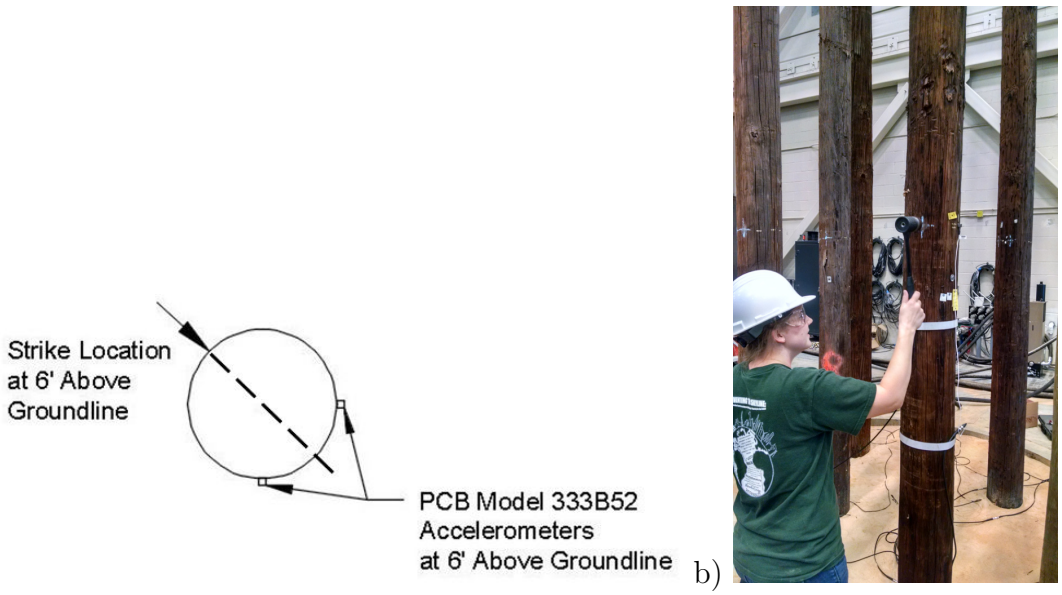

FIGURE 3.7: Experimental modal analysis: a) orientation of accelerometers and location of impact for experimental modal analysis of poles; b) photograph of experimental modal analysis setup

excitation force is plotted in the time domain, the duration of the impact can be identified. The transformation of this information to the frequency domain reveals the frequency bandwidth that is excited by the impact. The impulse duration and frequency bandwidth are inter-related and can be altered by changing the hardness of the hammer tip. This, in turn, changes the number of modes of the poles that were excited and the energy from the impulse that excites each mode. After evaluation of multiple impulse hammer tips, this study utilized a short-sledge impact hammer with a soft tip to create excitation over a bandwidth from 0 Hz to approximately 300 Hz, as indicated in Figure 3.8. A harder tip was used to try and excite higher-frequency modes of the poles to increase the number of natural frequencies measured for each pole, but the use of the harder tip was found to produce high peak accelerations that saturated the response of the accelerometers. These excitation forces were measured

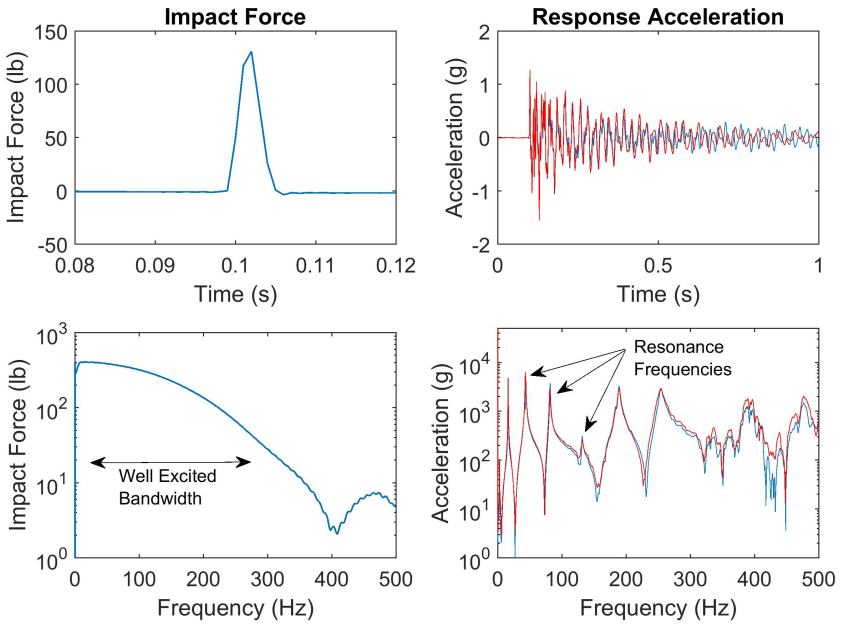

FIGURE 3.8: Overview of vibration measurement in both time and frequency domains

for each test and used to calculate the frequency response functions (FRFs), although measurement of the impact excitation is not required to estimate the natural frequencies because it provides an indication of the frequency bandwidth excited but does not reflect the dynamics of the pole.

The right-hand side of Figure 3.8 presents plots of the typical response of a pole measured by a pair of accelerometers in both time and frequency domains. In time domain, the response of the pole appears as a typical damped free vibration response but is not readily interpreted because it consists of multiple modes occurring simultaneously at different frequencies. Once converted to frequency domain, the natural frequencies for the bending modes of the pole can be identified as the peaks in the spectrum. In correspondence to the measured impact force plotted in frequency domain, the response spectrum is smooth over the bandwidth from 0 Hz to approximatley

300 Hz and is noisy at higher frequencies. This indicates that modes higher than 300 Hz are not well excited, making them difficult to identify. In this experimental test program, this frequency bandwidth from 0 Hz to approximately 300 Hz generally resulted in the measurement of the first eight modes of the tested poles.

3.2.3 Acoustic Resonance

The third nondestructive test performed on the set of poles in the experimental testing was acoustic resonance testing, which involves noncontact measurement of the sound waves generated by vibration of the pole from an impact excitation. In this test setup, a clamp was used to hold a PCB Piezotronics model 130E20 prepolarized array microphone near the ground line of the pole. This microphone is a 1/4 inch diameter free-field transducer with 20 Hz to 10 kHz frequency response and 122 dB dynamic range. The butt of the clamp was inserted into the ground at a location approximately 3-inches from the surface of the pole and was positioned so that the diaphragm of the microphone was approximately 1-inch from the pole. A series of hammers (Figure 3.9a) was used to conduct the acoustic testing of each pole. One hammer was a one-piece steel heavyweight hammer with a head weight of 3 pounds that conforms to the OSHA specifications for the conventional sounding test [OSHA, 2014]. Additionally, a standard claw hammer with an estimated head weight of 1 pound and a PCB 086C03 impulse hammer with mass extender providing a total head weight of 0.5 pounds were used to induce vibrations in the pole for acoustic resonance testing.

For each hammer, sound waves were measured first for four strikes applied to the

a)  b) 

FIGURE 3.9: Acoustic resonance testing: a) photograph of impactors used to apply strikes to the poles; b) photograph of acoustic resonance testing setup

pole near the diaphragm of the microphone (Figure 3.9b), then measurements were obtained for a second series of strikes applied radially around the circumference of the each pole, with one strike applied to each quadrant, as shown in Figure 3.10. A 24-bit National Instruments PXIe-4497 dynamic signal analyzer sampled the analog transducer signal and converted it to a digital signal at a rate of 50 kHz. A 2 mS pretrigger window analog reference was used in conjunction with 200 mS sampling durations for each impact to ensure consistent signal timing across each of the collected data sets.

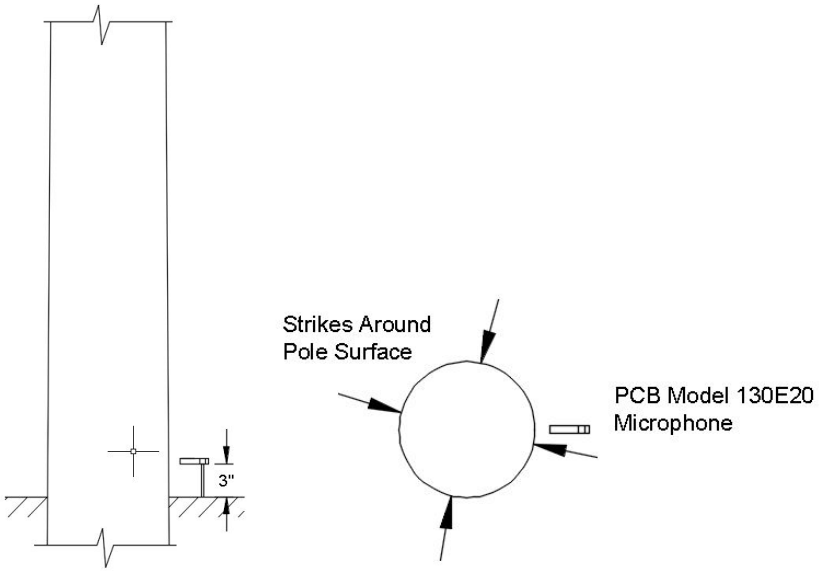

FIGURE 3.10: Locations of strikes and microphone during acoustic resonance testing

3.2.4 Infrared Thermography

The fourth and final nondestructive technique applied in the experimental program was infrared thermography, which was perfomred with the low-cost, portable FLIR C2 thermal imaging camera. The FLIR C2 has Multi Spectral Dynamic Imaging (MSX) image enhancement, which overlays the optical imaging with the thermal imaging for improved image definition, and is about the size of a small smartphone. Consisting of an infrared sensor with an 80x60 pixel array sensitive to 7.5 μm to 14 μm infrared radiation wavelengths, the FLIR C2 provides a thermal sensitivity of less than 18°F, a ±3.6°F accuracy, and a measurement range of 14°F to 302°F. Additionally, the camera provides a 640x480 pixel array fixed focal length digital camera that can acquire regular photographic images simultaneously with the thermal imaging sensor's thermal images.

Nondestructive infrared thermographic condition assessment of timber distribution poles requires a significant amount of heat in order to allow for the identification of a thermal anomalies associated with the presence of decay. Active thermography in the form of a 5-gallon BriskHeat metal drum heater (Figure 3.11) was used to introduce enough heat into the poles to provide the required thermal gradient for decay identification. The heater runs on 120V AC power and features an integrated thermostat that allows for the heater temperature to be controlled between 50°F and 425°F. This drum heater was secured to the surface of select poles (Poles 1, 7, 8, and 10) at the ground line, as shown in Figure 3.11a. Next, heat up to 350°F was applied for 10 minutes and thermographic images were captured after the drum heater was

removed (Figure 3.11b). The first image was captured directly after removing the heater from the pole, after which a sequence of thermal images were taken in 30 second intervals. When the pole had cooled for 4 minutes, images were taken in 1 minute intervals until the pole had cooled for 10 minutes. Pole 6 was tested similarly, although it was exposed to 20 minutes of heat at 350°F before the drum heater was removed.

a)  b) 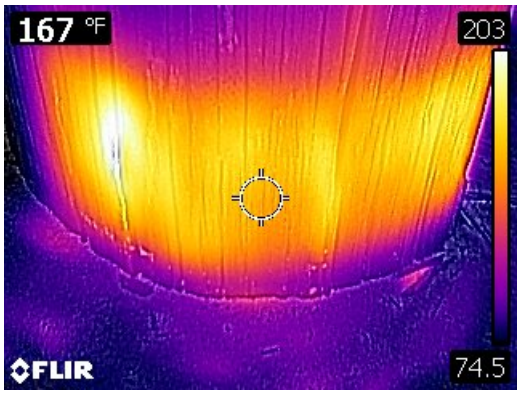

FIGURE 3.11: Infrared Thermograpy: a) photograph of location of silicone rubber band drum heater during thermal testing; b) typical thermal image acquired during testing

3.3 Destructive Characterization of Pole Condition

After all tests were conducted on the group of timber distribution poles installed in the experimental test bed, the poles were removed from the test bed and their actual condition below the ground line was profiled through destructive analysis. In addition, materials testing was performed on the poles to characterize engineering properties including the longitudinal elastic modulus, density, and moisture content. The removal process began by reattaching the crane to each pole top individually and using a chainsaw to remove the top of the pole from its base at approximately 6 foot

above the ground line. Removing the top portion of the poles, which were reserved for the materials testing, made it easier to maneuver the embedded region of the poles during destructive characterization. Next, a through hole was drilled through the top of the in-situ pole sections and an overhead crane was used to remove the section of poles still installed in the test bed without introducing any further damage or section loss to the pole specimens. Prior to removal from the test bed, lines were drawn on the bottom sections of the poles to document the axes where sensors were placed and where strikes were applied to the pole during each of the nondestructive tests performed.

3.3.1 Image Analysis of Pole Sections Below Ground Line

A horizontal band saw was used to cut the bottom section of the pole into cross sectional slices approximately 2 to 3 inches in depth, as shown in Figure 3.12. Specifically, slices were cut from the sections of the pole showing decay and extended from these decayed areas to approximately 6 inches above the ground line of each pole. Each slice was photographed on a white posterboard background using a Nikon D5100 digital camera that was positioned on a tripod so as to be looking down onto the cross section (Figure 3.13). A high contrast square was included in each photograph to serve as a dimensional reference and to calibrate subsequent digital image processing of the cross sectional slices. Photographs of the cross sectional slices for each pole are provided in Appendix C. On these images, colored arrows are used to indicate the azimuth locations for sensor and impact locations in the nondestructive tests. Red arrows indicate the location of an accelerometer used in the vibrational tests and

the location of the microphone during the acoustic resonance testing. Blue arrows indicate the location of the second accelerometer used during the vibrational testing. Green arrows indicate the location of the array of sensors used in the guided stress wave testing and one of the strike locations while black arrows indicate the second impact location used in the guided wave testing.

FIGURE 3.12: Destructive characterization of Pole 8 with band saw

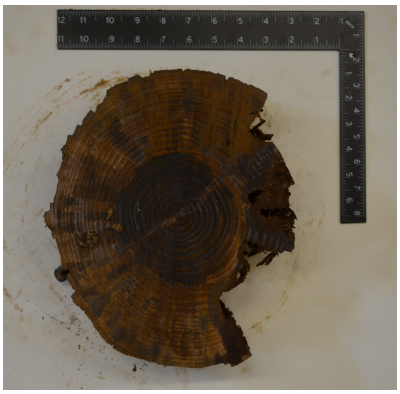

FIGURE 3.13: Photograph of a slice from a tested pole used to destructively determine geometric section properties below the ground line

The photographs of the slices were analyzed using a developed MATLAB script to estimate section properties through digital image processing. This script first converted each photograph to a binary image and built-in functions from the image analysis toolbox were used to automatically trace the boundary of the slice as well

as the boundary of the reference square (Figure 3.14). The areas within the closed polygons of the traced regions were then computed in teams of total number of image pixels. Likewise, the second moments of inertia (I_x and I_y) were computed with respect to the centroid of the slice area in pixel widths^4 . The actual physical area of the construction square in square inches was measured and then used to convert the pole area from pixels to in^2 and the second moments of inertia to in^4. The effective diameter (d_{eff}) and circumference (C_{eff}) of the slice were also determined by treating the cross section as an ideal cylinder. The calculated effective pole diameters and the image processed section properties were plotted for each pole versus the depth of the pole below ground line (Figure 3.15). These plots and calculated section properties are presented in Appendix D beside the photographs taken of the condition of each pole in the region below the ground line.

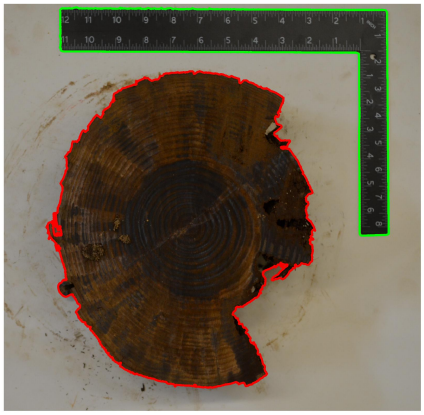

FIGURE 3.14: Image analysis applied to profile perimeters of slice and reference square

Based on the observed condition of the poles prior to installation in the experimental test bed, the primary type of decay present in the poles is shell rot. With

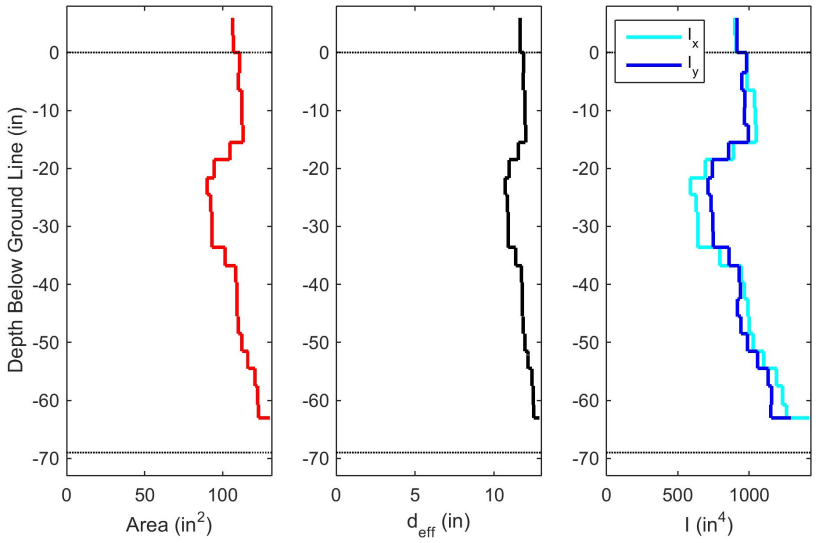

FIGURE 3.15: Profiling section properties below the ground line by plotting results of image analysis from slices

shell rot, decay occurs from the exterior of the pole and spreads inward, which results in significantly larger reductions in section properties in comparison to heart rot or pocket rot. This is suggested when comparing Tables 1 through 3, which equate internal pocket decay, heart rot, and external pocket decay to a reduction in pole circumference. For instance, when heart rot results in a pole having a healthy shell of wood that is 3 inches thick, the corresponding reduction in circumference equals 2 inches. If this occurs in a pole with a ground line circumference of 26 inches, then a heart rot area of approximately 315 square inches is equated to a shell rot area of approximately 215 square inches, which is significantly smaller. Based on the image analysis and the visual examination of the poles prior to installation, each pole was classified as healthy, moderately decayed, or severely decayed. Listed from least decayed to most decayed: Poles 7, 3, 5, and 6 were classified as healthy, Poles 2, 4, and 1 were classified as moderately decayed, and Poles 9, 10, and 8 were classified as

severely decayed.

3.3.2 Materials Testing

In accordance with Test Method D of ASTM D2395, a 2 inch diameter Forstner bit was drilled into each pole and the shavings were collected and weighed. After drilling, the depth of the Forstner bit hole was measured and was used along with the bit diameter to calculate the volume of the shavings removed from the pole. The pole density was calculated by dividing the sample weight by the sample volume. The moisture content of the pole was determined by drying the shavings collected from the pole for at least 24 hours in an oven heated to 217°F, as described by Test Method A of ASTM D4442. After weighing the dry shavings, Equation 7 was used to calculate the percentage moisture content (MC) of the pole using the original mass of the shavings (W_o) and the oven-dry mass of the shavings (W_d) .

$$MC = \frac{W_o - W_d}{W_d} \times 100 \tag{7}$$

To develop an estimate of the longitudinal elastic modulus (E_L) of each pole, the top portions that were previously set aside were nondestructively evaluated using the sonic-echo, or impact-echo, technique described in section 2.2.1.2. A PCB Model 333B52 accelerometer was used to measure stress wave reflections produced by impacts with a PCB Model 086C03 impact hammer. First, the accelerometer was fastened to one end of each pole segment at the center of the cross section using tacky wax. Next, the impact hammer was used to strike the pole in the center of the

TABLE 6: Summary of measured density (ρ), moisture content, longitudinal wave speed (C_p), and estimated longitudinal elastic modulus (E_L) of tested poles

Pole	ρ **(lb/ft^3)**	**Moisture (%)**	C_p **(in/s)**	E_L **(ksi)**
1	39.25	11.2	187,763	1,867
2	43.76	13.2	210,565	2,617
3	38.93	9.6	188,650	1,869
4	39.25	10.8	199,180	2,101
5	41.50	12.7	207,500	2,411
6	33.14	11.5	188,500	1,588
7	29.92	8.0	209,720	1,775
8	34.10	7.4	205,250	1,938
9	35.07	7.2	202,613	1,942
10	41.50	6.9	210,375	2,478

	ρ **(lb/ft^3)**	**Moisture (%)**	C_p **(in/s)**	E_L **(ksi)**
Average, $\bar{x}$	37.64	9.9	201,012	2,059
Standard Deviation, σ	4.38	2.4	9,461	336

cross section and the resulting stress wave reflections were measured over a 0.1 second duration with a sampling rate of 204.8 kHz. A total of five strikes were applied to each pole section. The collected data was analyzed using a fast Fourier transform, which allowed for direct identification of the frequency of the stress wave reflections. The longitudinal wave speed for each pole (C_p) was determined using Equation 2. In this estimation the in situ density determined by ASTM D2395 sampling was used, while an estimated Poisson ratio of 0.2 was used based on the average LT and LR Poisson ratios of southern yellow pine with similar moisture contents suggested by a publication by the Federal Highway Administration [Murray, 2007]. The wave speeds, elastic modulus, density, and moisture content of each pole are presented in Appendix B and summarized in Table 6.

CHAPTER 4: EXPERIMENTAL MODAL ANALYSIS OF POLES AND DEVELOPMENT OF ANALYTICAL MODEL

In this chapter, an experimental modal analysis of the set of ten full-scale timber distribution poles is performed to produce a database of vibration-based measurements suitable for developing and assessing condition assessment techniques. Experimental modal analysis performed with a roving impulse hammer is first presented to characterize the typical natural frequencies and associated mode shapes for a representative distribution pole partially embedded in a soil foundation. In addition, a Rayleigh-Ritz model is developed to provide a method of analytically predicting the natural frequencies and mode shapes of timber distribution poles partially embedded in an elastic soil. This model is verified by comparing the predicted modal parameters to those obtained from the experimental testing. Then, knowledge of the natural frequencies and mode shapes from this preliminary testing and the developed model was used to aid in the interpretation of test data collected from each of the poles using the rapid vibration testing method described in the previous chapter. Specifically, the natural frequencies and damping ratios for each of the ten poles are estimated for both the unsaturated and saturated soil conditions using a system identification routine.

4.1 Experimental Modal Analysis of a Representative Timber Pole

Prior to performing the rapid vibration-based nondestructive testing, experimental

modal analysis was conducted on one of the timber distribution poles installed in the experimental test bed in order to estimate the natural frequencies, relative damping ratios, and mode shapes of a structurally sound pole with typical embedment. Specifically, this testing was performed on Pole 7 since this pole was relatively new and deemed to be structurally sound. The testing performed utilized a stationary pair of PCB Model 333B52 accelerometers and a roving PCB Model 086D20 Impulse Hammer with a soft tip. The stationary locations of the two accelerometers and the locations where impulse excitation was applied with the hammer are shown in Figure 4.1. Roving impulse hammer testing leverages Maxwell's Reciprocity Theorem. The vibration response is measured at a fixed location for a series of impulse forces applied at different degrees of freedom. By reciprocity, the measured responses correspond to the expected response if the impulse excitation was applied at the location of the accelerometer and the accelerometer was positioned at each of the impulse locations [Fung, 1965]. This approach allows for experimental modal analysis to be conducted with a limited number of sensors and by moving the location of the impulse hammer, which is easier than moving and re-bonding the accelerometer.

A National Instruments PXIe-4497 dynamic signal analyzer was used to provide signal conditioning and to convert the analog signals from the accelerometers and impulse hammer to digital data. Measurements were collected with 24-bit resolution at a 1kHz sampling rate over a 5 second duration for each impulse. A reference trigger was used for sampling to ensure a consistent pre-trigger sampling duration for each response obtained. The data collected was preprocessed to remove voltage offsets and convert the voltage measurements to physical units. Then, the time histories were

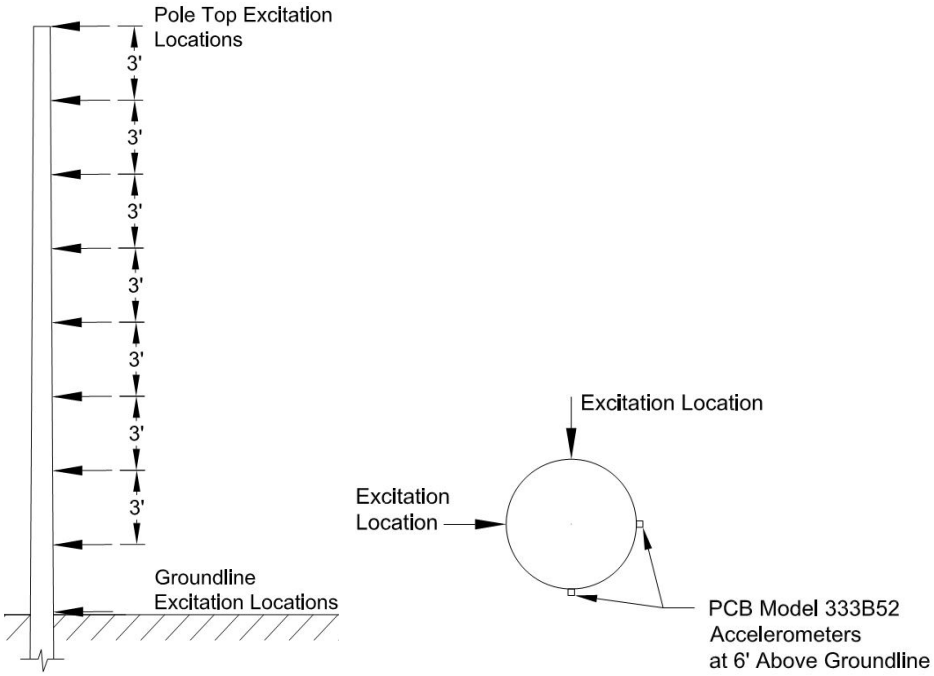

FIGURE 4.1: Locations of accelerometers and impulse excitations during experimental modal analysis of Pole 7

converted to frequency domain using the fast Fourier transform (FFT). Using the frequency domain data, FRFs were developed for each input-output measurement pair using the H_1 Estimator. The H_1 Estimator, shown in Equation 8, uses the frequency spectra for the input force (X) and output acceleration (Y) to estimate the FRF and is recommended for experimental modal analysis conducted with an impulse hammer [Brandt, 2011].

$$H_1 = \frac{S(X). * S(Y)}{S(X). * S(X)} \tag{8}$$

Each of the FRFs computed for each input-output measurement pair were then averaged and the inverse fast Fourier transform was applied to convert the data back to time domain as impulse responses. The combined deterministic-stochastic subspace state-space system identification routine was then used to estimate the natural

frequencies, damping ratios, and mode shapes of the pole from the impulse responses [Van Overschee and De Moor, 2012]. To provide a basis for averaging, five estimates were obtained from different model orders when performing the system identification routine. From the impulse responses, the estimated mode shapes associated with each natural frequency were normalized in amplitude and phase using the modal scale factor (MSF) presented in Equation 9, where ψ_a and ψ_b represent the two mode shape vectors being scaled in reference to each other. The Modal Assurance Criterion (MAC) was calculated for each normalized mode shape using Equation 10 to determine the degree of consistency between the mode shape vectors. Only consistent estimates of the mode shape vectors, or those with MAC values of 90% consistency or higher, were averaged together to determine the mode shapes and the associated natural frequencies.

$$MSF = \frac{\{\psi_a\}^T \{\psi_b\}}{\{\psi_b\}^T \{\psi_b\}} \tag{9}$$

$$MAC = \frac{|\{\psi_a\}^T \{\psi_b\}|^2}{\{\psi_a\}^T \{\psi_a\} \{\psi_b\}^T \{\psi_b\}} \tag{10}$$

Figure 4.2 presents the corresponding mode shapes obtained from the experimental modal analysis of Pole 7. As with the estimated natural frequencies, the mode shapes are very similar for each direction of bending, which is expected for elements that are generally symmetric in geometry and boundary conditions, such as timber poles. Furthermore, significant displacements at ground line were identified in the higher frequency mode shapes, which renders the use of a simplified analytical model with

TABLE 7: Estimated natural frequencies (f_n) and damping ratios (ζ) of Pole 7 obtained through experimental modal analysis

	Axis 1		Axis 2	
	f_n (Hz)	ζ (%)	f_n (Hz)	ζ (%)
Mode 1	2.84	2.33	2.92	0.10
Mode 2	15.92	0.67	16.32	0.43
Mode 3	42.44	0.74	43.01	0.56
Mode 4	79.95	1.05	80.78	1.00
Mode 5	127.93	1.61	127.93	1.61
Mode 6	184.51	1.68	185.42	1.25
Mode 7	248.90	1.76	249.58	2.02

either idealized fixed or pinned ground line boundary conditions as inappropriate. Table 7 presents the natural frequencies (f_n) and damping ratios (ζ) obtained for each measurement axis after performing the averaging of the modal parameter estimates. The results indicate that the natural frequencies for each bending axis are nearly identical through the first seven modes. Furthermore, the natural frequencies are so closely spaced that the identification of unique estimates for each direction was often difficult to obtain. For instance, the fifth mode could not be uniquely identified for each bending axis and so the estimates presented in Table 7 and Figure 4.2 include interactions between the bending modes in each direction. From the results of this analysis, it was determined that the rapid vibration testing for determination of the natural frequencies of each of the 10 poles could be conducted by measuring only one bending axis due to the symmetry of the poles. However, it should be noted that in field installations, the effects of eccentrically located mass of supported electrical equipment and the mass and stiffness of the power lines would likely result in different natural frequencies in each direction.

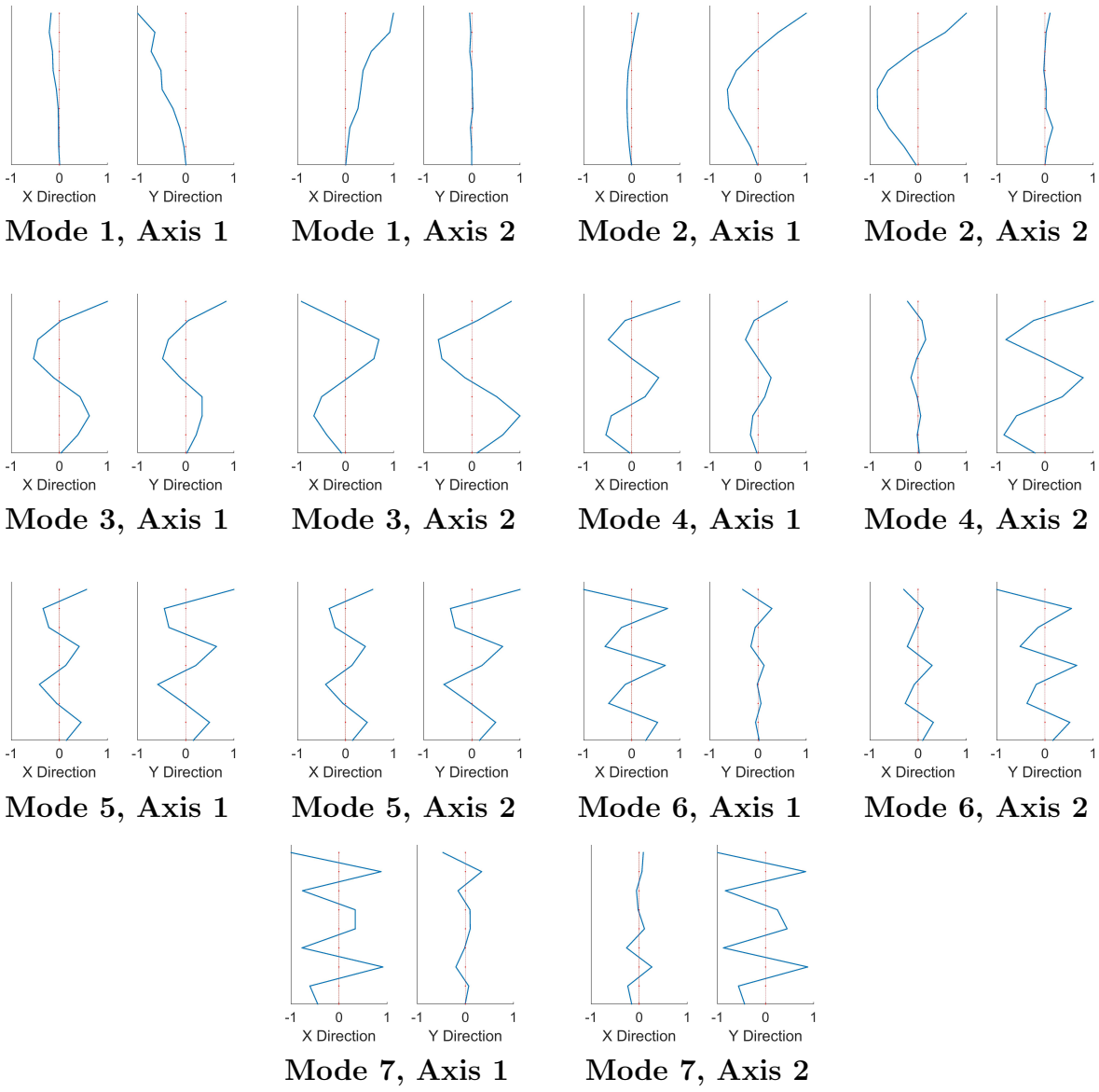

FIGURE 4.2: Mode shapes of Pole 7 determined through experimental modal analysis

4.2 Development of a Rayleigh-Ritz Model for Estimating Natural Frequencies of Distribution Poles

The Rayleigh-Ritz Method is an approximate method for predicting the natural frequencies and mode shapes of a continuous system model. This method builds on the Rayleigh Method by specifying the assumed deflected shape for each mode as a finite series of basis functions and it provides a more accurate estimation of the modal parameters of a system, especially those associated with the higher natural frequencies [Tedesco et al., 1999]. In both the Rayleigh Method and the Rayleigh-Ritz Method, conservation of potential and kinetic energy is used to solve for a natural frequency of the system model using an assumed mode shape to estimate the maximum potential and kinetic energies. In the Rayleigh Method, a fixed, assumed mode shape is used so only the corresponding natural frequency is approximated. In the Rayleigh-Ritz Method, the mode shapes, $\Phi_j(x)$, are approximated by simultaneously solving for both the coefficients, $C_{i,j}$, of the basis functions, $\varphi_i(x)$, in the finite series used to represent the mode shapes (Equation 11) and the corresponding natural frequencies, ω_j, of the system. This approximation is developed by constructing mass and stiffness matrices that are associated with the potential and kinetic energies, respectively, using the finite series of basis functions. Then, the generalized Eigenvalue problem (Equation 12) is solved by eigenvalue decomposition to solve for the natural frequencies and mode shapes of the system model.

$$\Phi_j(x) = \sum_{n}^{i=1} C_{i,j}\varphi_i(x) \tag{11}$$

$$[K]\{C_j\} = \omega_j^2[M]\{C_j\} \tag{12}$$

A model of a tapered pole with a length of L and a cross section defined by a radius of r_1 at the bottom of the pole and of r_2 at the top of the pole is shown schematically in Figure 4.3. Homogeneous material properties are assumed for the pole, where ρ is the mass density of the pole and E is the longitudinal elastic modulus of the pole. The radius of the pole was idealized to perfectly taper at a constant rate along its length. Due to this taper, the cross sectional radius (r), area (A), and second moment of inertia (I) of the pole varied as a function of the location (x) from the origin of the pole model, which was located at the mid-height of the pole. These geometric section properties were calculated using Equations 13, 14, and 15.

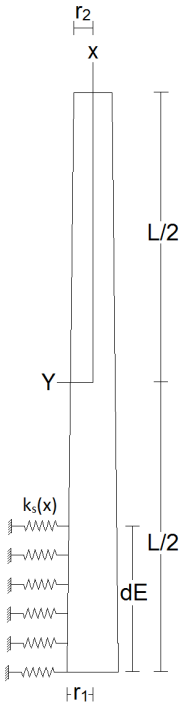

FIGURE 4.3: Analytical Rayleigh-Ritz model of a tapered pole embedded in elastic soil

$$r(x) = \frac{r_1 + r_2}{2} - \frac{r_1 - r_2}{L}x \tag{13}$$

$$A(x) = \pi r(x)^2 \tag{14}$$

$$I(x) = \pi \frac{r(x)^4}{4} \tag{15}$$

As revealed by the experimental modal analysis, an idealized fixed or pinned boundary condition should not be utilized in the model at the ground line of the pole. Therefore, elastic springs were used to approximate the effect of the surrounding soil on the subgrade portion of the modeled pole. The spring stiffness, $k_s(x)$, is assumed to vary linearly with depth of embedment, dE, according to a soil modulus parameter, E_s. The spring stiffness below the depth of embedment is then determined by Equation 16.

$$k_s(x) = E_s\big(1 - \frac{x + \frac{L}{2}}{d_E}\big) \tag{16}$$

Within the Raleigh-Ritz Method, the superposition of basis functions (φ_m) constructs the deflected shape of the pole for each mode shape and are used to compute the corresponding stiffness and mass matrices. When applied to the developed model of an ideal distribution pole partially embedded in soil, the terms in the stiffness and mass matrices are defined by Equations 17, 18, respectively. The accuracy of the Rayleigh-Ritz model depends on the suitability and the number of the basis functions used to develop the model. Polynomial basis functions are often used in simple

Rayleigh-Ritz models for beam-like systems, but were not used in the present study because of the large round-off errors that can occur when high-order polynomial terms are used. These round-off errors result in frequency estimates that converge well up to a certain degree, but beyond which they deviate significantly from the actual values [Ilanko and Monterrubio, 2014]. This limits the prediction accuracy of Rayleigh-Ritz models with polynomial basis functions to only the first few natural frequencies and, for this study, accurate prediction of the first seven on eight natural frequencies was required. The basis functions (φ_m) utilized in this study were selected to include a mix of low-order polynomials and sinusoids for the higher order terms (Equations 19-23). Such an approach has been found to produce more accurate estimates for beam-like systems, particularly for higher-order bending modes [Ilanko and Monterrubio, 2014].

$$K_{i,j} = \int_{-L/2}^{L/2} EI(x)\,\varphi_i''(x)\,\varphi_j''(x)\,dx + \int_{-L/2}^{-L/2+dE} k_s(x)\,\varphi_i(x)\,\varphi_j(x)\,dx \tag{17}$$

$$M_{i,j} = \int_{-L/2}^{L/2} m(x)\,\varphi_i(x)\,\varphi_j(x)\,dx \tag{18}$$

$$\varphi_1 = 1 \tag{19}$$

$$\varphi_2 = \frac{x}{L} \tag{20}$$

$$\varphi_3 = \left(\frac{x}{L}\right)^2 \tag{21}$$

$$\varphi_n = (-1)^{(i/2-1)} sin\frac{(i-3)\pi x}{L}, \text{ for } i = 4, 6, 8, ..., n \tag{22}$$

$$\varphi_n = (-1)^{((i-3)/2)} cos\frac{(i-3)\pi x}{L}, \text{ for } i = 5, 7, 9, ..., n \tag{23}$$

Starting with the fourth basis function and continuing for the n finite number of functions included in the model, the basis functions include cosine and sine waves of decreasing wavelength. When used to model a pole with a constant cross section, the orthogonal nature of the relationship between the cosine and sine functions results in basis functions with terms that reduce to zero, which reduces the complexity of the integrals used to derive the entries in the mass and stiffness matrices [Ilanko and Monterrubio, 2014]. However, since the pole model features a tapered cross section, the benefit of the orthogonality of the basis functions is only obtained when the origin of the model is defined at the mid-height of the pole. When the origin is moved, stiffness and mass integrals can be split into even and odd components, which will reduce to zero for certain intervals due to orthogonality of the functions over the limits of the integrals. Leveraging orthogonality requires that the geometric properties of the pole be separated into the constant, x^2, and x^4 even terms and the x and x^3 odd terms terms of the stiffness and mass matrices. For instance, the orthogonality relationship for constant terms are detailed in Equations 24 to 28.

$$\int_{-L/2}^{L/2} A\, sin\frac{i\pi x}{L}\, sin\frac{j\pi x}{L} = 0 \text{ if } i \neq j \tag{24}$$

$$\int_{-L/2}^{L/2} A\, sin\frac{i\pi x}{L}\, sin\frac{j\pi x}{L} = A\frac{L}{2} \text{ if } i = j \tag{25}$$

$$\int_{-L/2}^{L/2} A\, cos\frac{i2\pi x}{L}\, cos\frac{j2\pi x}{L} = 0 \text{ if } i \neq j \tag{26}$$

$$\int_{-L/2}^{L/2} A\, cos\frac{i2\pi x}{L}\, cos\frac{j2\pi x}{L} = A\frac{L}{2} \text{ if } i = j \tag{27}$$

$$\int_{-L/2}^{L/2} A\, sin\frac{i\pi x}{L}\, cos\frac{j2\pi x}{L} = 0 \tag{28}$$

Using the MATLAB Symbolic Math Toolbox, the integrals for all terms of the mass and stiffness matrices were calculated using generic variables for the pole geometry (L, r_1, r_2), material properties (E, ρ), and soil parameters (E_s, dE). This pre-calculation of the integrals allowed for development of a MATLAB function capable of assembling the mass and stiffness matrices of any pole with given model parameters in a fraction of a second. A total of 250 basis functions were utilized to develop all Rayleigh-Ritz models used in this study. The natural frequencies of Pole 7 were estimated using the Rayleigh-Ritz model and are presented in Table 8. The predictions developed by the model are in strong agreement with the natural frequencies estimated during the full-length experimental modal testing. This agreement serves to experimentally validate the formulation of the Rayleigh-Ritz model as a tool for quickly predicting the natural frequencies of timber poles partially embedded in sand. Furthermore, the mode shapes predicted by the Rayleigh-Ritz model (Figure 4.4) are consistent with those experimentally determined and serve to confirm that the experimentally

measured modes are associated with transverse bending.

TABLE 8: Estimation of the natural frequencies of Pole 7 using the developed Rayleigh-Ritz model

		Experimental Modal Analysis	
	Rayleigh-Ritz Model	Axis 1	Axis 2
Mode 1	2.88 Hz	2.84 Hz	2.92 Hz
Mode 2	15.79 Hz	15.92 Hz	16.32 Hz
Mode 3	42.15 Hz	42.44 Hz	43.01 Hz
Mode 4	80.49 Hz	79.95 Hz	80.78 Hz
Mode 5	129.61 Hz	127.93 Hz	127.93 Hz
Mode 6	187.26 Hz	184.51 Hz	185.42 Hz
Mode 7	249.23 Hz	248.90 Hz	249.58 Hz

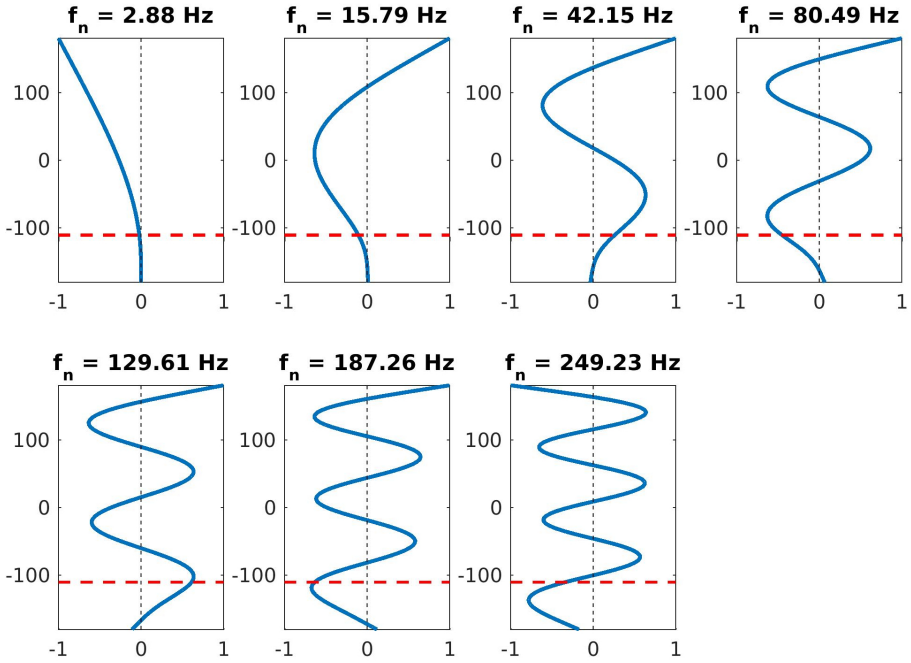

FIGURE 4.4: Mode shapes and natural frequencies of Pole 7 estimated using the developed Rayleigh-Ritz model (dashed line indicates elevation of ground line)

4.3 Experimental Estimation of Natural Frequencies and Damping Ratios of Timber Poles

In order to estimate the natural frequencies of each pole, the data collected from the rapid vibration testing described in Section 3.2.2 was processed using the Eigenvalue Realization Algorithm (ERA). The ERA is an input-output system identification

method originally developed by Jer-Nan Juang that fits impulse response data to a state-space model of a multiple degree of freedom mechanical system [Juang, 1994]. This method is widely used in vibration testing of civil structures and has been found to accurately estimate natural frequencies even when they are closely spaced [Bazan, 2004]. To develop impulse response estimates, the experimental FRFs were developed for each of the sensor measurement axes and then averaged together. By averaging the two directions, the effects of any torsional modes or out-of-plane bending modes potentially excited by the impulse applied during experimental testing are largely eliminated from the measurement signal, thereby leaving only the in-plane bending modes in the response. The averaged FRFs were then windowed to the 0 to 300 Hz frequency bandwidth that was well excited by the impulse hammer. This averaged FRF was then converted to an impulse response using the inverse FFT, after which the ERA method was applied to generate discrete state-space model estimates consistent with the measured impulse response.

A semi-automated routine was developed in MATLAB to apply the ERA method to develop state-space models over a range of different model orders, or degrees of freedom, in order to generate estimates of the natural frequencies of the poles. The routine starts by fitting the data to a state-space model with a model order of ten and performs eigenvalue decomposition on the state matrix to obtain estimates of the natural frequencies and damping ratios for this initial model. Then, the routine increments the model order by one, re-fits the data to the model, and then computes the new modal parameter estimates for this model with an additional degree of freedom. By performing this iterative data fitting, the modal parameter estimates for the

structural modes are improved by averaging and spurious estimates produced by the data fitting algorithm can be identified and removed. In order to ensure consistent estimates, any estimates that occur within ±2.5 Hz of each other are retained and new estimates that occur between ±2.5 Hz and ±5 Hz of the original estimates are discarded to eliminate estimates for cases of mode splitting that occur when the data is over-fit. Once five modal parameter estimates are determined for the fundamental natural frequencies, the routine is ended and the estimates are filtered to remove any with unrealistic values. Specifically, any estimates with corresponding damping ratios larger then 50% were removed from the data set. Then these filtered estimates were averaged by grouping together all estimates within ±5% of each other. The natural frequencies associated with these averaged modal parameter estimates were then plotted over the average FRF for the corresponding pole (Figure 4.5a). A manual review and filtering was then applied through which the estimates consistent with the resonant peaks in the FRF were selected as the final set of natural frequency estimates. The Rayleigh-Ritz model was used in conjunction with this manual review to assist in the selection of the natural frequencies and was particularly useful for confirming the identification of natural frequencies that did not have clearly defined peaks in the FRF. An example of a set of selected natural frequencies estimates superimposed on the measured FRF is presented in Figure 4.5b.

The FRFs developed from the experimental vibration testing on the poles while installed in unsaturated soil conditions are shown in Figure 4.6 and the corresponding natural frequency and relative damping ratio estimates for all the poles are summarized in Table 9. It is important to note that natural frequencies alone cannot be

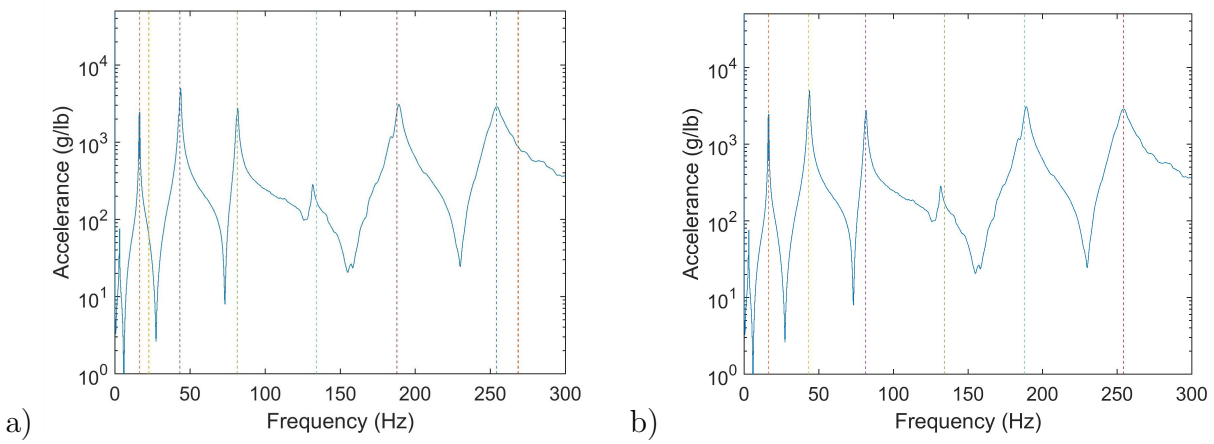

FIGURE 4.5: Results from semi-automated modal parameter identification routine: a) automated determination of candidate natural frequencies; b) manual selection of identified natural frequencies

used to determine the structural condition of the poles, as they are dependent on the density and stiffness of the timber along with the geometric characteristics of the pole and the depth of pole embedment. Of the installed poles, eight natural frequencies were identified in the 0 to 300 Hz measurement bandwidth for Poles 8-10, seven natural frequencies were identified for Poles 1-5 and 7, and six natural frequencies were identified for Pole 6. The three poles with eight natural frequencies present in the measurement bandwidth are the poles for which severe shell rot was present, as corroborated by the destructive characterization of the poles. The inclusion of an additional natural frequency in the measurement bandwidth is a result of a shifting of the natural frequencies, particularly the higher frequencies, down, which occurs due to the loss of structural stiffness as a result of the decay. In contrast, the low number of detected natural frequencies for Pole 6 is a result of its shorter length in comparison to the other installed poles, which increases the relative bending stiffness of the pole. Lastly, the damping ratios for all the poles were also found to exhibit sig-

nificantly higher estimates for the first natural frequency than the subsequent natural frequencies. However, by inspection of the FRF, these damping ratio estimates are likely incorrect and merely reflect the challenges in accurately measuring the fundamental mode. Consequently, the first natural frequency estimate should be considered significantly more uncertain than those with lower damping ratios.

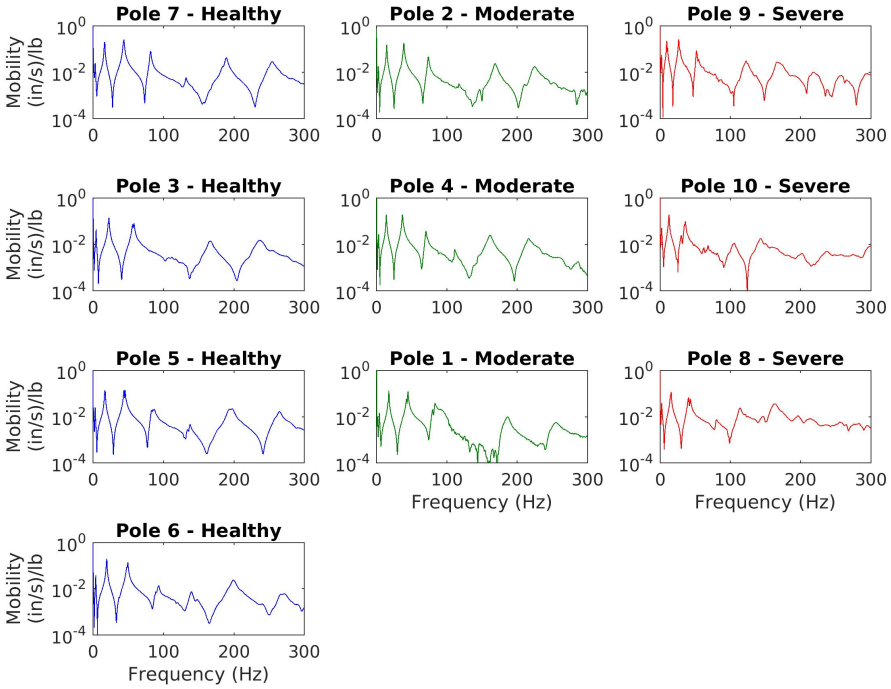

FIGURE 4.6: Frequency response functions developed from experimental vibration testing on poles installed in unsaturated soil

The FRFs developed from the experimental vibration testing on the poles while installed in saturated soil conditions are shown in Figure 4.7. These FRFs were utilized in the ERA semi-automatic routine previously described to estimate the natural frequencies and damping ratios of the poles installed in saturated conditions, which are summarized in Table 10. Figure 4.8 provides the percentage change between the

TABLE 9: Experimental estimates of natural frequencies (f_n) and damping ratios (ζ) for all poles from vibration testing in unsaturated soil

Pole 1

Mode	f_n **(Hz)**	ζ **(%)**
1	4.06	16.0
2	17.55	2.29
3	44.56	1.4
4	81.86	1.5
5	126.31	2.0
6	186.06	1.6
7	254.03	2.8

Pole 2

Mode	f_n **(Hz)**	ζ **(%)**
1	3.09	44.7
2	14.45	2.6
3	39.05	1.3
4	73.79	1.5
5	117.59	1.3
6	167.64	1.3
7	226.05	1.2

Pole 3

Mode	f_n **(Hz)**	ζ **(%)**
1	4.54	11.2
2	22.55	1.6
3	57.09	1.3
4	107.75	5.5
5	166.04	1.8
6	236.26	2.2

Pole 4

Mode	f_n **(Hz)**	ζ **(%)**
1	2.97	17.5
2	13.94	2.1
3	37.22	1.9
4	70.74	1.2
5	111.36	1.2
6	160.30	2.9
7	215.44	1.6

Pole 5

Mode	f_n **(Hz)**	ζ **(%)**
1	3.14	12.7
2	17.23	1.7
3	44.91	1.6
4	84.45	1.5
5	135.51	1.1
6	196.29	1.7
7	267.24	2.1

Pole 6

Mode	f_n **(Hz)**	ζ **(%)**
1	3.93	10.0
2	19.37	2.0
3	48.64	1.5
4	91.13	2.8
5	142.09	2.3
6	198.38	3.4
7	268.92	1.8

Pole 7

Mode	f_n **(Hz)**	ζ **(%)**
1	3.20	10.9
2	16.39	1.5
3	43.38	1.4
4	81.55	0.9
5	131.24	1.3
6	187.34	1.2
7	255.82	1.1

Pole 8

Mode	f_n **(Hz)**	ζ **(%)**
1	2.35	19.4
2	15.75	3.6
3	40.77	2.9
4	79.88	2.9
5	112.16	13.7
6	145.77	3.0
7	164.46	2.3
8	194.67	5.8

Pole 9

Mode	f_n **(Hz)**	ζ **(%)**
1	2.03	23.3
2	9.57	3.6
3	26.51	2.2
4	51.94	1.5
5	80.94	1.9
6	121.54	2.3
7	168.87	2.5
8	217.65	1.8

Pole 10

Mode	f_n (Hz)	ζ (%)
1	2.26	25.6
2	12.69	4.3
3	36.03	1.7
4	67.98	3.9
5	105.12	4.2
6	145.79	2.5
7	201.47	2.1
8	237.08	5.8

natural frequency and damping ratio estimates obtained in unsaturated and saturated soil conditions. These statistics reflect that the poles generally experience a reduction in natural frequency when the pole is installed in saturated soil compared to unsaturated soil. This decrease is expected as the increase in moisture content reduces the stiffness of the soil medium and therefore decreases the overall stiffness of the pole-soil system. This effect of the soil stiffness on the modal parameters is important and must be compensated for within any vibration-based nondestructive assessment strategy developed for pole condition assessment using natural frequencies. In comparison to the change in natural frequencies, the damping ratios experience very significant increases between the unsaturated and saturated soil conditions, and the effect is most significant for the higher natural frequencies. For the severely decayed poles, the damping ratios were found to increase to the extent that the highest natural frequency identified in unsaturated soil conditions was no longer identifiable once the soil was saturated. Due to these large and generally unpredictable changes, it is suggested that the condition assessment strategy should not take into account the damping ratio estimates because they are significantly more sensitive to any change in the soil conditions than any plausible effect that decay in the pole below ground line might have on the damping ratios.

TABLE 10: Experimental estimates of natural frequencies (f_n) and damping ratios (ζ) for all poles from vibration testing in saturated soil

Pole 1

Mode	f_n **(Hz)**	ζ **(%)**
1	3.96	10.2
2	17.13	2.3
3	42.87	1.7
4	80.91	2.9
5	126.05	3.6
6	181.63	4.5
7	251.07	4.4

Pole 2

Mode	f_n **(Hz)**	ζ **(%)**
1	2.88	33.1
2	14.07	2.9
3	37.88	1.6
4	72.16	2.8
5	114.95	3.5
6	167.14	5.8
7	223.82	6.8

Pole 3

Mode	f_n **(Hz)**	ζ **(%)**
1	4.23	6.7
2	21.41	2.6
3	53.61	2.3
4	106.37	12.1
5	161.48	5.8
6	225.81	10.2

Pole 4

Mode	f_n **(Hz)**	ζ **(%)**
1	2.93	12.8
2	13.81	3.0
3	36.18	2.1
4	68.59	3.0
5	110.58	3.1
6	160.81	4.6
7	215.05	6.8

Pole 5

Mode	f_n **(Hz)**	ζ **(%)**
1	3.18	11.4
2	15.84	3.2
3	41.67	1.8
4	78.56	4.6
5	127.84	8.4
6	188.09	7.7
7	262.33	8.0

Pole 6

Mode	f_n **(Hz)**	ζ **(%)**
1	3.74	5.9
2	18.73	2.7
3	47.79	2.9
4	87.17	8.6
5	137.03	6.1
6	199.39	6.4
7	278.91	8.5

Pole 7

Mode	f_n **(Hz)**	ζ **(%)**
1	3.24	10.1
2	16.09	1.7
3	43.14	1.7
4	80.27	2.7
5	130.34	3.7
6	186.71	4.1
7	255.64	6.9

Pole 8

Mode	f_n **(Hz)**	ζ **(%)**
1	2.27	15.4
2	15.47	3.3
3	41.61	2.1
4	80.83	4.0
5	119.61	6.6
6	149.35	6.6
7	–	–
8	–	–

Pole 9

Mode	f_n **(Hz)**	ζ **(%)**
1	2.22	36.2
2	9.54	4.1
3	26.39	2.2
4	51.87	2.0
5	86.32	5.9
6	122.11	6.3
7	164.97	8.1
8	–	–

Pole 10

Mode	f_n (Hz)	ζ (%)
1	2.33	19.3
2	12.73	3.4
3	36.02	3.1
4	66.37	2.9
5	106.71	4.0
6	143.23	6.9
7	–	–
8	–	–

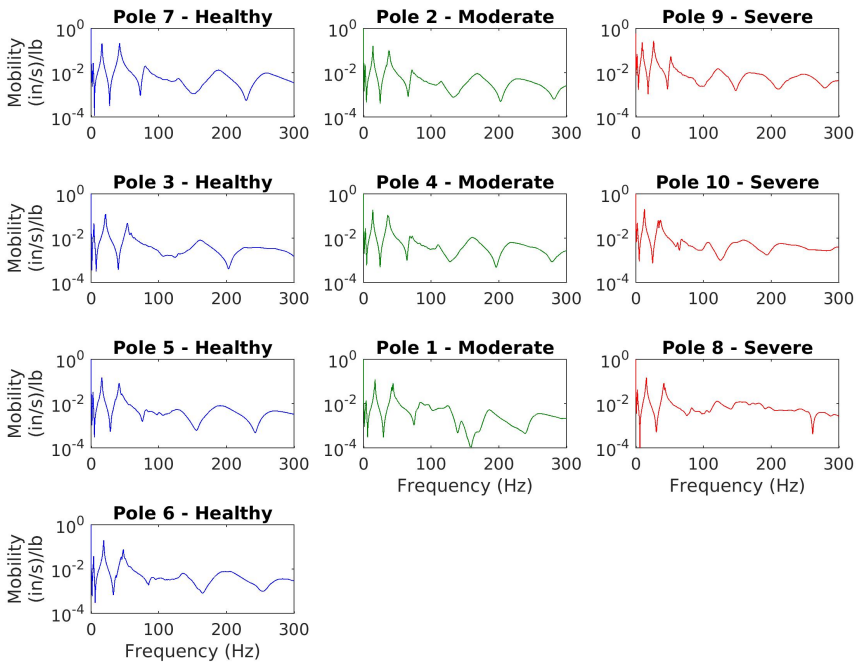

FIGURE 4.7: Frequency response functions developed from experimental vibration testing on poles installed in saturated soil

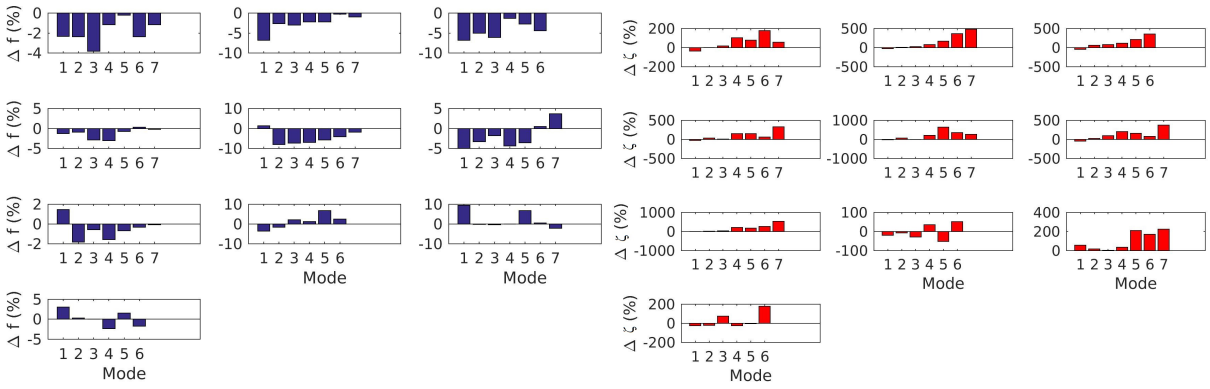

FIGURE 4.8: Percentage difference between natural frequencies (left) and damping ratios (right) estimates obtained in unsaturated and saturated soil conditions for Pole 1 through Pole 10

CHAPTER 5: VIBRATION-BASED CONDITION ASSESSMENT OF TIMBER POLES

In this chapter, the use of structural identification, or model updating, is explored for vibration-based condition assessment. By this technique, optimization strategies are used to calibrate parameters in an analytical model of the structure and the identified values of the parameter assignments are used to assess the likelihood of decay. In this study, two strategies based on structural identification of the previously developed Rayleigh-Ritz model are evaluated. The first method identifies stiffness parameters of the originally formulated Rayleigh-Ritz model, while the second approach expands on the original model by including an additional parameter that models potential decay in the pole.

5.1 Model Updating of Rayleigh-Ritz Model without Explicit Decay Modeling

The elastic modulus of a distribution pole and the stiffness values associated with the soil foundation significantly influence the natural frequencies and mode shapes of the poles. Values of E_L are difficult to precisely determine without physical sampling and testing, as southern pine has a range of plausible elastic moduli, is orthotropic, and the properties are affected by aging. Likewise, the soil in which the poles are installed present variable stiffness that is not readily estimated for rapid condition assessment. Most of the remaining parameters in the model are geometric and can be determined or estimated with greater confidence. Since decay below the ground

line is not explicitly considered in the model, this approach seeks to use the identified elastic modulus of the pole or the identified stiffness of the supporting soil foundation to assess the likelihood of decay.

To do this, the previously described basis functions and the geometric dimensions of each pole were used to calculate the normalized mass and stiffness matrices for one pole. During the optimization routine, linear superposition of the parameterized stiffness matrix was leveraged to provide rapid reconstruction of the mass and stiffness matrices for different E and E_s parameter assignments. Through this approach, the stiffness matrix, K, was calculated for any model using Equation 29, where K^1_{pole} is the contriution to the stiffness matrix from the flexural rigidity of the pole calculated with E set to one and K^1_{soil} is the contribution to the stiffness matrix from the soil springs calculated with E_s set to one.

$$K = EK^1_{pole} + E_sK^1_{soil} \tag{29}$$

To reduce the search space and ensure identification of plausible parameter assignments, bounds were developed for E and E_s for the optimization routine. The established range of allowable E values was based on the average E of the poles that was estimated from the longitudinal wave speed measurements and reported in Appendix B. This average value was calculated to be 2058 ksi and so the bounds for this parameter were established as the range from 50% to 200% of this average, which equates to 1029 ksi to 4116 ksi, respectively. Empirical analysis was conducted to develop the range of E_s, which was established as 1 ksi to 50 ksi [Subramanian, 2008].

In some cases, certain natural frequencies of the poles were not utilized during the optimization routine so as to prevent the results of the routine from becoming skewed. Specifically, the fundamental natural frequency of each pole was not used during the parameter identification due the challenges in accurately estimating this value, as discussed in the prior section on system identification. Likewise the seventh natural frequency of Pole 3 was not used because it was not present within the measurement bandwidth. Additionally, the eight natural frequency for Pole 8 through Pole 10 was not used because of its inaccurate measurement, which is attributed to severe decay present in these poles.

During the optimization routine, the natural frequencies of each pole model were calculated using eigenvalue decomposition and then compared to the experimentally measured natural frequencies to assess the model correlation. To optimize the parameter assignments for each pole, an objective function was developed using the absolute percentage error between the predicted natural frequencies generated by the model and the measured natural frequencies (Equation 30). The calculated natural frequency of the ith mode is represented by $\hat{f}_i$ and the experimentally measured natural frequency is represented by f_i. Lower values of the objective score, J, correspond to E and E_s combinations that result in predicted natural frequencies that are more similar to those determined experimentally. Therefore, the optimal E and E_s combination can be determined by minimizing the objective function through optimization.

$$J(E, E_s) = \sum_{i=2}^{n} \left| \frac{\hat{f}_i - f_i}{f_i} \right| \times 100 \tag{30}$$

A genetic algorithm was selected to perform global optimization using a population size of 100 individuals, an elite count of 5 individuals, and a cross-over rate of 60%. Stopping criteria for this genetic algorithm was set as a fixed number of generations, established by susbequent analysis presented in this chapter. Genetic algorithms mimic the evolutionary process of chromosomes and survival of the fittest to test parameter combinations of a population of candidate solutions and then use the objective scores of those parameter combinations to generate a new population of parameter combinations, or individuals, to assess. Through this evolution, the algorithms generate parameter sets that continually increase in correlation with the measured data until the desired optimization is achieved or, in this case, a specific number of generations is created [Mitchell, 1998]. Following the genetic algorithm, the fmincon constrained local optimization routine was applied to arrive at the minimum of the objective function in the proximity of where the genetic algorithm converged.

5.1.1 Parameter Identifiability

Parameter identification is an inverse method that does not generate a unique solution and, furthermore, does not guarantee that optimization techniques arrive at the global minimum of the objective function. A parameter identifiability study was therefore conducted to determine whether the optimization scheme is capable of correctly determining the unknown parameters (E, E_s) that produce the best correlation to the given set of natural frequencies. This analysis is performed using synthetic natural frequency measurements from an analytical model with randomly assigned E and E_s values to provide a case with exactly known parameter assignments treated as

unknowns. Ten cases of random E and E_s values were used to assess the performance of the optimization routine. Twenty generations were used in the genetic algorithm to identify the parameter assignments by the inverse model. The assigned parameter values are presented in Table 11, along with the corresponding identified parameters ($\hat{E}$, $\hat{E}_s$) determined through the optimization scheme and the percentage error between the assigned and estimated values. Based on the exceptionally low prediction errors obtained for all ten cases, the parameters in the model were determined to be identifiable using the optimization routine employed.

TABLE 11: Random values assigned to uncertain parameters (E, E_s) and identified parameters ($\hat{E}$, $\hat{E}_s$) using the Rayleigh-Ritz model without explicit deterioration modeling

Case	E (psi)	E_s (psi)	$\hat{E}$ (psi)	$\hat{E}_s$ (psi)	%Error E	%Error E_s
1	2979905	51090	2979049	51183	0.029	0.182
2	1358464	70209	1359016	69921	0.041	0.410
3	1214871	89200	1216104	88165	0.102	1.160
4	2463881	95970	2462181	96589	0.069	0.645
5	3982908	55174	3985009	55012	0.053	0.294
6	1943760	14723	1943120	14742	0.033	0.126
7	2749999	15780	2750467	15773	0.017	0.042
8	1559957	26493	1559827	26509	0.008	0.059
9	3296528	84231	3295454	84444	0.033	0.253
10	1662953	26174	1662015	26265	0.056	0.349
				Average	0.044	0.352

5.1.2 Optimization Speed

Required computational time is a significant consideration when determining the number of generations to use for optimization, because computational time increases as the number of generations increases. The optimum number of iterations used by the Rayleigh-Ritz model was determined by evaluating the performance of the optimization scheme when different stopping criteria was set. This analysis was per-

formed using a set of ten analytical models with randomized E and E_s assignments between the prescribed lower and upper bound values. Synthetic data for the natural frequencies of these analytical pole models were calculated and then the genetic algorithm-based optimization scheme was applied for parameter identification of each of the ten models. Estimated elastic moduli values were compared to the initial randomly assigned values and the average percentage error between the two was calculated for each of the generations (Figure 5.1). As expected, more generations used in the optimization scheme resulted in more accurate identification of the parameters, although the benefit of running the optimization for more generations generally follows an exponential decay. The average absolute prediction error, which provides an average of the difference between the predicted and the assigned E and E_s values, was also calculated (Figure 5.2). The prediction errors show that both of the parameters can be estimated on average within $\pm 1\%$ of the randomly assigned values when twenty generations of the Rayleigh-Ritz model are utilized. Based on this analysis, twenty generations of the Rayleigh-Ritz model were utilized in this first approach to analyze the ten timber utility poles tested experimentally in this study.

Figure 5.3 presents the processing time for the genetic algorithm optimization on a desktop computer when applied to the ten poles in this study. Although an individual model can be evaluated on the order of 1/20 of a second, the use of a genetic algorithm with 100 individuals over 20 generations requires evaluation of 2000 Rayleigh-Ritz models, which takes approximately 80 seconds. Faster assessments can be performed

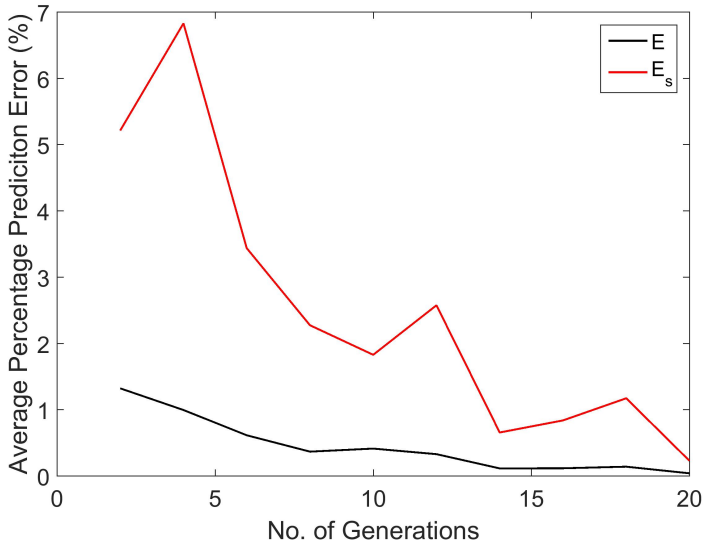

FIGURE 5.1: Average percentage prediction error for the elastic moduli of the pole and the soil with increased generations of the genetic algorithm

with a trade-off in the reliability of the identified parameters.

5.1.3 Results of Parameter Identification

Elastic moduli values determined through parameter identification can theoretically be used to determine the condition of a pole. To do this, the E values produced from the optimization routine are compared to the typical E values for the wood species that the pole is comprised of; values of E that are lower than average indicate that decay is present in a pole. Additionally, a healthy pole will have a corresponding Rayleigh-Ritz model that can closely predict the actual natural frequencies of the pole and that has low prediction errors calculated during the optimization routine. When large prediction errors are calculated even for the best-fit model, it is assumed to be highly probable that the tested pole is significantly decayed.

The parameter identification of E and E_s using the experimentally measured natural frequencies from the set of ten poles is presented graphically in Figures 5.4a

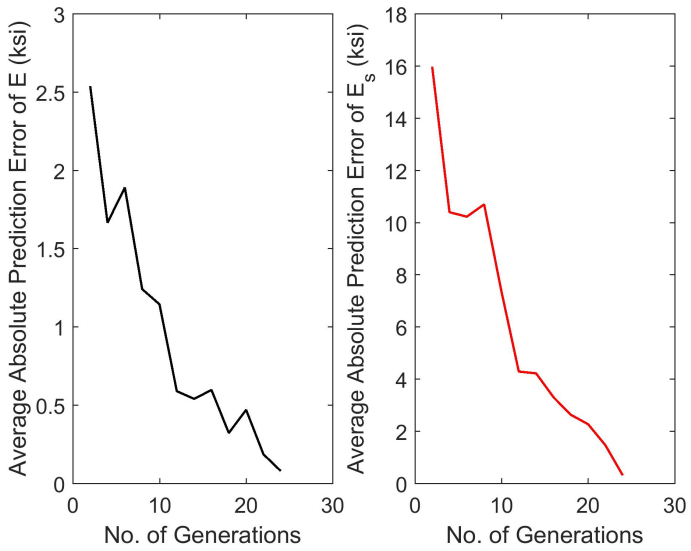

FIGURE 5.2: Average absolute prediction error for the elastic moduli of the pole and the soil with increased generations of the genetic algorithm

and 5.4b, where the poles are arranged by severity of decay. Average prediction errors between the experimental natural frequencies and the final estimation of the natural frequencies of the model are shown in Figure 5.4c. In Figure 5.4, the poles with little or no decay, with moderate decay, and with severe decay as determined through destructive characterization are represented by blue, green, and red bars, respectively. From these figures, it can be seen that the estimated modulus of elasticity for each timber pole is relatively consistent across all ten poles. Similarly, the E_s values estimated from parameter identification are generally consistent across all ten poles. Consequently, there is no apparent, direct correlation between the E and E_s estimations and the amount of decay in the poles. However, analysis of the average prediction errors in the natural frequencies of the calibrated model was found to suggest the presence of significant decay in timber poles, as poles with significant decay exhibited larger natural frequency prediction errors. Furthermore, the analysis sug-

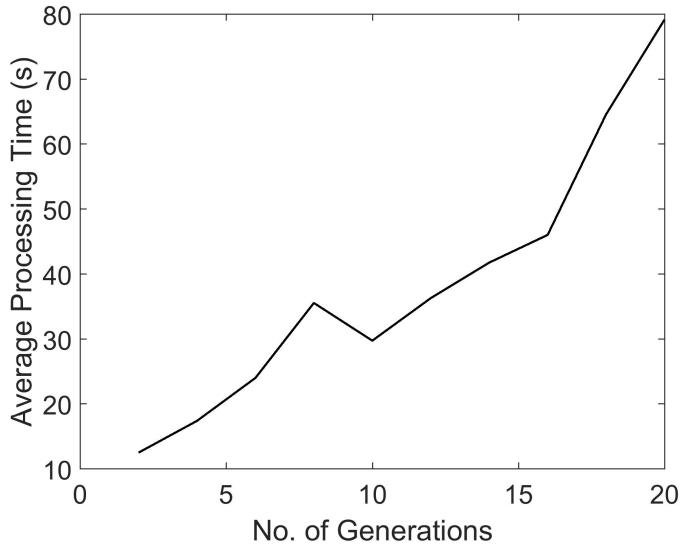

FIGURE 5.3: Average processing time for the parameter identification as a function of the number of generations in the genetic algorithm

gests a challenge in developing clear ranges in prediction errors as thresholds between little, moderate, or significant decay. This challenge and the indirect identification of decay by assessing prediction errors rather than parameters in the model increases the difficulty of precisely determining the condition of a pole using this parameter identification approach. Additional experimental testing and refinement of the approach would be required to further develop this method for practical implementation.

5.2 Application of Rayleigh-Ritz Model with Explicit Decay Modeling

To address the limitation of the original parameter identification method, which does directly not account for the presence of decay in the pole, the Rayleigh-Ritz model was extended to include a parameter to explicitly model the reduction in stiffness and mass below the ground line. To do this, an additional damage parameter (DP) was introduced to the Rayleigh-Ritz model, as shown in Figure 5.5, as a uniform loss of pole mass and stiffness over an exterior area of the pole similar to typical shell

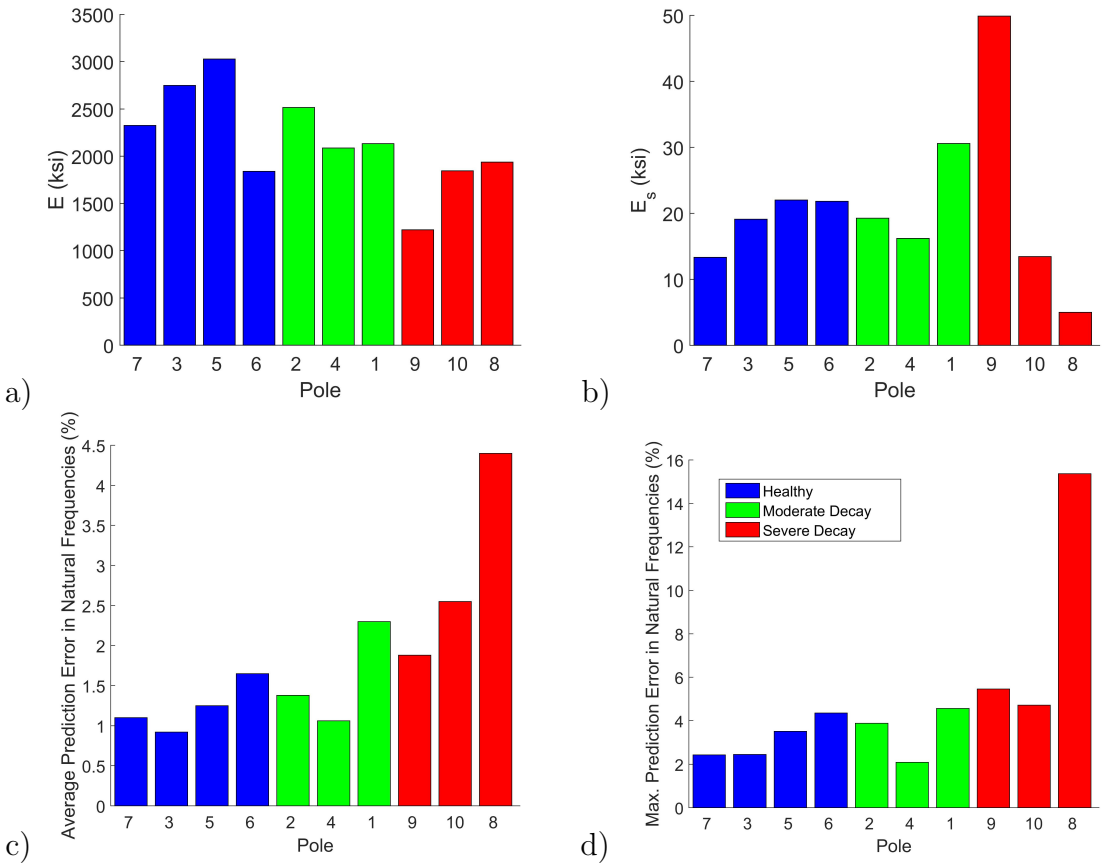

FIGURE 5.4: Results of the parameter identification: a) identified pole modulus of elasticity (E); b) identified soil modulus (E_s); c) average percentage error in natural frequency predictions for optimized model; d) maximum prediction error in natural frequency predictions for optimized model

rot. The damage parameter is defined as the ratio of the change in area resulting from decay, ΔA, to the original cross sectional area, A (Equation 31). For this research, the decay is specifically restricted to a region of the pole that is below-grade, spanning from a prescribed depth d_1 to depth d_2 below grade. To account for the damage parameter in the extended Rayleigh-Ritz model, Equations 32 and 33 were used to calculate the mass and stiffness matrices (M, K) using superposition. In these equations, M^1_{DP} and K^1_{DP} are the mass and stiffness matrices for the region of decay computed with the modulus of elasticity set to one and M_{pole} is the contribution to

the stiffness matrix from the mass of the pole. It should be noted that this assembly of the stiffness matrix is nonlinear in the uncertain parameters, which increases the difficulty of the optimization.

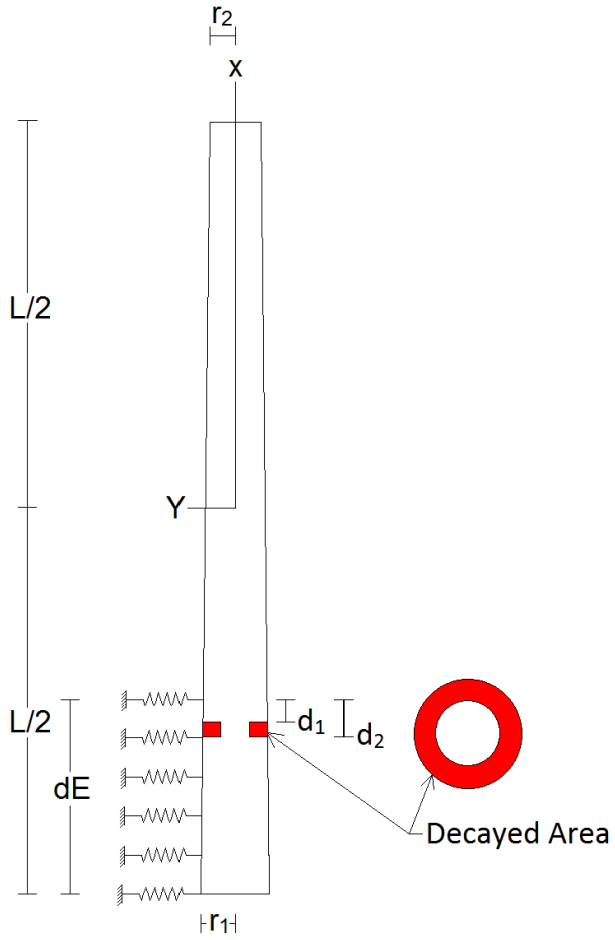

FIGURE 5.5: Extended Rayleigh-Ritz model utilizing damage parameter to represent model deterioration

$$DP = \frac{\Delta A}{A} \tag{31}$$

$$M = M_{pole} - M_{DP}^{1} DP \tag{32}$$

$$K = EK^1_{pole} + E_sK^1_{soil} - EK^1_{DP}(1 - (1 - DP)^2) \tag{33}$$

To reduce the time required to analyze the measurements acquired from the ten timber utility poles tested in the study and to ensure reasonable E and E_s estimates, the range of allowable E and E_s values was bounded to 1000 ksi to 3000 ksi and 5 ksi to 50 ksi, respectively. The revised bounds for these parameters were established from the parameter identification results obtained with the original Rayleigh-Ritz model. The location of decay in the model extended from 6 to 18 inches below grade and was applied uniformly to the cross section of the pole with the search space for the damage parameter bounded to 0 to 0.8. As with the Rayleigh-Ritz model without explicit decay modeling, eigenvalue decomposition was used to calculate the natural frequencies of the model for each parameter combination. These natural frequencies were then compared to the experimentally measured natural frequencies using the same objective function to assess the model correlations. A genetic algorithm with the same settings as before was used with the fmincon local optimizer to identify the E, E_s, and DP associated with the strongest model correlation.

5.2.1 Parameter Identifiability

The introduction of the damage parameter to the Rayleigh-Ritz model required that a parametric identifiability study also be conducted to determine if the optimization could reliably solve this inverse problem with the additional parameter. Ten cases with randomized E, E_s, and DP assignments were used to generate synthetic natural frequency measurements and 24 generations of the genetic algorithm

were then used to identify the parameter assignments of the inverse models. The randomly assigned parameter values are presented in Table 12, along with the corresponding identified elastic moduli parameters ($\hat{E}$, $\hat{E}_s$) and the identified pole damage parameters ($\hat{DP}$). The percentage error between the assigned and estimated values is presented in Table 13. Based on the exceptionally low prediction errors obtained for all ten cases, the three parameters in the model were determined to be identifiable using the optimization routine employed.

TABLE 12: Random values assigned to uncertain parameters (E, E_s, DP) and identified parameters ($\hat{E}$, $\hat{E}_s$, $\hat{DP}$) using the Rayleigh-Ritz model with explicit deterioration modeling

Case	E (psi)	E_s (psi)	DP	$\hat{E}$ (psi)	$\hat{E}_s$ (psi)	$\hat{DP}$
1	3505350	16603	53	3502835	16627	52.9
2	3805279	97089	2	3805420	97045	2.0
3	1241174	95760	68	1242353	94250	68.0
4	3830248	49052	75	3817015	49357	74.5
5	2905041	80228	54	2906357	79803	54.0
6	1144226	15046	61	1143860	15200	61.1
7	1740004	42754	60	1749931	41420	60.8
8	2623618	91658	31	2637043	87775	31.9
9	2975543	79429	53	3964038	80625	52.6
10	3999846	95990	13	3999677	96022	13.0

5.2.2 Optimization Speed

With the additional damage parameter, computation time may be even more significant, as the optimization routine must determine three parameters, which is more challenging. The optimum number of generations of the genetic algorithm optimization was determined by evaluating the performance of the optimization scheme when different stopping criteria was set. This analysis was conducted on a set of ten analytical models with random E, E_s, and DP assignments within the prescribed range

TABLE 13: Percentage error between uncertain parameters (E, E_s, DP) and identified parameters ($\hat{E}$, $\hat{E_s}$, $\hat{DP}$) using the Rayleigh-Ritz model with explicit deterioration modeling

Case	%Error E	%Error E_s	%Error DP
1	0.075	0.145	0.186
2	0.004	0.045	0.000
3	0.095	1.577	0.017
4	0.345	0.622	0.606
5	0.045	0.530	0.078
6	0.032	1.024	0.163
7	0.571	3.120	1.393
8	0.512	4.236	2.786
9	0.289	1.506	0.772
10	0.004	0.033	0.110
Average	0.197	1.284	0.611

for each parameter. The natural frequencies of these models were calculated and then the genetic algorithm-based optimization scheme was applied for parameter identification of each model. The average percentage prediction errors and the average absolute prediction errors between the assigned and identified E, E_s, and DP values across the ten cases were calculated for each of the generations (Figures 5.6, 5.7). The prediction errors show that all three parameters can be estimated on average within $\pm 2\%$ of the randomly assigned values when 24 generations of the Rayleigh-Ritz model were utilized. Based on this analysis, 24 generations of the Rayleigh-Ritz model with deterioration modeling were utilized to analyze the ten timber utility poles tested experimentally in this study.

Figure 5.8 presents the processing time for the genetic algorithm optimization on a desktop computer when applied to the ten poles in this study. Although an individual model can be evaluated in a fraction of a second, the use of a genetic algorithm with 100 individuals over 24 generations requires evaluation of 2400 Rayleigh-Ritz models,

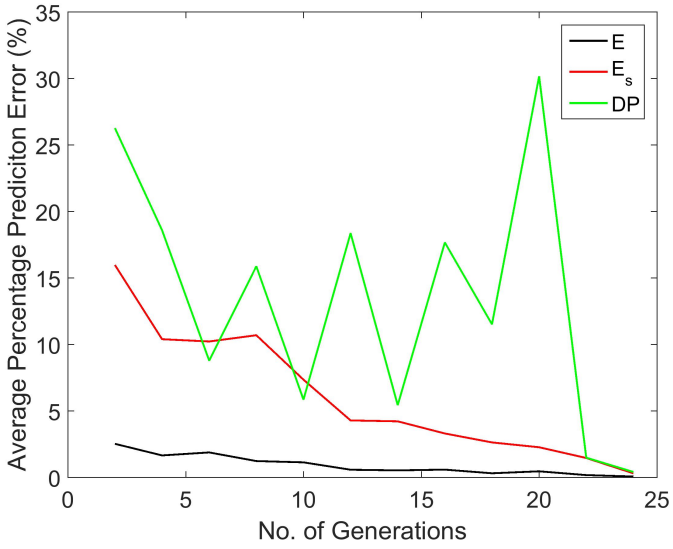

FIGURE 5.6: Average percentage prediction error for the elastic moduli of the pole and the soil and the damage parameter of the pole with increased generations of the genetic algorithm

which takes approximately 125 seconds. Faster assessments can be performed with a trade-off in the reliability in the accuracy of the identified parameters

5.2.3 Results of Parameter Identification

The optimization routine was applied to the experimentally estimated natural frequencies of the ten poles physically tested for parameter identification with the extended Rayleigh-Ritz model. Figure 5.9 provides graphical summaries of the results of this analysis. The elastic stiffness parameters are generally consistent with the parameters identified using the original Rayleigh-Ritz model. The values for E in particular correlate strongly between both models. While trends in the E_s parameter are similar, they were found to vary less significantly with the extended model. This suggests that the previously un-modeled decay below the ground line affects the soil modulus parameter identification more than it affects the identification of the timber

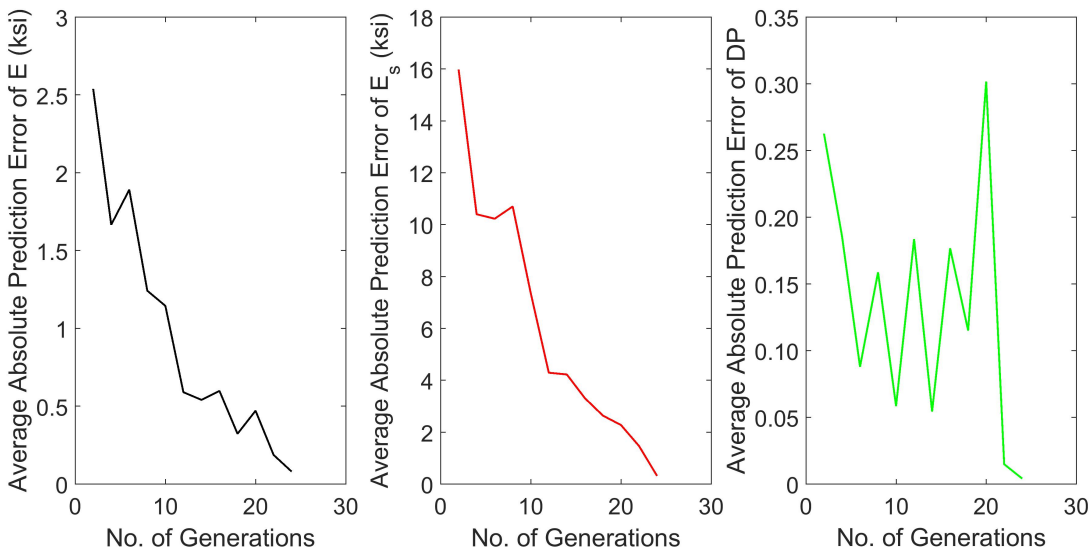

FIGURE 5.7: Average absolute prediction error for the elastic moduli of the pole and the soil and the damage parameter for the pole with increased generations of the genetic algorithm

elastic modulus. Another difference is the slight reduction in prediction errors for the natural frequencies of the optimized model when the optimization was performed on the extended model. This improved ability to predict the natural frequencies reflects the ability of the model with the damage parameter to more closely reflect the actual structural conditions.

The identified damage parameter results for the extended Rayleigh-Ritz model are shown in Figure 5.10, which presents the ten installed timber poles in order of severity of decay, as determined through destructive testing. These identified damage parameters clearly show the reduction in cross-sectional area for the severely decayed poles and even correctly identify the relative severity of the section loss for these poles. Additionally, all four of the healthy poles were correctly identified as having no decay below the ground line. At first glance, the condition assessment of poles with little or moderate decay seems to be less reliable because Pole 1, which was

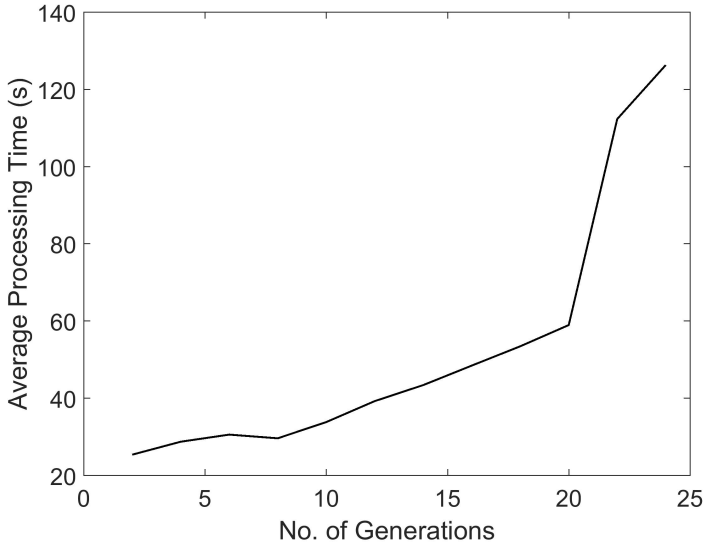

FIGURE 5.8: Average processing time for the parameter identification as a function of the number of generations in the genetic algorithm

characterized as a pole with moderate decay after destructive characterization, was misclassified as a healthy pole. However, as shown in Appendix D, the actual decay in Pole 1 was primarily located between approximate depths of 20 and 35 inches, which is outside the range specified in the extended Rayleigh-Ritz model. Future work could explore methods for improving decay detection in timber poles like Pole 1, where decay is deeper below the ground line than 18 inches. These methods could include introducing additional damage parameters or applying the parameter identification with different user specified depth of decay.

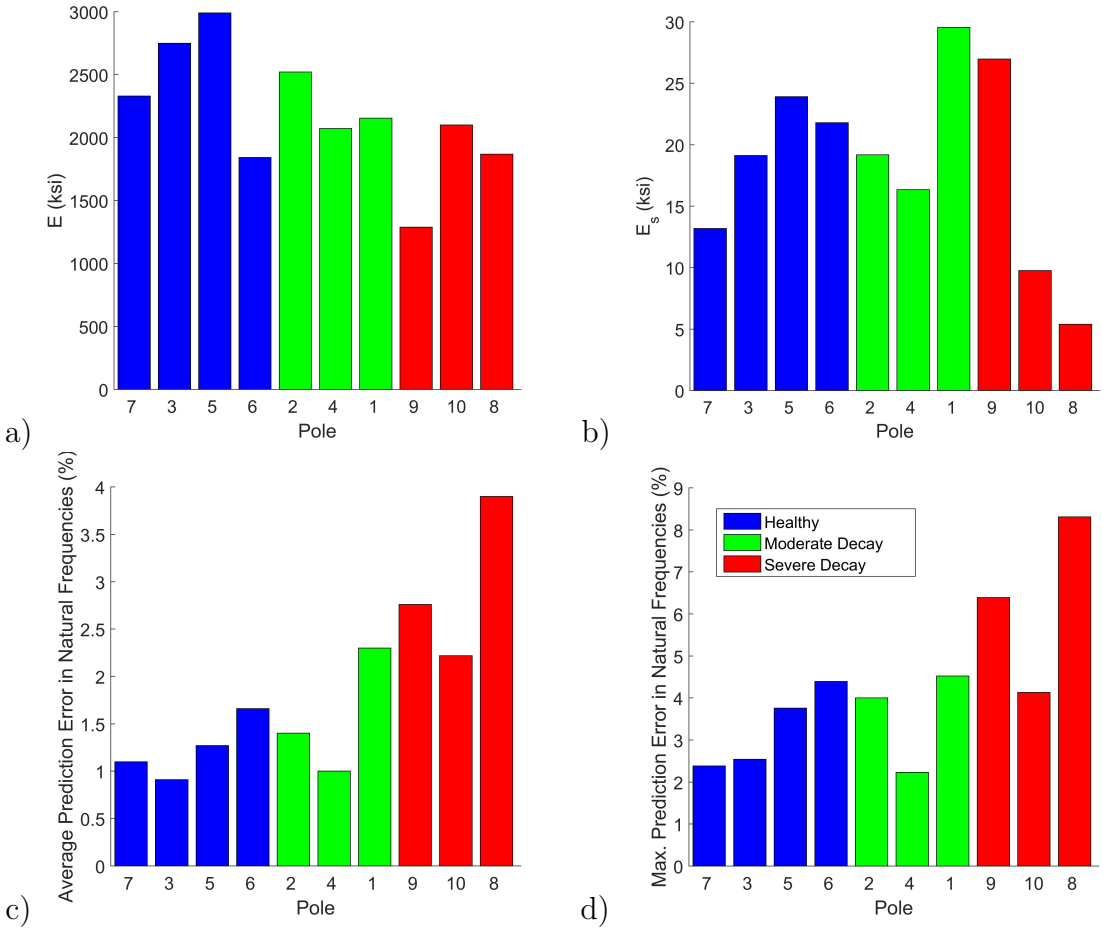

FIGURE 5.9: Results of the deterioration modeling Rayleigh-Ritz method: a) identified pole modulus of elasticity (E); b) identified soil modulus (E_s); c) average percentage error in natural frequency predictions for optimized model; d) maximum percentage error in natural frequency predictions for optimized model

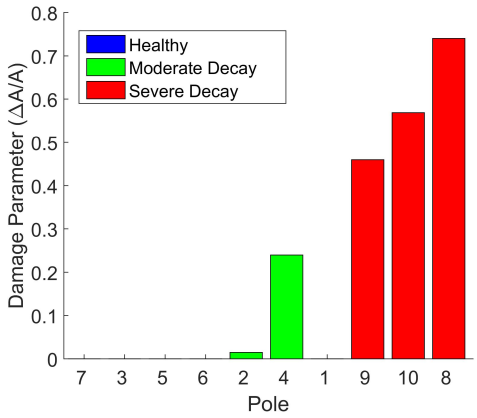

FIGURE 5.10: Damage parameter results obtained with the Rayleigh-Ritz model with explicit deterioration modeling

CHAPTER 6: CONCLUSION

The widespread use of timber utility poles in the electrical distribution network requires that utility workers routinely climb these poles to perform maintenance work when the poles are not accessible by bucket trucks. Such work is dangerous, although power companies and service providers have developed routine pole inspection and maintenance programs to reduce the risk posed to workers. In the United States, OSHA has developed guidelines for pre-maintenance pole inspection assessments, including conventional visual and manual inspection practices. However, these practices have been found effective only about 60% of the time without excavating the soil around the pole, which increases the cost and time required for pole inspection and can expose the pole to decay-causing fungi [Daugherty, 1998]. Reliance on conventional inspection practices continues to be prevalent because of their rapid application, ease of use, and low-cost. Nondestructive evaluation methods applied to pole assessment have been developed in attempt to create inspection tools that are more accurate than conventional methods and can optimize asset management. However, these tools can be costly, time consuming, and can require a trained technician.

In this thesis, several nondestructive evaluation techniques were investigated for their potential to be developed into a low-cost, portable, and rugged instrument for routine field use. These techniques were applied to ten poles of various age and extent

of deterioration installed in an experimental test bed. Analysis of test data was focused on vibration-based methods for condition assessment using natural frequencies measured during the experimental testing. A Rayleigh-Ritz model was developed to quickly predict the natural frequencies and mode shapes of tapered poles installed in soil. This fast running Rayleigh-Ritz model was then used in the development of two parameter identification approaches for condition assessment of the poles. Confirmation of parameter identifiability for both models was produced by using the optimization scheme to identify the parameters from ten sets of synthetic natural frequency measurements from models with randomized parameter assignments. In addition, analyses were performed to allow for assessment of the trade-off between parameter prediction accuracy and computational time.

Validation of the use of parameter identification for condition assessment of decay below the ground line was performed by comparing the parameters and predictions of the calibrated models to the known condition severities of the poles revealed through destructive characterization. No correlation was evident between the amount of deterioration in a pole and the corresponding identified elastic modulus parameters. However, the optimization routines resulted in elastic modulus estimations that were relatively consistent with the average measured elastic modulus of in-situ timber poles. When using parameter identification, the natural frequency prediction errors were determined to be a more apparent indication of pole condition than the identified parameters themselves. However, when introducing an additional parameter to explicitly model decay in the shallow region just below the ground line, the damage parameter values were determined to provide a strong correlation with the measured

severity of decay in each pole. The second method is particularly promising for further development of a low-cost, rapid, and portable nondestructive evaluation tool for distribution poles.

6.1 Recommendations for Future Work

The vibration based condition assessment technique presented in this thesis is suitable for application to in-situ timber utility poles of all sizes installed in unsaturated and saturated soil conditions. However, there are some limitations of the current research that need to be addressed before developing the technology into a tool for future use. In order to expand the capabilities of this application, future research efforts should be aimed toward addressing several additional areas for improved operational and analysis capabilities.

6.1.1 Deterioration Identification

Currently, the Rayleigh-Ritz models assume the potential presence of decay at a single location between the ground line and 18 inches below the ground line. Although deterioration in poles below grade is often within this range, the limited test results indicate that poles with decay outside of this location will not be as easily identifiable and may lead to incorrect condition assessments. Future research could examine the use of alternative or additional damage parameters in the Rayleigh-Ritz model to improve the detection of moderate decay cases.

6.1.2 Controlled Laboratory Experimentation

In order to develop a low-cost, rugged, portable device suitable for rapid in-situ testing of timber utility poles, the number of poles tested in a controlled laboratory environment must be increased. The data collected from this testing can be used to further refine and validate the vibration-based condition assessment techniques. Additionally, the controlled environment may allow for technical or logistic challenges to be more easily identified and then addressed prior to field testing. One such challenge is the development of threshold definitions for the classification of healthy, moderately decayed, and severely decayed poles in terms of the identified elastic modulus of timber, soil condition, the decayed cross sectional area of the pole, and the prediction error of natural frequencies. Such definitions are important because they can decrease processing time and allow for the quick identification of structurally compromised poles.

6.1.3 Field Validation

As current testing has been conducted solely in a controlled laboratory environment, challenges that may be faced in the field have not yet been identified and, therefore, cannot be addressed. For instance, the in-field application will expose the assessment process to environmental factors, such as rain or extreme heat or cold. It is unknown what effect such conditions will have on the testing process, if any, and how these conditions can be best mitigated during testing or during analysis. Furthermore, it is unknown how the mass and stiffness of supported electrical infrastructure will affect the use of the parameter identification method. The development

of a database of field measurements should be pursued to address this question and to verify modifications to the current Rayleigh-Ritz model to account for the influence of this infrastructure. This database could also be used to determine if there is a predictable rate of decay based on timber species, type of preservative, and other environmental conditions that could be used to enhance asset management practices. Furthermore, through development of such a database a baseline for future condition assessments can be established, which can increase the accuracy and reliability of condition assessments.

REFERENCES

[ANSI, 2015] ANSI (2015). Wood poles - specifications and dimensions. Standard ANSI O5.1, American National Standards Institute.

[Baraneedaran et al., 2009] Baraneedaran, S., Gad, E. F., Flatley, I., Kamiran, A., Wilson, J. L., et al. (2009). Review of in-service assessment of timber poles. *Proceedings of the Australian Earthquake Engineering Society, Newcastle*.

[Barclay et al., 1999] Barclay, D., Cooper, P., and Chui, Y. (1999). Evaluation of wood poles using a free vibration technique. *Journal of testing and evaluation*, 27(3):191–195.

[Bazan, 2004] Bazan, F. (2004). Eigensystem realization algorithm (era): reformulation and system pole perturbation analysis. *Journal of sound and vibration*, 274(1):433–444.

[Bibber, 1944] Bibber, H. (1944). The centenary of the morse telegraph. *Electrical Engineering*, 63(12):433–436.

[Birtz, 1979] Birtz, R. E. (1979). Wood pole maintenance. *Journal of Arboricutlure*, 5(3):65–69.

[Brandt, 2011] Brandt, A. (2011). *Noise and vibration analysis: signal analysis and experimental procedures*. John Wiley & Sons.

[Brashaw et al., 2006] Brashaw, B. K., Vatalaro, R. J., Wacker, J. P., and Ross, R. J. (2006). Condition assessment of timber bridges. 1. evaluation of a micro-drilling resistance tool. DTIC Document.

[Burcham et al., 2011] Burcham, D. C., Ghosh, S., Choon, L. E., and King, F. Y. (2011). Evaluation of an infrared camera technique for detecting mechanically induced internal voids in *Syzygium grande*. *Arboriculture & Urban Forestry*, 37(3):93–98.

[Bureau of Reclamation, 1992] Bureau of Reclamation (1992). Wood pole maintenance. 4-6:10–11.

[Conde et al., 2012] Conde, M. J. M., nán, C. R. L., de Hita, P. R., and Gálvez, F. P. (2012). Infrared thermography applied to wood. *Research in Nondestructive Evaluation*, 23:32–45.

[Craighead et al., 2001] Craighead, I., Thackery, S., Redstall, M., and Thomas, M. (2001). Monitoring wood decay in poles by the vibroacoustic response method. *Proceedings of the Institution of Mechanical Engineers, Part C: Journal of Mechanical Engineering Science*, 215(8):905–917.

[Crosby, 2011] Crosby, A. (2011). Special research topic report on current practice in utility distribution poles and light poles.

[Damgaard et al., 2013] Damgaard, M., Ibsen, L., and L.V. Andersen, J. A. (2013). Cross-wind modal properties of offshore wind turbines identified by full scale testing. *Journal of Wind Engineering and Industrial Aerodynamics*, 116:94–108.

[Daniels and Jones, 2009] Daniels, R. A. and Jones, P. D. (2009). *Marketing Your Timber: Forest Products*. Mississippi State University Extension Service.

[Daugherty, 1998] Daugherty, G. L. (1998). The realistic expectation of an in-place wood pole inspection program. *Wood Design Focus*, 9(2).

[Dunlop, 1983] Dunlop, J. I. (1983). Method and means for detecting decay in wood. US Patent 4,399,701.

[Franklin et al., 1990] Franklin, D. E., Murphy, M. W., and Palylyk, R. A. (1990). Apparatus and method for testing wooden poles. US Patent 4,926,691.

[Freeman et al., 2003] Freeman, M. H., Shupe, T. F., Vlosky, R. P., and Barnes, H. (2003). Past, present, and future of the wood preservation industry: wood is a renewable natural resource that typically is preservative treated to ensure structural integrity in many exterior applications. *Forest Products Journal*, 53(10):8–16.

[Fung, 1965] Fung, Y.-c. (1965). *Foundations of solid mechanics*. Prentice Hall.

[Hasenstab et al., 2006] Hasenstab, A., Osterloh, K., and Krause, M. (2006). Testing of wooden construction elements with ultrasonic echo technique and x-ray. In *Proceedings of the 9th European Conference on Non-Destructive Testing, Berlin, Germany*, pages 25–29.

[Hellier, 2001] Hellier, C. (2001). *Handbook of nondestructive evaluation*. McGraw-Hill.

[Hosgood et al., 1989] Hosgood, H., Banks, L., and Beauford, W. (1989). Method and apparatus for testing timbers for disconformity or decay. US Patent 4,858,469.

[Huang et al., 2010] Huang, Y.-H., Ni, S.-H., Lo, K.-F., and Charng, J.-J. (2010). Assessment of identifiable defect size in a drilled shaft using sonic echo method: Numerical simulation. *Computers and Geotechnics*, 37(6):757–768.

[Ilanko and Monterrubio, 2014] Ilanko, S. and Monterrubio, L. E. (2014). *The Rayleigh-Ritz Method for Structural Analysis*. ISTE Ltd. and John Wiley & Sons, Inc.

[Jozi, 2015] Jozi, B. (2015). *Condition Assessment of In-Service Timber Utility Poles Utilizing Advanced Digital Signal Processing and Multi-Sensors Array*. PhD thesis, University of Technology Sydney.

[Jozi et al., 2014] Jozi, B., Dackermann, U., Braun, R., Li, J., and Samali, B. (2014). Application and improvement of conventional stress-wave-based non-destructive testing methods for the condition assessment of in-service timber utility poles. In *Proceedings of 23rd Australasian Conference on the Mechanics of Structures and Materials (December 9th-12th, 2014)*. Southern Cross University.

[Juang, 1994] Juang, J.-N. (1994). *Applied system identification*. Prentice Hall.

[Kim et al., 2000] Kim, Y. R., Ranjithan, S., Donato, P. J., and Murphy, C. M. (2000). Nondestructive evaluation of the structural condition of timber piles. *Final Report, North Carolina Department of Transportation, FHWA/NC/2000-004*.

[Krause et al., 2015] Krause, M., Dackermann, U., and Li, J. (2015). Elastic wave modes for the assessment of structural timber: ultrasonic echo for building elements and guided waves for pole and pile structures. *Journal of Civil Structural Health Monitoring*, 5(2):221–249.

[Krautkrämer and Krautkrämer, 2013] Krautkrämer, J. and Krautkrämer, H. (2013). *Ultrasonic testing of materials*. Springer Science & Business Media.

[López et al., 2014] López, G., Basterra, L.-A., gemma Ramón-Cueto, and de Diego, A. (2014). Detection of singularities and subsurface defects in wood by infrared thermography. *International Journal of Architectural Heritage*, 8(4):517–536.

[Malhotra and Carino, 2003] Malhotra, V. and Carino, N. J., editors (2003). *Handbook on Nondestructive Testing of Concrete Second Edition*. CRC Press.

[Mankowski et al., 2002] Mankowski, M., Hansen, E., and Morrell, J. (2002). Wood pole purchasing, inspection, and maintenance: A survey of utility practices. *Forest Products Journal*, 52(11):43–50.

[Meinlschmidt, 2005] Meinlschmidt, P. (2005). Thermographic detection of defects in wood and wood-based materials. In *14th International Symposium of Nondestructive Testing of Wood, Honnover, Germany (May 2nd-4th, 2005)*.

[Mitchell, 1998] Mitchell, M. (1998). *An introduction to genetic algorithms*. MIT press.

[Morrell, 2016] Morrell, J. J. (2016). Estimated service life of wood poles. Technical Bulletin No. 16-U-101, North American Wood Pole Council.

[Murray, 2007] Murray, Y. D. (2007). Manual for LS-DYNA wood material model 143. FHWA-HRT 04-097.

[OSHA, 2014] OSHA (2014). Methods of inspecting and testing wood poles. Standard OSHA 1910.269 App D, Occupational Safety & Health Administration (OSHA).

[Piazza et al., 2014] Piazza, M., Pompermaier, G. M., and Riggio, M. P. (2014). Method and device for assessing the structural characteristics of installed supporting poles. US Patent 8,630,813.

[Pines, 1997] Pines, D. J. (1997). Detection of utility pole rot damage by measuring the reflection coefficient. *Journal of Nondestructive Evaluation*, 16(1):43–56.

[Popovics, 2003] Popovics, J. (2003). NDE techniques for concrete and masonry structures. *Progress in Structural Engineering and Materials*, 5:49–59.

[Potvin, J., 2014] Potvin, J. (2014). Evaluating wood pole inspection alternatives to conventional visual, sound, and bore practices. Technical Update 3002001279, Electrical Power Research Institute (EPRI).

[RUS, 2011] RUS (2011). Specification for wood poles, stubs and anchor logs. RUS Bulletin 1728F-700, United States Department of Agriculture, Rural Utilities Service (RUS).

[RUS, 2013] RUS (2013). Wood pole inspection and maintenance. RUS Bulletin 1730B-121, United States Department of Agriculture, Rural Utilities Service (RUS).

[SCS, 2013] SCS (2013). *Environmental Life Cycle Assessment of Southern Yellow Pine Wood and North American Galvanized Steel Utility Distribution Poles*. Scientific Certification Systems (SCS).

[Subhani et al., 2011] Subhani, S., Li, J., Samali, B., and Dackermann, U. (2011). Determinations of stress wave velocity in a timber pole using wavelet transform. In *14th Asia Pacific Vibration Conference (December 5th-9th, 2011)*. The Hong Kong Polytechnic University.

[Subramanian, 2008] Subramanian, N. (2008). *Design of Steel Structures*. OUP India.

[Tedesco et al., 1999] Tedesco, J. W., McDougal, W. G., and Ross, C. A. (1999). *Structural Dynamics: Theory and Applications*. Addison-Wesley Longman, Inc.

[Van Overschee and De Moor, 2012] Van Overschee, P. and De Moor, B. (2012). *Subspace identification for linear systems: TheoryImplementationApplications*. Springer Science & Business Media.

[Wyckhuysea and Maldaguea, 2001a] Wyckhuysea, A. and Maldaguea, X. (2001a). A study of wood inspection by infrared thermography, Part I: Wood pole inspection by infrared thermography. *Research in Nondestructive Evaluation*, 13(1):1–12.

[Wyckhuysea and Maldaguea, 2001b] Wyckhuysea, A. and Maldaguea, X. (2001b). A study of wood inspection by infrared thermography, Part II: Thermography for wood defects detection. *Research in Nondestructive Evaluation*, 13(1):13–21.

[Yan, 2015] Yan, N. (2015). *Numerical Modelling and Condition Assessment of Timber Utility Poles using Stress Wave Techniques*. PhD thesis, University of Technology Sydney.

APPENDIX A : CHARACTERISTICS OF EVALUATED TIMBER DISTRIBUTION POLES

TABLE 14: Markings on timber distribution poles installed in geotechnical pit, * *denotes illegible character marking*

Pole Number	**Markings**		
1	DP Co. Patrol 1995		
2	ENERCO 2014	Reject/Replace #2274	A 3-83 SPC 5-30
3	DP Co. Patrol 1996		SBT***
4	DP Co. Patrol 2000, ENERCO 2014, 62	Reject/Replace #3095	
5	DP Co. Patrol 2005		
6	OSMOSE 1988, DP Co. Patrol 2001	Pull Pole #149	* **4 **O* 5-*0
7	AT&T		ATT-6 KOP FL-11-14 SPSK60 5-30
8	ENERCO 2014	Reject/Replace #693	1*
9	DPCO, 37.A, ENERCO 2014	Reject/Replace #1937	***** *-6 SPC 12# 7-*0
10	DP Co. Patrol 2001, ENERCO 2015	Reject/Replace #3995 (Priority)	SWP M-81 SPC-12 5-30

APPENDIX B : POLE GEOMETRIES AND PROPERTIES

Pole 1

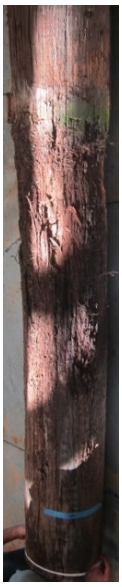

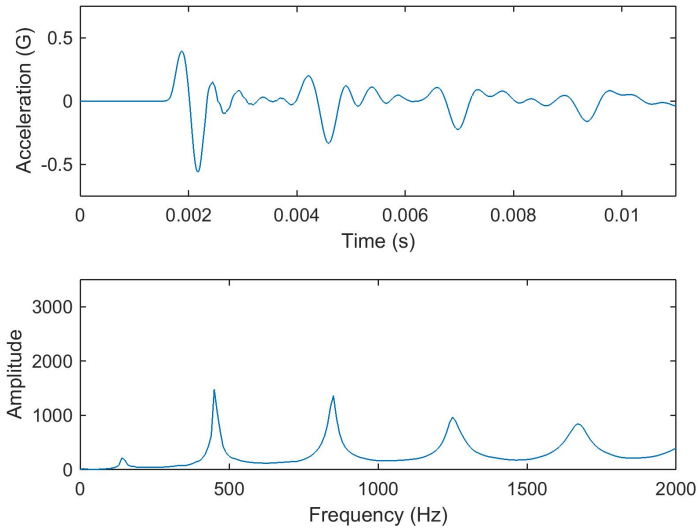

Total Pole Length	360.0 in (9.14 m)
Embedment Depth	69.0 in (1.75 m)
Base Circumference	38.25 in (97.16 cm)
Top Circumference	25.0 in (63.50 cm)
Marking	None
Inspection Tag	None

Length of Wave Speed Specimen	208.625 in (5.30 m)
Frequency of Wave Reflections	450 Hz
Longitudinal Wave Speed, C_p	187,763 in/s (4,769.2 m/s)
In-Situ Density, ρ	39.25 lb/ft^3 (628.8 kg/m^3)
Moisture Content	11.2 %
Longitudinal Elastic Modulus, E_L	1,867 ksi (12,872.5 MPa)

Pole 2

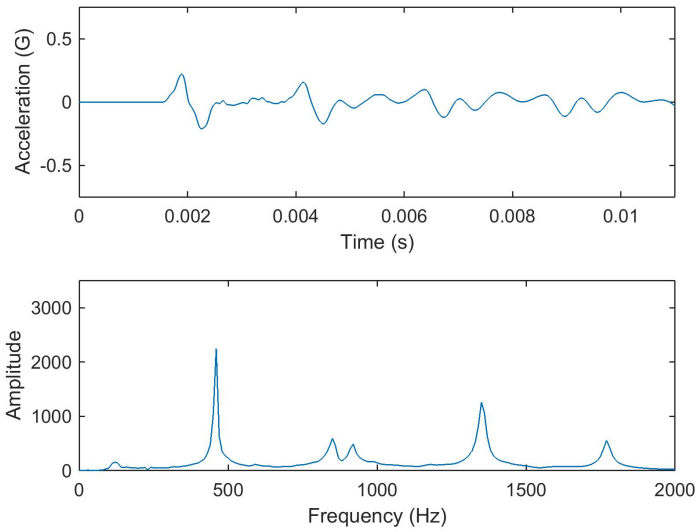

Total Pole Length	359.0 in (9.12 m)
Embedment Depth	52.0 in (1.32 m)
Base Circumference	36.0 in (91.44 cm)
Top Circumference	25.75 in (65.41 cm)
Marking	A 3-83 SPC 5-30
Inspection Tag	Reject/Replace

Length of Wave Speed Specimen	228.875 in (5.81 m)
Frequency of Wave Reflections	460 Hz
Longitudinal Wave Speed, C_p	210,565 in/s (5,348.4 m/s)
In-Situ Density, ρ	43.76 lb/ft^3 (700.9 kg/m^3)
Moisture Content	13.2 %
Longitudinal Elastic Modulus, E_L	2,617 ksi (18,043.6 MPa)

Pole 3

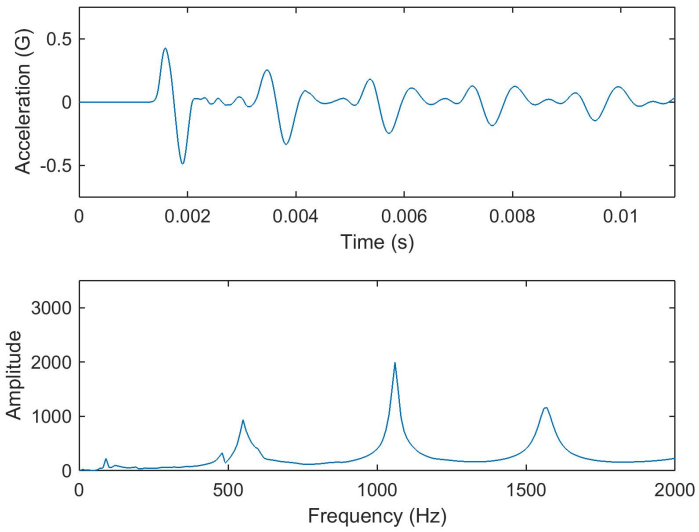

Total Pole Length	321.25 in (8.16 m)
Embedment Depth	70.0 in (1.78 m)
Base Circumference	35.25 in (89.54 cm)
Top Circumference	24.25 in (61.62 cm)
Marking	SBT***
Inspection Tag	None

Length of Wave Speed Specimen	171.5 in (4.36 m)
Frequency of Wave Reflections	550 Hz
Longitudinal Wave Speed, C_p	188,650 in/s (4791.7 m/s)
In-Situ Density, ρ	38.93 lb/ft^3 (623.6 kg/m^3)
Moisture Content	9.6 %
Longitudinal Elastic Modulus, E_L	1,869 ksi (12,886.3 MPa)

Pole 4

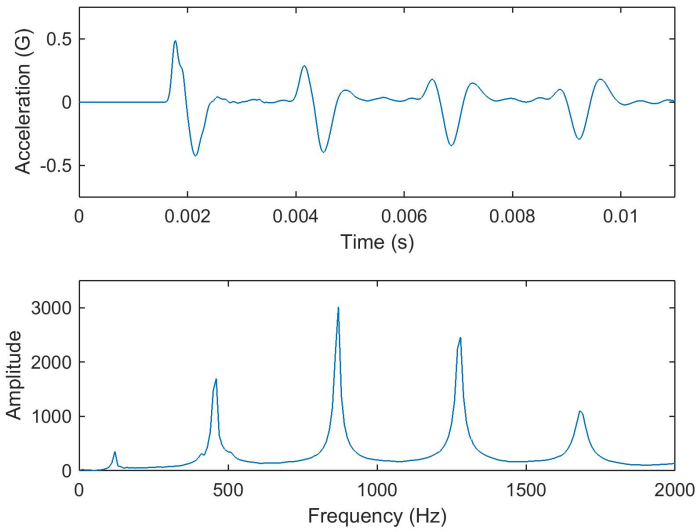

Total Pole Length	360.0 in (9.14 m)
Embedment Depth	65.0 in (1.65 m)
Base Circumference	33.875 in (86.04 cm)
Top Circumference	21.875 in (55.56 cm)
Marking	None
Inspection Tag	Reject/Replace

Length of Wave Speed Specimen	216.5 in (5.50 m)
Frequency of Wave Reflections	460 Hz
Longitudinal Wave Speed, C_p	199,180 in/s (5,059.2 m/s)
In-Situ Density, ρ	39.25 lb/ft^3 (628.8 kg/m^3)
Moisture Content	10.8 %
Longitudinal Elastic Modulus, E_L	2,101 ksi (14,485.9 MPa)

Pole 5

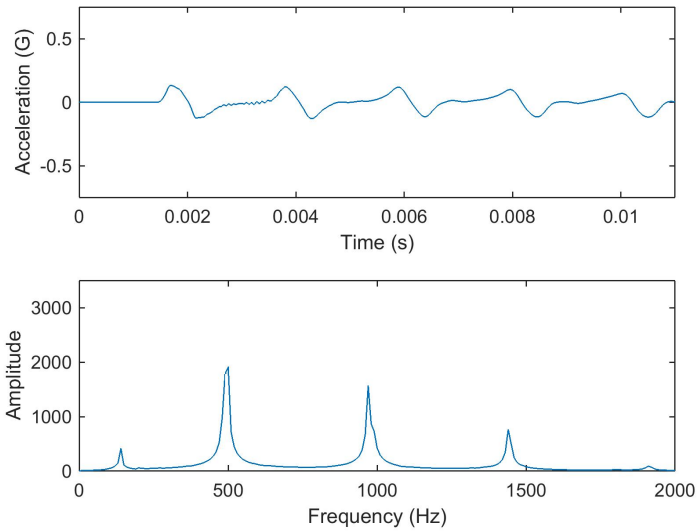

Total Pole Length	358.5 in (9.11 m)
Embedment Depth	70.0 in (1.78 m)
Base Circumference	30.75 in (78.11 cm)
Top Circumference	24.25 in (61.60 cm)
Marking	None
Inspection Tag	None

Length of Wave Speed Specimen	207.5 in (5.27 m)
Frequency of Wave Reflections	500 Hz
Longitudinal Wave Speed, C_p	207,500 in/s (5,270.5 m/s)
In-Situ Density, ρ	41.50 lb/ft^3 (664.8 kg/m^3)
Moisture Content	12.7 %
Longitudinal Elastic Modulus, E_L	2,411 ksi (16,623.3 MPa)

Pole 6

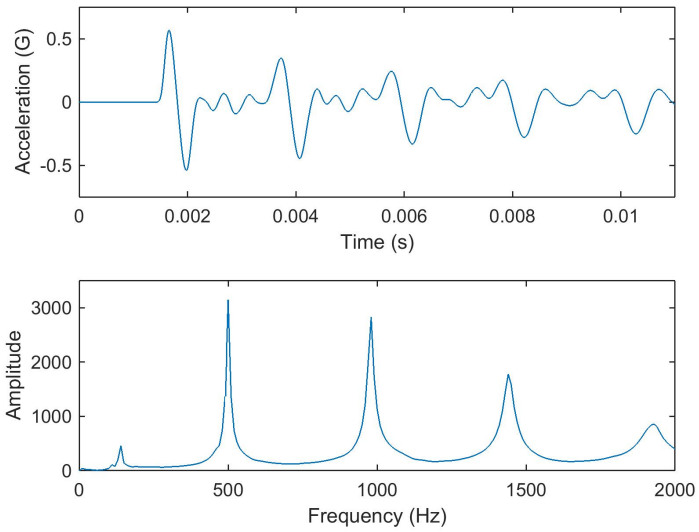

Total Pole Length	341.5 in (8.67 m)
Embedment Depth	76.0 in (1.93 m)
Base Circumference	36.75 in (93.35 cm)
Top Circumference	23.5 in (59.69 cm)
Marking	* **4 **O* 5-*0
Inspection Tag	Pull Pole

Length of Wave Speed Specimen	188.5 in (4.78 m)
Frequency of Wave Reflections	500 Hz
Longitudinal Wave Speed, C_p	188,500 in/s (4,787.9 m/s)
In-Situ Density, ρ	33.14 lb/ft^3 (530.8 kg/m^3)
Moisture Content	11.5 %
Longitudinal Elastic Modulus, E_L	1,588 ksi (10,948.9 MPa)

Pole 7

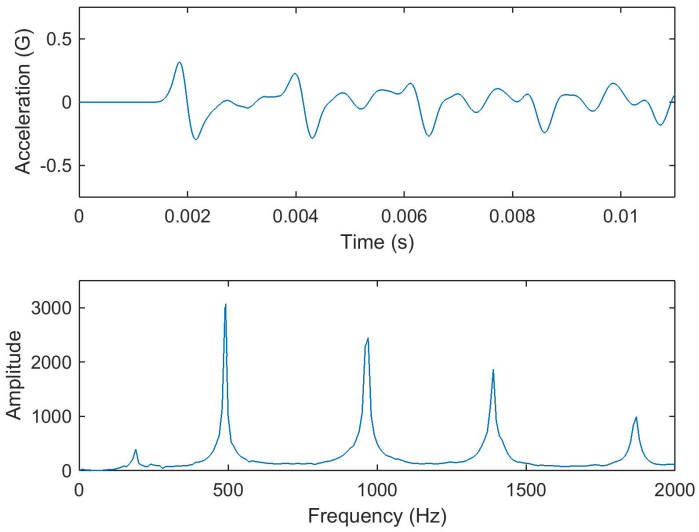

Total Pole Length	361.0 in (9.17 m)
Embedment Depth	70.0 in (1.78 m)
Base Circumference	29.0 in (73.66 cm)
Top Circumference	23.25 in (59.06 cm)
Marking	ATT-6 KOP FL-11-14 SPSK60 5-30
Inspection Tag	None

Length of Wave Speed Specimen	214.0 in (5.44 m)
Frequency of Wave Reflections	490 Hz
Longitudinal Wave Speed, C_p	209,720 in/s (5,326.9 m/s)
In-Situ Density, ρ	29.92 lb/ft^3 (479.3 kg/m^3)
Moisture Content	8.0 %
Longitudinal Elastic Modulus, E_L	1,775 ksi (12,238.2 MPa)

Pole 8

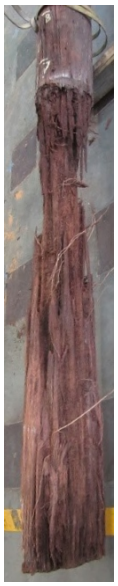

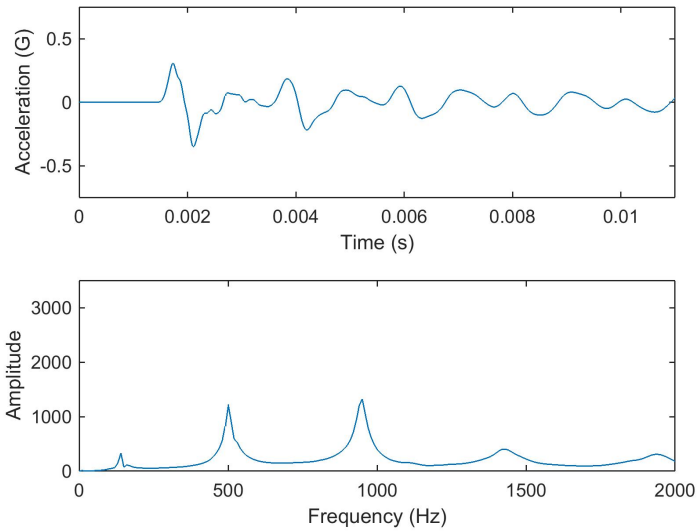

Total Pole Length	360.0 in (9.14 m)
Embedment Depth	78.0 in (1.98 m)
Base Circumference	36.0 in (91.44 cm)
Top Circumference	27.5 in (69.85 cm)
Marking	1*
Inspection Tag	Reject/Replace

Length of Wave Speed Specimen	205.25 in (5.21 m)
Frequency of Wave Reflections	500 Hz
Longitudinal Wave Speed, C_p	205,250 in/s (5,213.4 m/s)
In-Situ Density, ρ	34.10 lb/ft^3 (546.3 kg/m^3)
Moisture Content	7.4 %
Longitudinal Elastic Modulus, E_L	1,938 ksi (13,362.0 MPa)

Pole 9

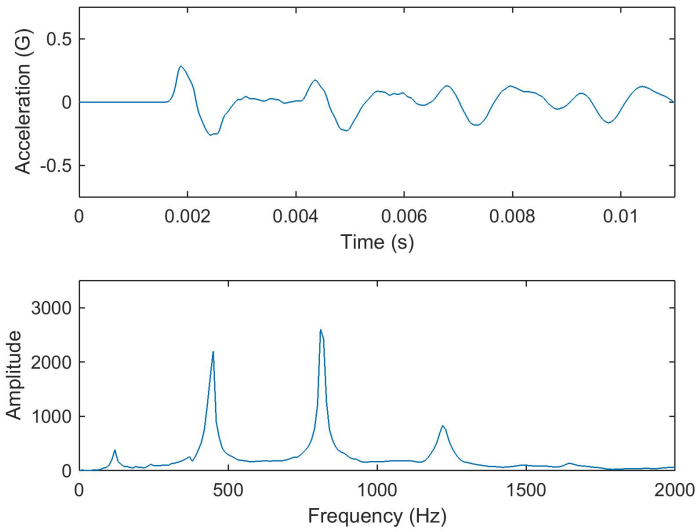

Total Pole Length	357.5 in (9.08 m)
Embedment Depth	60.0 in (1.52 m)
Base Circumference	27.25 in (69.22 cm)
Top Circumference	17.75 in (45.09 cm)
Marking	***** *-6 SPC 12# 7-*0
Inspection Tag	Reject/Replace

Length of Wave Speed Specimen	225.125 in (5.72 m)
Frequency of Wave Reflections	450 Hz
Longitudinal Wave Speed, C_p	202,613 in/s (5,146.4 m/s)
In-Situ Density, ρ	35.07 lb/ft^3 (561.8 kg/m^3)
Moisture Content	7.2 %
Longitudinal Elastic Modulus, E_L	1,942 ksi (13,389.6 MPa)

Pole 10

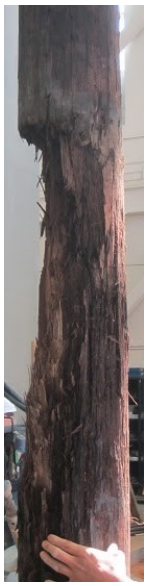

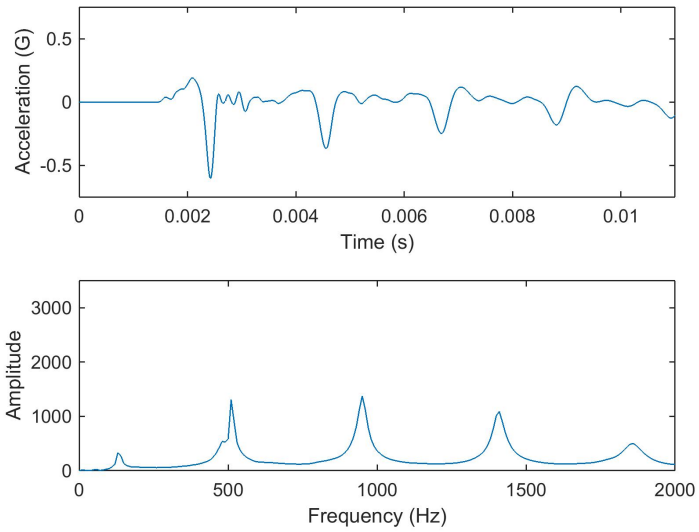

Total Pole Length	356.0 in (9.04 m)
Embedment Depth	76.0 in (1.93 m)
Base Circumference	29.75 in (75.57 cm)
Top Circumference	21.75 in (55.25 cm)
Marking	SWP M-81 SPC-12 5-30
Inspection Tag	Reject/Replace (Priority)

Length of Wave Speed Specimen	206.25 in (5.24 m)
Frequency of Wave Reflections	510 Hz
Longitudinal Wave Speed, C_p	210,375 in/s (5,343.5 m/s)
In-Situ Density, ρ	41.50 lb/ft^3 (664.8 kg/m^3)
Moisture Content	6.9 %
Longitudinal Elastic Modulus, E_L	2,478 ksi (17,085.2 MPa)

Pole 1

6 in. Above Ground

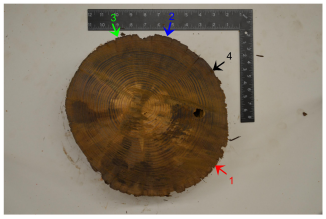

3 in. Above Ground

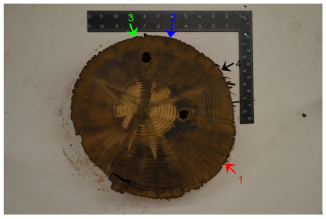

Ground Line

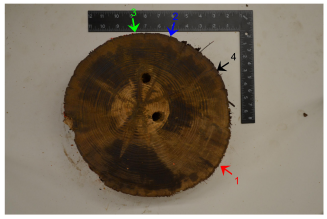

3.5 in. Below Ground

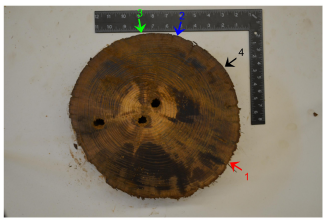

6.5 in. Below Ground

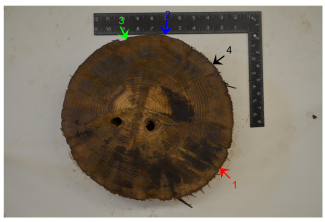

9.5 in. Below Ground

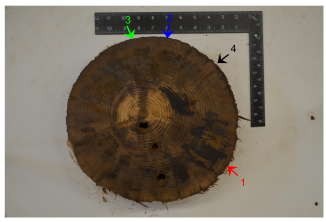

12.5 in. Below Ground

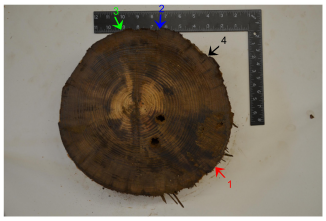

15.5 in. Below Ground

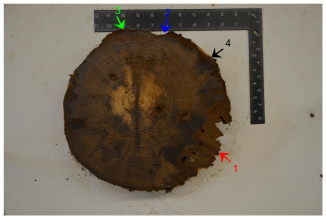

18.5 in. Below Ground

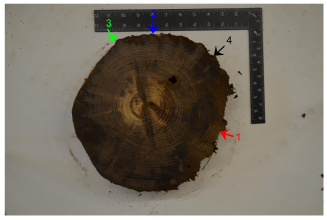

21.625 in. Below Ground

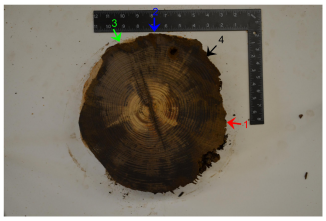

24.5 in. Below Ground

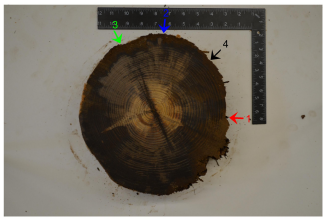

27.5 in. Below Ground

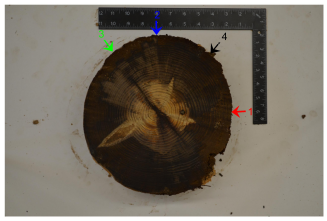

30.875 in. Below Ground

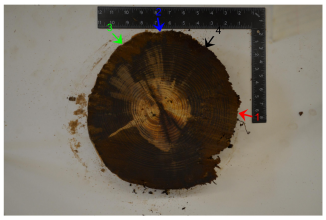

33.625 in Below Ground

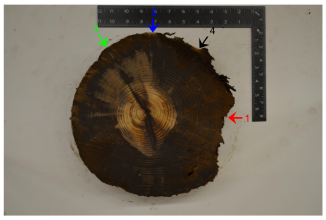

36.75 in. Below Ground

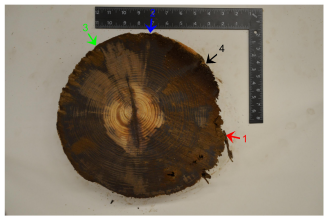

39.625 in. Below Ground

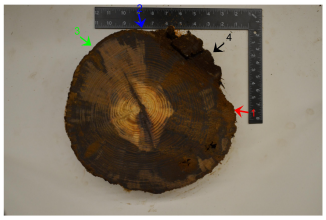

42.5 in. Below Ground

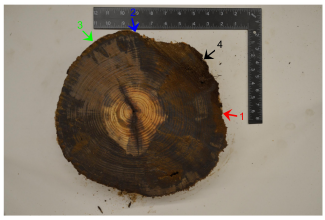

45.5 in. Below Ground

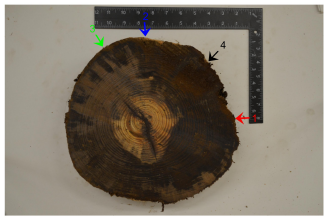

48.5 in. Below Ground

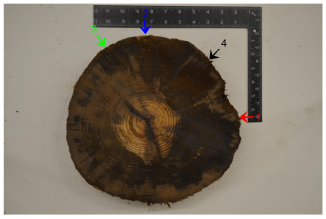

51.5 in. Below Ground

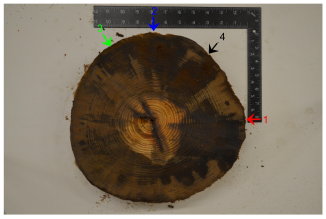

54.5 in. Below Ground

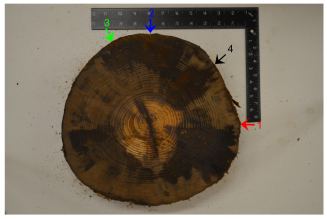

57.5 in. Below Ground

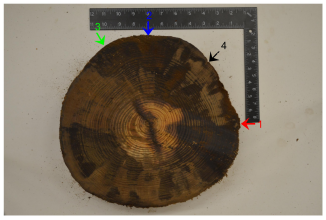

60.5 in. Below Ground

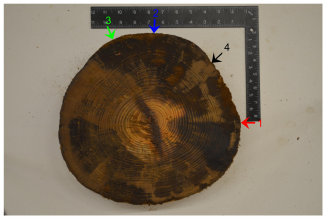

63 in. Below Ground

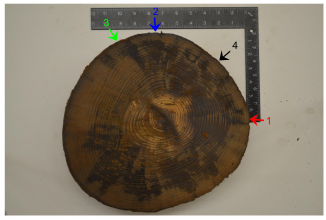

Pole 2

6 in. Above Ground	3 in. Above Ground	Ground Line
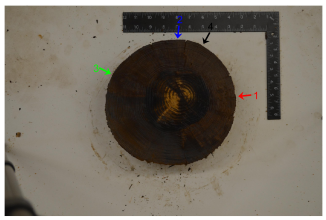	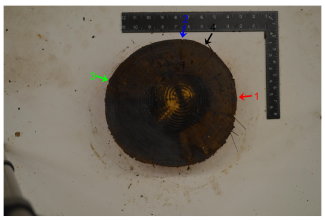	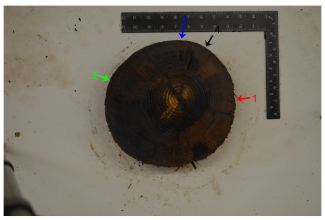
2.25 in. Below Ground	**5.25 in. Below Ground**	**8.25 in. Below Ground**
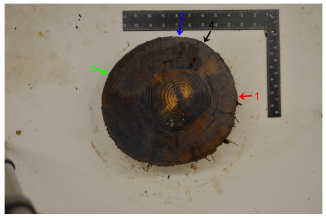	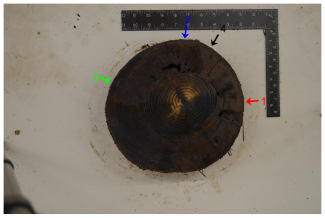	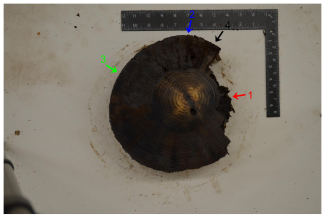
11.5 in. Below Ground	**14.5 in. Below Ground**	**17.875 in. Below Ground**
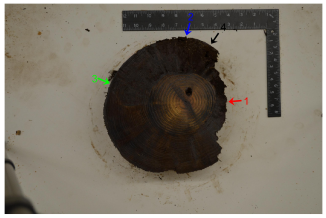	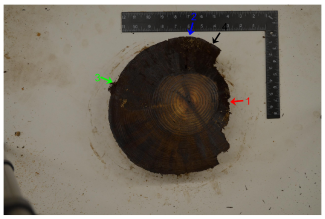	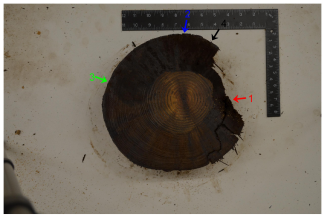
20.125 in. Below Ground	**24 in. Below Ground**	**27.125 in. Below Ground**
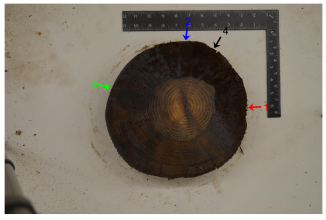	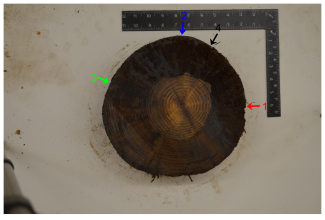	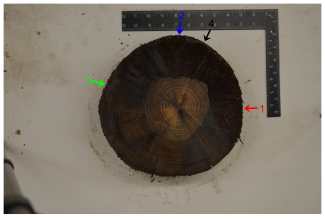

30.375 in. Below Ground

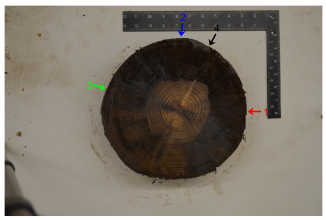

33.5 in Below Ground

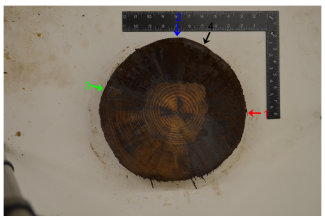

36.5 in. Below Ground

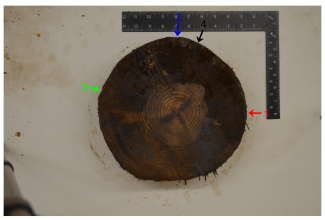

Pole 3

5 in. Above Ground

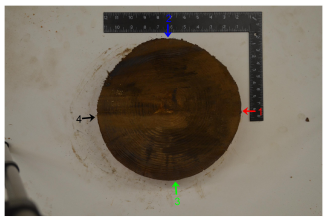

2 in. Above Ground

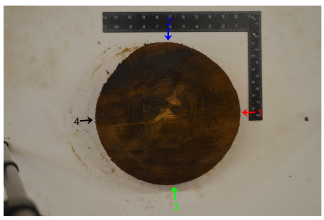

1 in. Below Ground

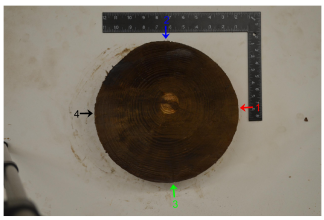

---

4 in. Below Ground

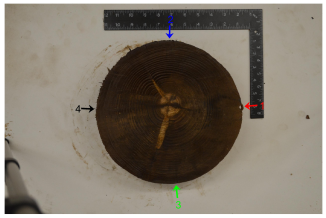

6.5 in. Below Ground

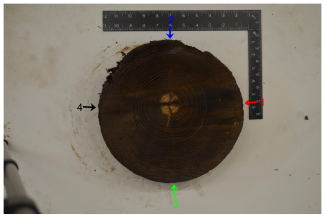

9.375 in. Below Ground

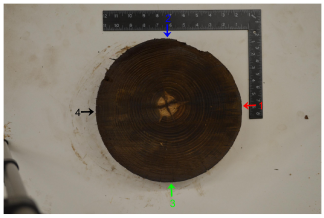

12.125 in. Below Ground

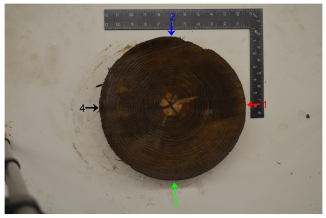

Pole 4

8.5 in. Above Ground

5.5 in. Above Ground

3 in Above Ground

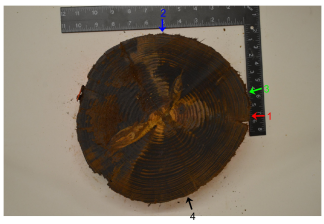

Ground Line

3.125 in. Below Ground

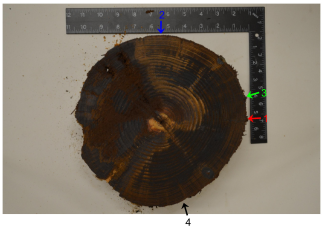

6.25 in. Below Ground

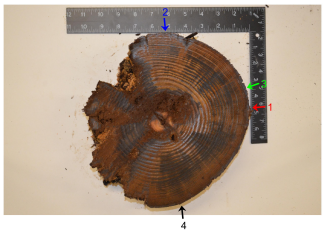

9.25 in. Below Ground

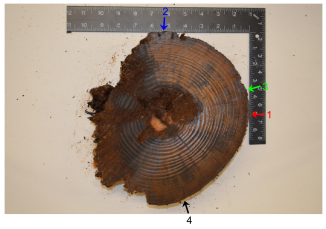

12 in. Below Ground

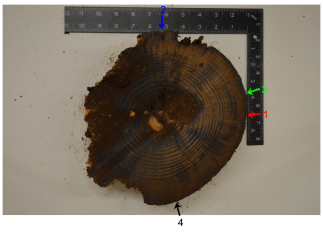

15 in. Below Ground

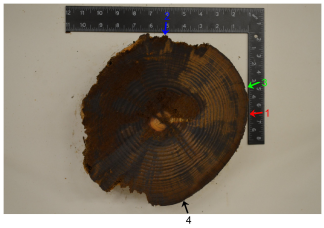

18 in. Below Ground

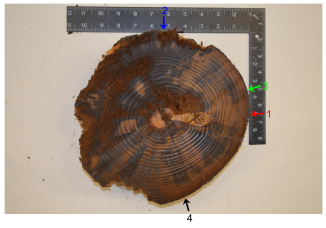

21 in. Below Ground

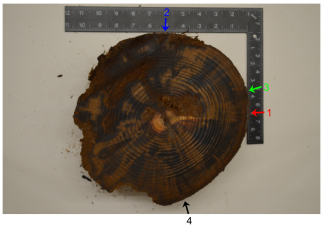

23.5 in. Below Ground

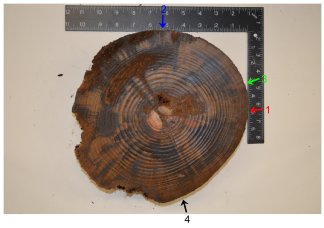

26.5 in. Below Ground

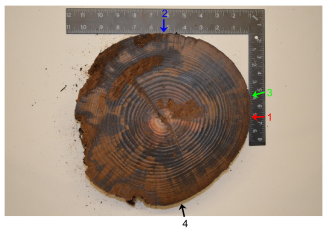

29.5 in Below Ground

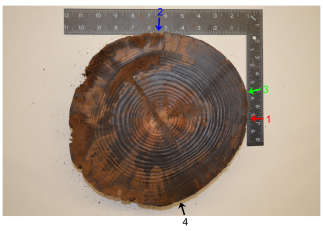

32.5 in. Below Ground

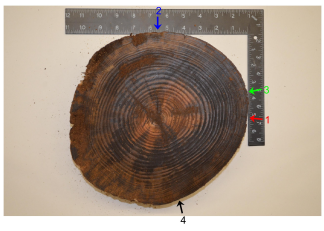

35.5 in. Below Ground

38.5 in. Below Ground

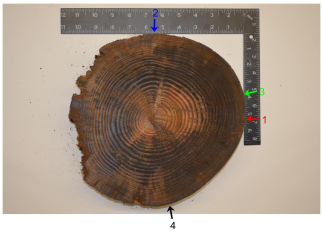

Pole 5

5.5 in. Above Ground

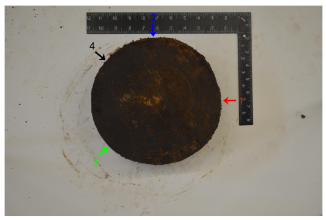

2.5 in. Above Ground

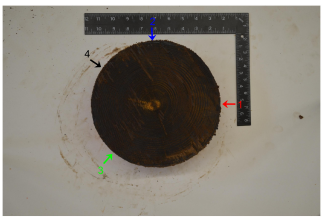

Ground Line

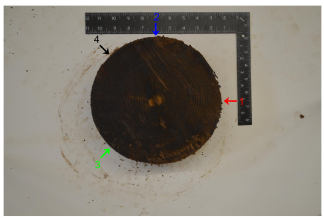

---

3 in. Below Ground

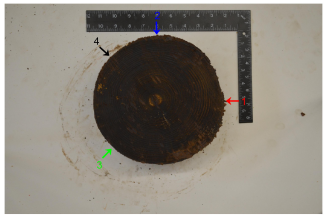

5.875 in. Below Ground

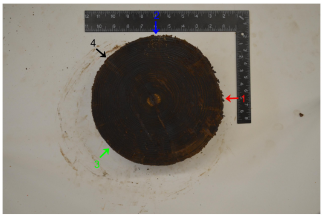

8.875 in. Below Ground

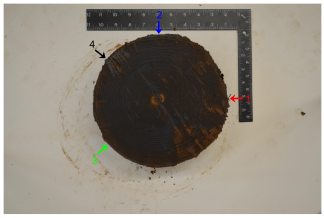

12.125 in. Below Ground

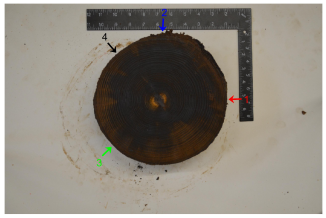

Pole 6

6.25 in. Above Ground

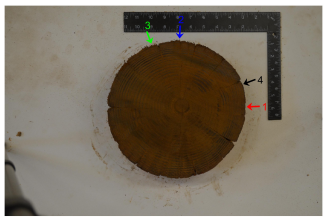

2.5 in. Above Ground

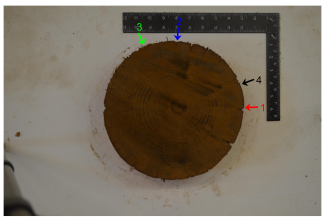

0.5 in Below Ground

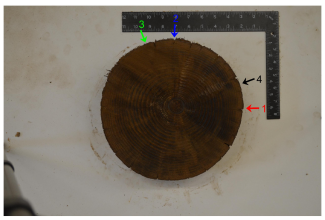

3.25 in. Below Ground

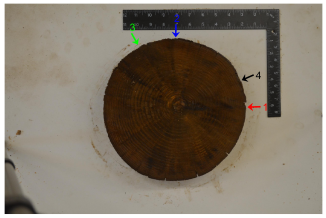

6.25 in. Below Ground

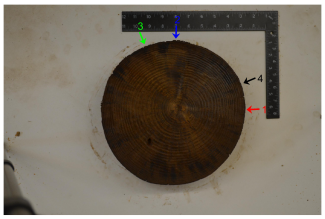

9.125 in. Below Ground

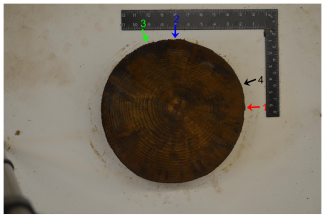

---

12 in. Below Ground

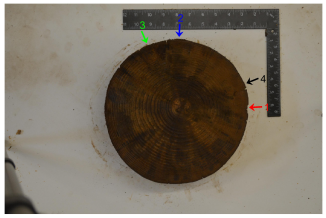

Pole 7

6 in. Above Ground

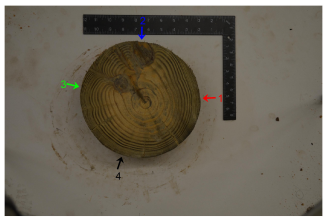

3 in. Above Ground

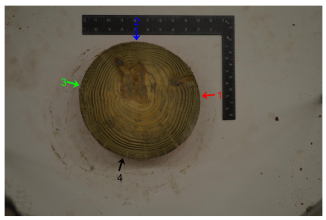

Ground Line

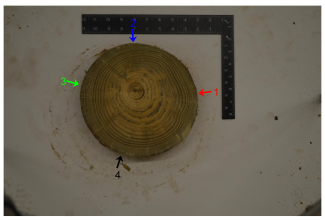

1.5 in. Below Ground

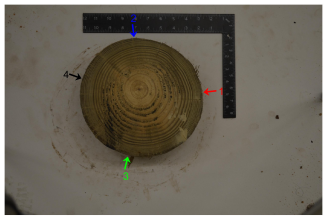

4.25 in. Below Ground

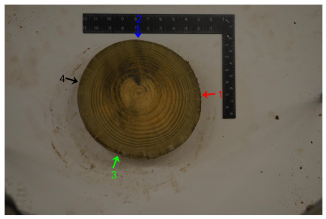

7.25 in. Below Ground

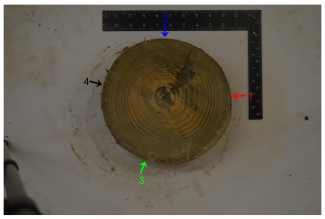

10.25 in. Below Ground

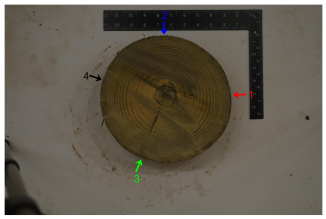

13.25 in. Below Ground

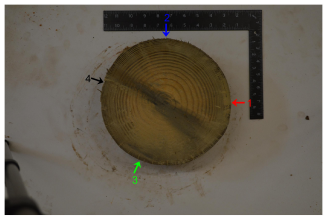

Pole 8

5.5 in. Above Ground

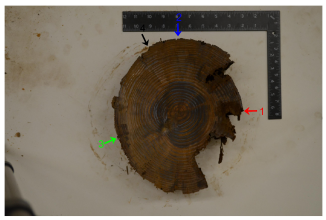

2.5 in. Above Ground

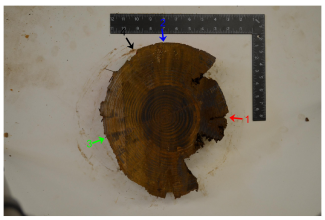

0.5 in. Below Ground

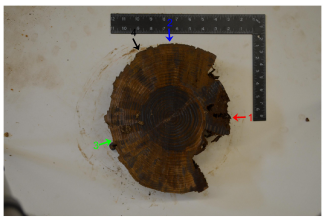

3.5 in. Below Ground

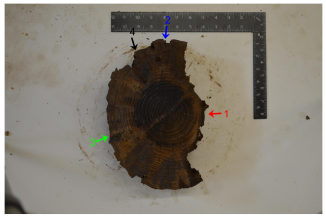

6.5 in. Below Ground

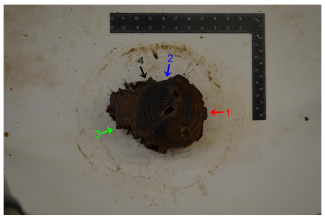

9.5 in. Below Ground

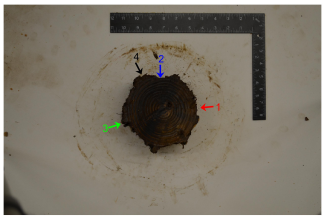

12.5 in. Below Ground

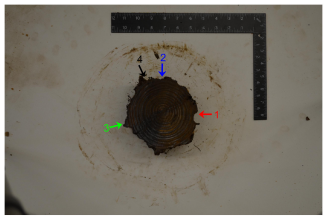

16.5 in. Below Ground

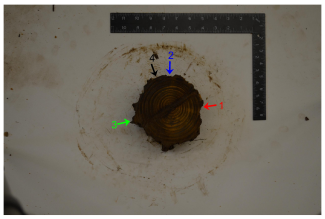

19.5 in. Below Ground

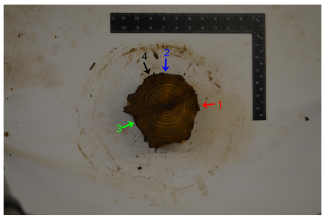

22 in. Below Ground

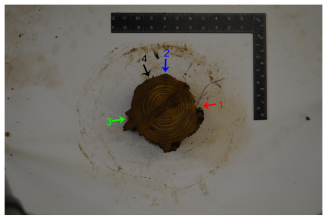

24.5 in. Below Ground

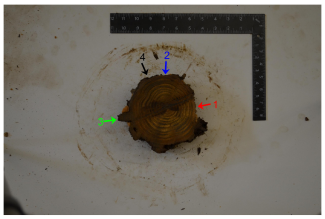

27.5 in. Below Ground

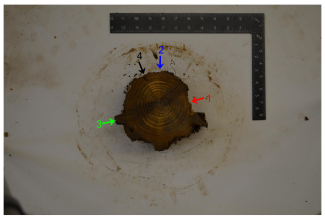

30.625 in. Below Ground

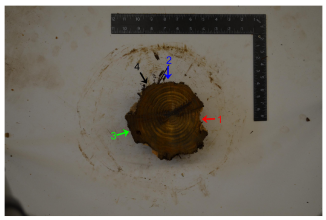

33.625 in Below Ground

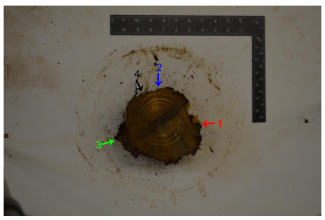

36.5 in. Below Ground

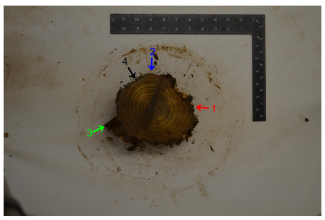

39.875 in. Below Ground

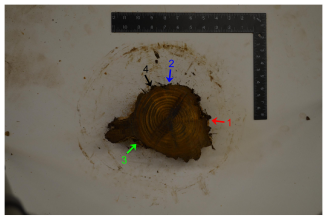

42.5 in. Below Ground

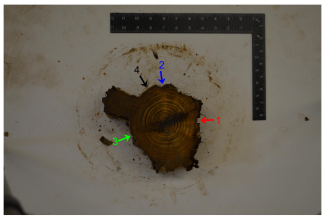

45.5 in. Below Ground

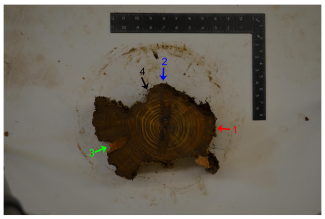

48.75 in. Below Ground

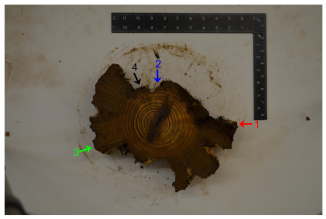

51.5 in. Below Ground

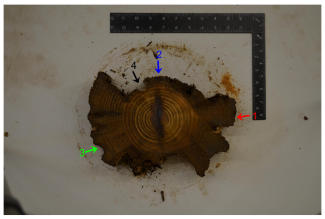

54.5 in. Below Ground

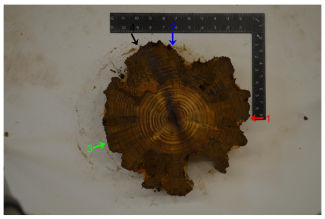

57.5 in. Below Ground

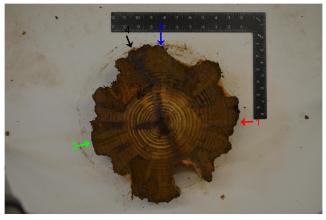

60.125 in. Below Ground

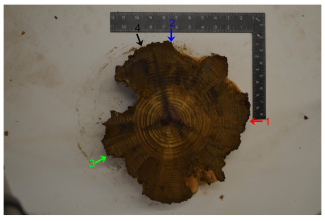

63 in. Below Ground

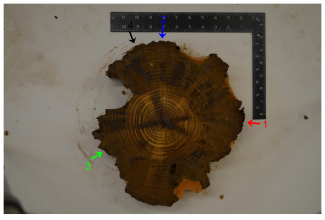

65.25 in. Below Ground

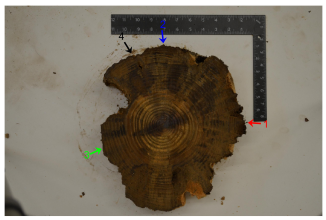

69 in Below Ground

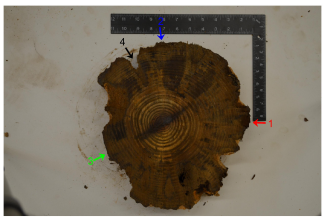

71.75 in. Below Ground

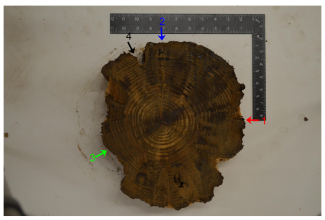

74.25 in. Below Ground

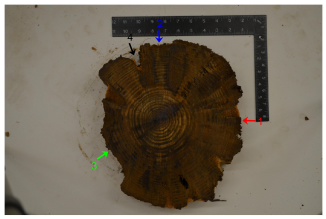

77 in. Below Ground

80 in. Below Ground

Pole 9

6 in. Above Ground

3 in. Above Ground

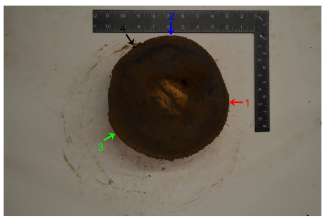

Ground Line

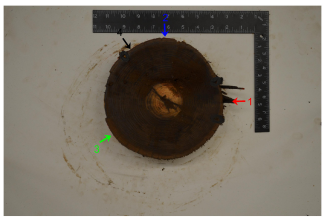

---

2 in. Below Ground

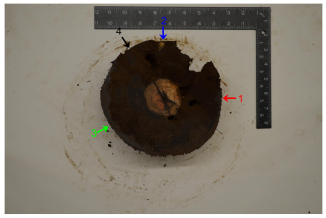

5 in. Below Ground

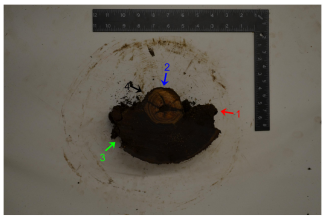

8.125 in. Below Ground

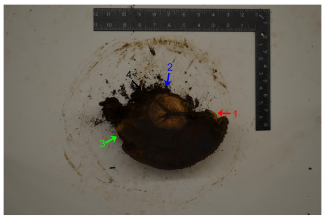

11.125 in. Below Ground

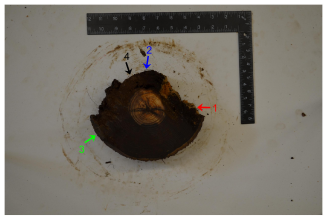

13.5 in. Below Ground

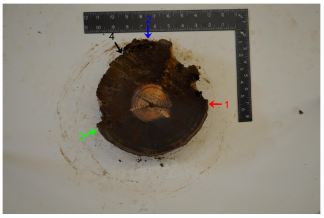

16.5 in. Below Ground

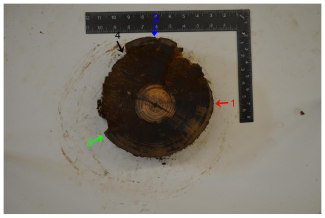

19.5 in. Below Ground

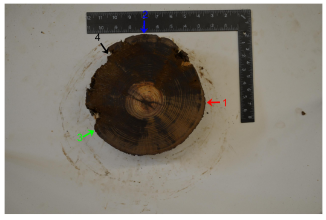

22.5 in. Below Ground

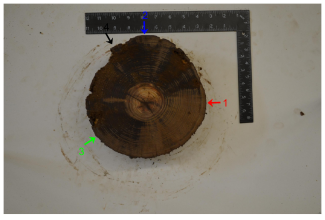

25.5 in. Below Ground

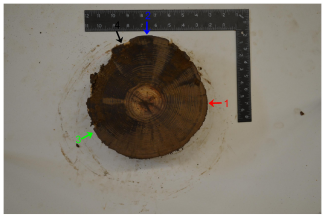

28.75 in. Below Ground

31.75 in Below Ground

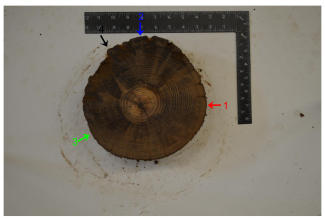

34.75 in. Below Ground

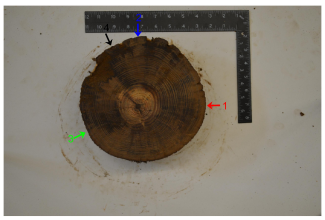

37.75 in. Below Ground

40.75 in. Below Ground

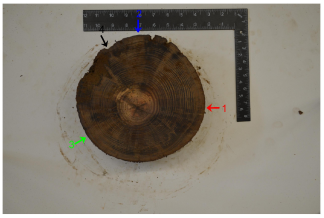

43.625 in. Below Ground

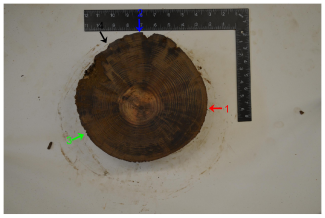

46.5 in. Below Ground

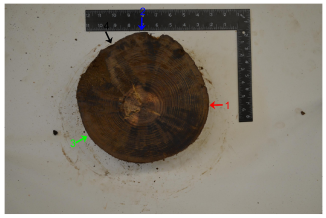

49.5 in. Below Ground

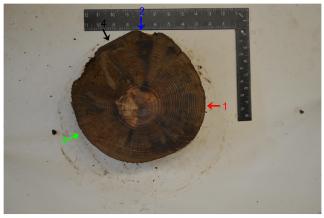

52.5 in. Below Ground

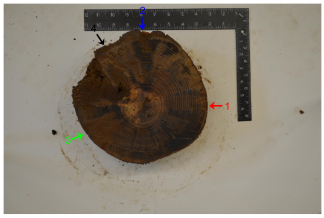

55.75 in. Below Ground

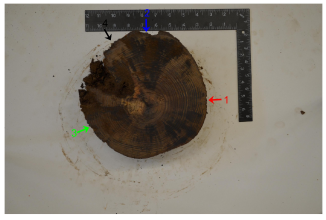

58.5 in. Below Ground

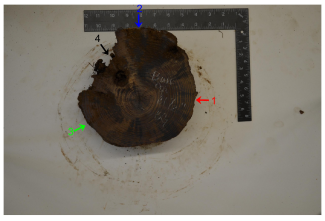

Pole 10

6 in. Above Ground

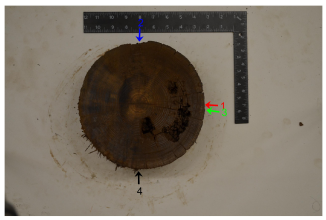

3 in. Above Ground

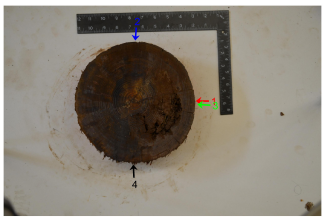

Ground Line

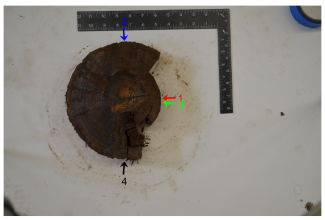

---

2 in. Below Ground

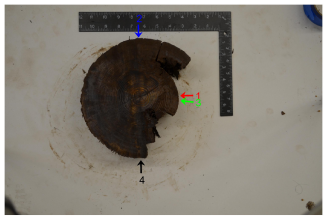

5 in. Below Ground

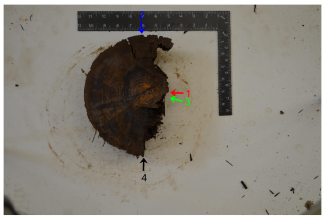

8.25 in. Below Ground

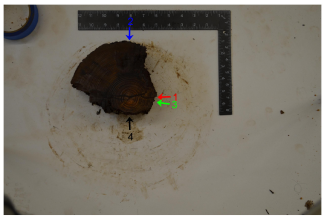

11.75 in. Below Ground

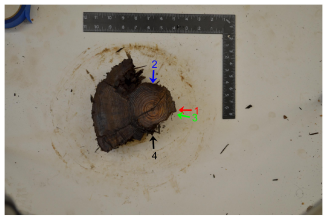

14.5 in. Below Ground

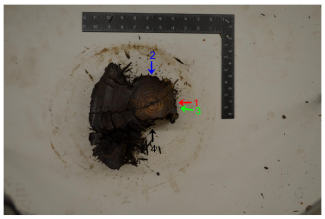

17.25 in. Below Ground

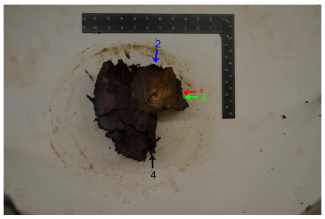

---

20 in. Below Ground

23.125 in. Below Ground

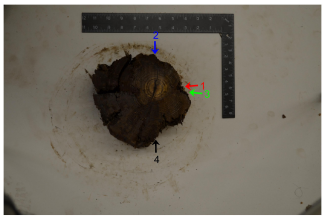

25.75 in. Below Ground

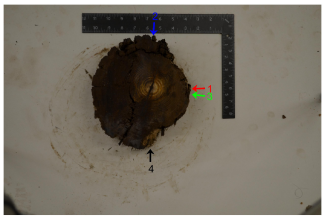

28.25 in. Below Ground

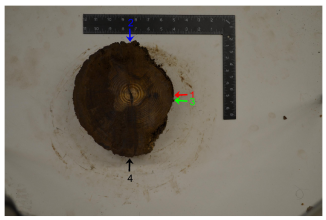

31.25 in Below Ground

34.25 in. Below Ground

37 in. Below Ground

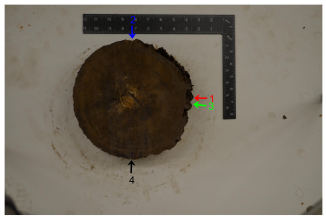

40 in. Below Ground

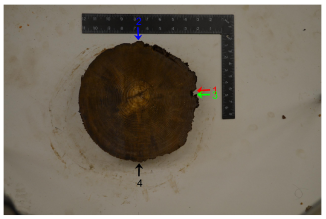

41.75 in. Below Ground

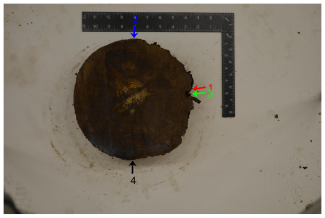

45.375 in. Below Ground

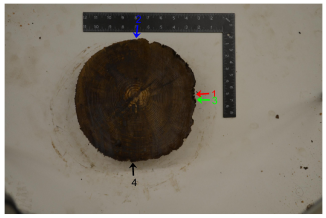

48.25 in. Below Ground

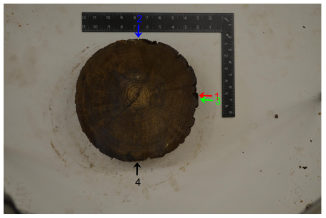

APPENDIX D : IMAGE ANALYSIS OF POLE SLICES

Pole 1

Depth	A (in^2)	d_{eff} (in)	C_{eff} (in)	I_x (in^4)	I_y (in^4)
6 in. (A.G.)	106.51	11.65	36.58	898.0	915.7
3 in (A.G.)	106.82	11.66	36.64	910.0	914.0
Ground Line	111.00	11.89	37.35	985.2	982.1
3.5 in. (B.G.)	110.11	11.84	37.20	986.9	947.9
6.5 in. (B.G.)	112.24	11.95	37.56	1039.3	969.5
9.5 in. (B.G.)	112.32	11.96	37.57	1043.8	967.1
12.5 in. (B.G.)	113.26	12.01	37.73	1049.6	995.4
15.5 in. (B.G.)	104.56	11.54	36.25	890.4	855.8
18.5 in. (B.G.)	94.57	10.97	34.47	694.0	741.4
21.625 in. (B.G.)	89.97	10.70	33.62	587.6	712.0
24.5 in. (B.G.)	92.32	10.84	34.06	629.7	733.8
27.5 in. (B.G.)	93.13	10.89	34.21	640.6	746.9
30.875 in. (B.G.)	93.11	10.89	34.21	640.1	748.7
33.625 in. (B.G.)	101.59	11.37	35.73	793.9	859.5
36.75 in. (B.G.)	108.36	11.75	36.90	944.9	929.7
39.625 in. (B.G.)	109.18	11.79	37.04	967.5	938.0
42.5 in. (B.G.)	109.22	11.79	37.05	992.6	918.6
45.5 in. (B.G.)	110.15	11.84	37.21	1000.0	941.4
48.5 in. (B.G.)	112.42	11.96	37.59	1029.0	989.6
51.5 in. (B.G.)	116.37	12.17	38.24	1102.5	1059.4
54.5 in. (B.G.)	120.73	12.40	38.95	1193.0	1134.6

Depth	A (in^2)	d_{eff} (in)	C_{eff} (in)	I_x (in^4)	I_y (in^4)
57.5 in. (B.G.)	122.34	12.48	39.21	1233.3	1158.1
60.5 in. (B.G.)	122.94	12.51	39.31	1263.2	1152.6
63 in. (B.G.)	130.23	12.88	40.45	1420.3	1292.8

Pole 2

Depth	A (in^2)	d_{eff} (in)	C_{eff} (in)	I_x (in^4)	I_y (in^4)
6.25 in. (A.G.)	74.16	9.72	30.53	455.3	421.4
3 in. (A.G.)	77.20	9.91	31.15	489.5	460.6
Ground Line	74.43	9.73	30.58	456.2	427.2
2.25 in. (B.G.)	80.32	10.11	31.77	536.7	492.2
5.25 in. (B.G.)	83.47	10.31	32.39	572.3	539.0
8.25 in. (B.G.)	74.32	9.73	30.56	390.1	514.1
11.5 in. (B.G.)	76.74	9.88	31.05	419.6	537.1
14.5 in. (B.G.)	76.26	9.85	30.96	405.5	541.5
17.875 in. (B.G.)	82.03	10.22	32.11	518.4	574.3
20.125 in. (B.G.)	88.62	10.62	33.37	641.9	610.5
24” BG	88.62	10.62	33.37	640.3	608.6
27.125 in. (B.G.)	90.88	10.76	33.79	667.5	649.2
30.375 in. (B.G.)	91.91	10.82	33.98	689.6	656.7
33.5 in. (B.G.)	93.24	10.90	34.23	706.1	679.1
36.5 in. (B.G.)	95.85	11.05	34.71	751.3	713.0

Pole 3

Depth	A (in^2)	d_{eff} (in)	C_{eff} (in)	I_x (in^4)	I_y (in^4)
5 in. (A.G.)	87.20	10.54	33.10	612.8	598.4
2 in. (A.G.)	88.72	10.63	33.39	634.4	619.4
1 in. (B.G.)	88.12	10.59	33.28	627.6	608.9
4 in. (B.G.)	90.61	10.74	33.74	663.0	644.2
6.5 in. (B.G.)	89.99	10.70	33.63	658.9	631.1
9.375 in. (B.G.)	91.07	10.77	33.83	676.1	645.1
12.125 in. (B.G.)	91.52	10.80	33.91	685.4	649.2

Pole 4

Depth	A (in^2)	d_{eff} (in)	C_{eff} (in)	I_x (in^4)	I_y (in^4)
5.5 in. (A.G.)	77.44	9.93	31.19	485.1	472.4
3 in. (A.G.)	81.03	10.16	31.91	527.8	519.8
Ground Line	80.41	10.12	31.79	514.9	517.5
3.125 in. (B.G.)	79.63	10.07	31.63	499.5	512.7
6.25 in. (B.G.)	74.07	9.71	30.51	412.4	475.2
9.25 in. (B.G.)	71.74	9.56	30.03	387.7	448.7
12 in. (B.G.)	74.88	9.76	30.68	439.5	466.3
15 in. (B.G.)	76.45	9.87	30.99	475.8	465.7
18 in. (B.G.)	79.67	10.07	31.64	524.6	494.5
21 in. (B.G.)	80.95	10.15	31.90	538.9	512.0
23.5 in. (B.G.)	82.61	10.26	32.22	556.1	537.2
26.5 in. (B.G.)	83.75	10.33	32.44	566.2	556.1
29.5 in. (B.G.)	86.61	10.50	32.99	616.4	584.1
32.5 in. (B.G.)	86.35	10.49	32.94	615.0	578.5
35.5 in. (B.G.)	86.98	10.52	33.06	625.7	586.5
38.5 in. (B.G.)	83.33	10.30	32.36	553.5	558.6

Pole 5

Depth	A (in^2)	d_{eff} (in)	C_{eff} (in)	I_x (in^4)	I_y (in^4)
5.5 in. (A.G.)	68.36	9.33	29.31	380.2	364.0
2.5 in. (A.G.)	67.66	9.28	29.16	370.8	358.1
Ground Line	68.22	9.32	29.28	378.6	362.5
3 in. (B.G.)	69.53	9.41	29.56	389.1	380.9
5.875 in. (B.G.)	70.36	9.47	29.74	397.0	391.5
8.875 in. (B.G.)	73.96	9.70	30.49	439.5	431.6
12.125 in. (B.G.)	72.08	9.58	30.10	418.1	410.3

Pole 6

Depth	A (in^2)	d_{eff} (in)	C_{eff} (in)	I_x (in^4)	I_y (in^4)
6.25 in. (A.G.)	84.21	10.35	32.53	569.4	559.9
2.5 in. (A.G.)	86.93	10.52	33.05	604.3	599.3
0.5 in. (B.G.)	90.52	10.74	33.73	655.6	649.3
3.25 in. (B.G.)	91.25	10.78	33.86	663.2	662.4
6.25 in. (B.G.)	93.30	10.90	34.24	689.5	696.5
9.125 in. (B.G.)	93.18	10.89	34.22	689.6	692.6
12 in. (B.G.)	93.78	10.93	34.33	695.4	704.9

Pole 7

Depth	A (in^2)	d_{eff} (in)	C_{eff} (in)	I_x (in^4)	I_y (in^4)
6 in. (A.G.)	65.57	9.14	28.70	351.5	333.7
3 in. (A.G.)	68.18	9.32	29.27	380.1	360.6
Ground Line	62.89	8.95	28.11	326.7	303.7
1.5 in. (B.G.)	68.68	9.35	29.38	389.8	362.1
4.25 in. (B.G.)	69.66	9.42	29.59	401.8	371.8
7.25 in. (B.G.)	69.60	9.41	29.57	401.0	371.1
10.25 in. (B.G.)	71.20	9.52	29.91	416.1	391.5
13.25 in. (B.G.)	70.46	9.47	29.76	405.3	385.6

Pole 8

Depth	A (in^2)	d_{eff} (in)	C_{eff} (in)	I_x (in^4)	I_y (in^4)
5.5 in. (A.G.)	78.86	10.02	31.48	411.0	656.2
2.5 in. (A.G.)	80.98	10.15	31.90	420.7	698.7
0.5 in. (B.G.)	79.14	10.04	31.54	392.9	676.6
3.5 in. (B.G.)	64.97	9.09	28.57	221.0	546.2
6.5 in. (B.G.)	31.49	6.33	19.89	108.5	60.6
9.5 in. (B.G.)	25.19	5.66	17.79	51.1	51.3
12.5 in. (B.G.)	23.32	5.45	17.12	41.4	46.7
16.5 in. (B.G.)	21.65	5.25	16.49	35.4	40.5
19.5 in. (B.G.)	22.34	5.33	16.76	38.5	42.3
22 in. (B.G.)	23.37	5.45	17.14	45.2	43.7
24.5 in. (B.G.)	25.99	5.75	18.07	56.1	54.9
27.5 in. (B.G.)	26.53	5.81	18.26	61.7	55.6
30.625 in. (B.G.)	25.74	5.73	17.99	53.5	54.5
33.625 in. (B.G.)	26.52	5.81	18.26	63.4	52.1
36.5 in. (B.G.)	27.24	5.89	18.50	72.3	51.3

Depth	A (in^2)	d_{eff} (in)	C_{eff} (in)	I_x (in^4)	I_y (in^4)
39.875 in. (B.G.)	29.54	6.13	19.27	102.9	56.0
42.5 in. (B.G.)	31.56	6.34	19.92	102.7	85.0
45.5 in. (B.G.)	44.48	7.53	23.64	267.8	114.0
48.75 in. (B.G.)	58.04	8.60	27.01	456.8	219.5
51.5 in. (B.G.)	61.09	8.82	27.71	532.3	192.3
54.5 in. (B.G.)	88.69	10.63	33.39	677.1	639.2
57.5 in. (B.G.)	91.67	10.80	33.94	681.1	709.2
60.125 in. (B.G.)	93.18	10.89	34.22	631.5	828.7
63 in. (B.G.)	97.14	11.12	34.94	665.7	923.2
65.25 in. (B.G.)	100.87	11.33	35.60	694.2	1009.4
69 in. (B.G.)	108.80	11.77	36.98	812.8	1135.5
71.75 in. (B.G.)	109.61	11.81	37.11	812.7	1166.9
74.25 in. (B.G.)	108.88	11.77	36.99	797.9	1149.8
77 in. (B.G.)	106.54	11.65	36.59	794.2	1073.4
80 in. (B.G.)	110.59	11.87	37.28	924.8	1089.8

Pole 9

Depth	A (in^2)	d_{eff} (in)	C_{eff} (in)	I_x (in^4)	I_y (in^4)
6 in. (A.G.)	51.78	8.12	25.51	211.8	215.6
3 in. (A.G.)	52.71	8.19	25.74	217.2	225.6
Ground Line	50.76	8.04	25.26	202.4	208.2
2 in. (B.G.)	48.34	7.85	24.65	200.4	178.1
5 in. (B.G.)	25.93	5.75	18.05	81.5	37.0
8.125 in. (B.G.)	29.90	6.17	19.38	117.5	49.1
11.125 in. (B.G.)	35.97	6.77	21.26	126.2	87.1
13.5 in. (B.G.)	50.60	8.03	25.22	191.8	222.6

Depth	A (in^2)	d_{eff} (in)	C_{eff} (in)	I_x (in^4)	I_y (in^4)
16.5 in. (B.G.)	53.37	8.24	25.90	212.4	246.7
19.5 in. (B.G.)	56.37	8.47	26.62	242.5	266.2
22.5 in. (B.G.)	57.60	8.56	26.90	256.0	275.2
25.5 in. (B.G.)	58.09	8.60	27.02	260.0	279.8
28.75 in. (B.G.)	59.65	8.71	27.38	274.9	293.8
31.75 in. (B.G.)	60.94	8.81	27.67	291.2	301.8
34.75 in. (B.G.)	62.97	8.95	28.13	316.7	315.8
37.75 in. (B.G.)	64.20	9.04	28.40	326.0	331.3
40.75 in. (B.G.)	65.53	9.13	28.70	345.0	339.8
43.625 in. (B.G.)	67.09	9.24	29.04	364.6	353.6
46.5 in. (B.G.)	68.37	9.33	29.31	376.4	368.9
49.5 in. (B.G.)	69.64	9.42	29.58	392.1	382.0
52.5 in. (B.G.)	69.83	9.43	29.62	392.0	387.5
55.75 in. (B.G.)	63.47	8.99	28.24	319.5	325.3
58.5 in. (B.G.)	53.77	8.27	25.99	219.3	255.7

Pole 10

Depth	A (in^2)	d_{eff} (in)	C_{eff} (in)	I_x (in^4)	I_y (in^4)
6 in. (A.G.)	66.89	9.23	28.99	352.5	359.9
3 in. (A.G.)	69.61	9.41	29.58	382.2	389.4
Ground Line	51.48	8.10	25.44	170.7	280.2
2 in. (B.G.)	54.05	8.30	26.06	208.3	293.7
5 in. (B.G.)	44.98	7.57	23.77	118.2	240.7
8.25 in. (B.G.)	26.86	5.85	18.37	64.5	55.8
11.75 in. (B.G.)	29.59	6.14	19.28	74.2	75.4
14.5 in. (B.G.)	33.44	6.52	20.50	103.0	112.7

Depth	A (in^2)	d_{eff} (in)	C_{eff} (in)	I_x (in^4)	I_y (in^4)
17.25 in. (B.G.)	36.94	6.86	21.55	107.0	134.6
20 in. (B.G.)	38.60	7.01	22.03	119.9	123.8
23.125 in. (B.G.)	38.93	7.04	22.12	127.3	118.5
25.75 in. (B.G.)	47.91	7.81	24.54	162.5	210.0
28.25 in. (B.G.)	52.07	8.14	25.58	187.7	251.2
31.25 in. (B.G.)	60.41	8.77	27.55	279.8	304.4
34.25 in. (B.G.)	63.24	8.97	28.19	315.3	324.4
37 in. (B.G.)	67.08	9.24	29.03	361.3	356.1
40 in. (B.G.)	67.07	9.24	29.03	359.6	357.7
41.75 in. (B.G.)	69.28	9.39	29.51	379.2	386.5
45.375 in. (B.G.)	71.94	9.57	30.07	409.0	415.9
48.25 in. (B.G.)	72.56	9.61	30.20	419.2	419.6

Pole 1

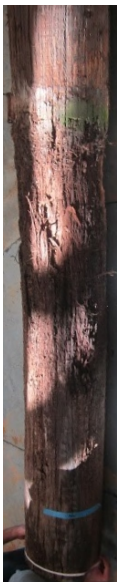

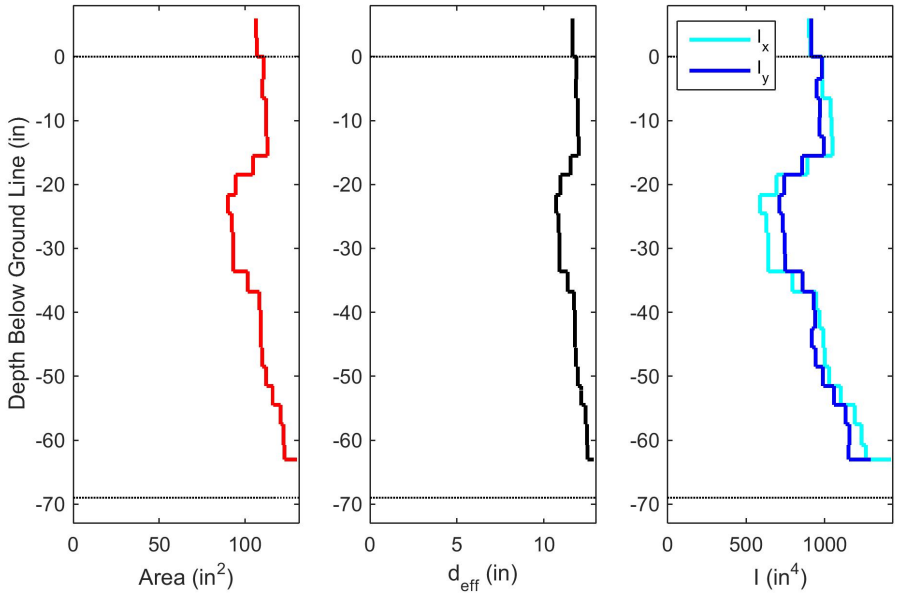
Depth Below Ground Line (in)
0
-10
-20
-30
-40
-50
-60
-70
0
50
100
Area (in^2)
0
5
10
d_{eff} (in)
0
500
1000
I (in^4)
I_x
I_y

Pole 2

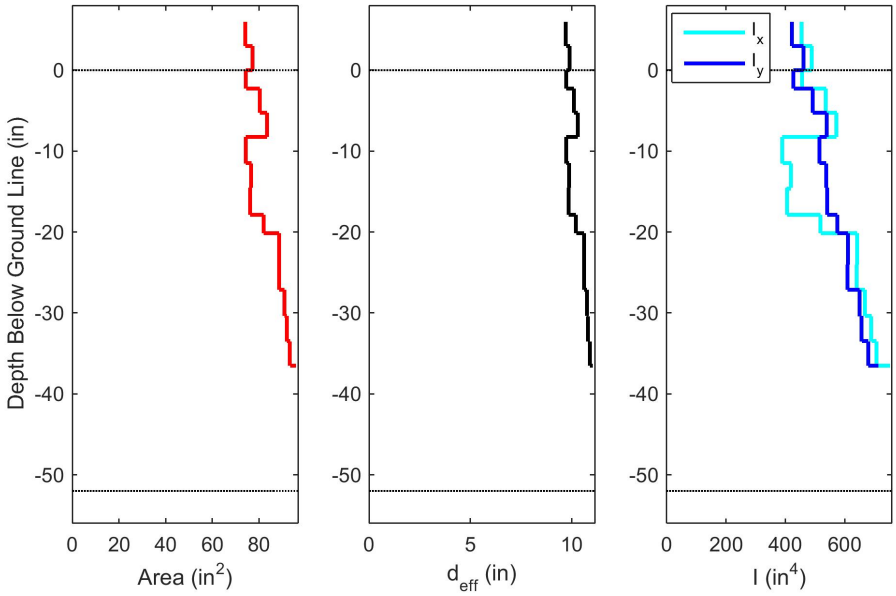
Depth Below Ground Line (in)
0
-10
-20
-30
-40
-50
0
20
40
60
80
Area (in^2)
0
5
10
d_{eff} (in)
0
200
400
600
I (in^4)
I_x
I_y

Pole 3

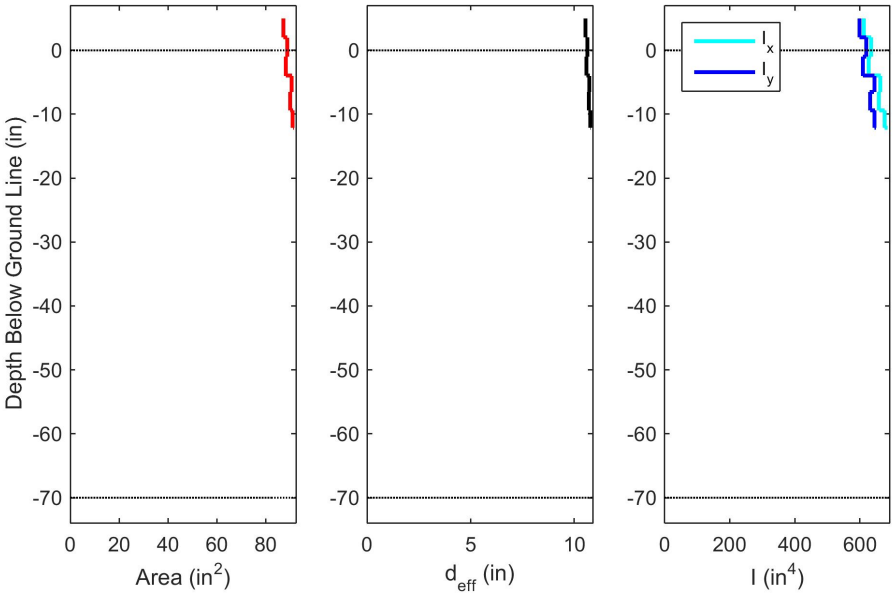
Depth Below Ground Line (in)
0
-10
-20
-30
-40
-50
-60
-70
0 20 40 60 80
Area (in^2)
0 5 10
d_{eff} (in)
0 200 400 600
I (in^4)
I_x
I_y

Pole 4

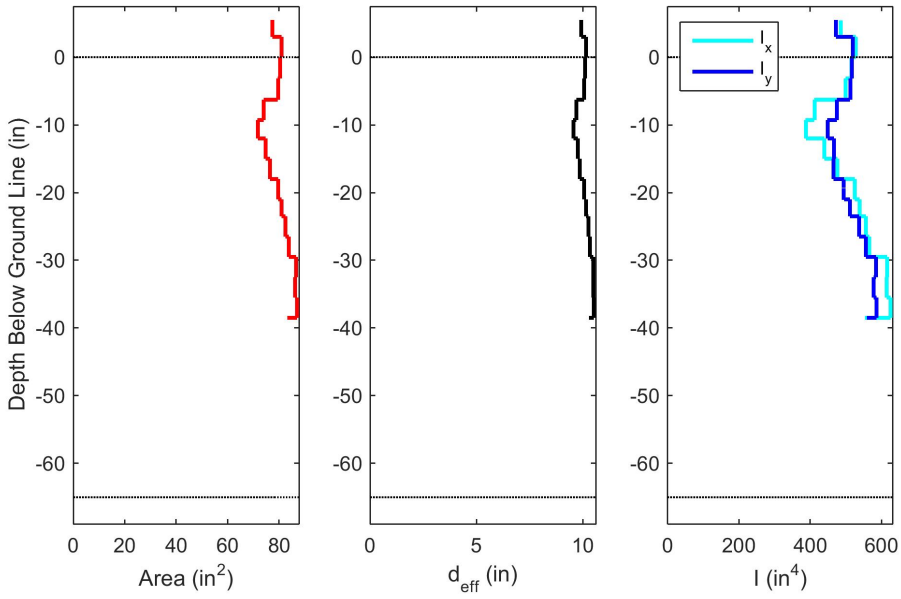
Depth Below Ground Line (in)
0
-10
-20
-30
-40
-50
-60
0 20 40 60 80
Area (in^2)
0 5 10
d_{eff} (in)
0 200 400 600
I (in^4)
I_x
I_y

Pole 5

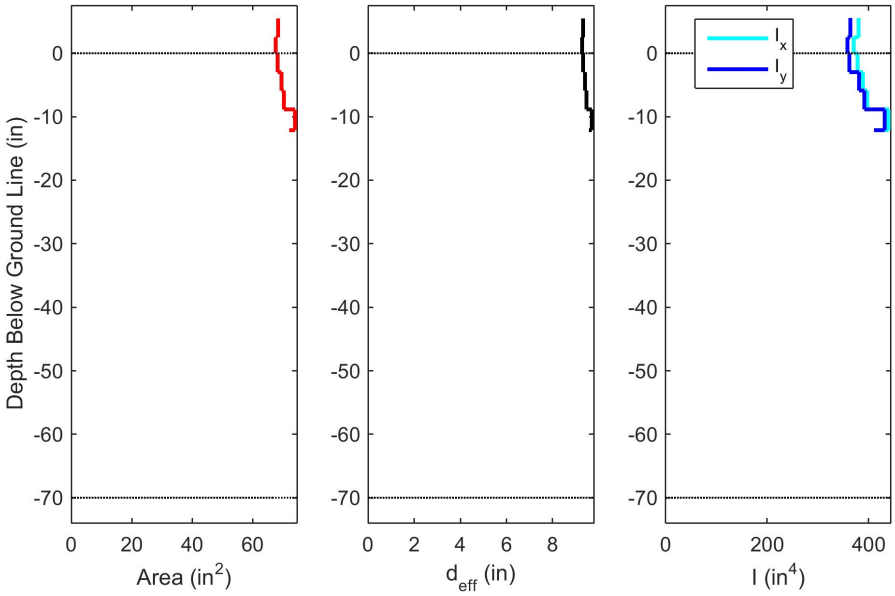
Depth Below Ground Line (in)
0
-10
-20
-30
-40
-50
-60
-70
0
20
40
60
Area (in^2)
0
2
4
6
8
d_{eff} (in)
0
200
400
I (in^4)
I_x
I_y

Pole 6

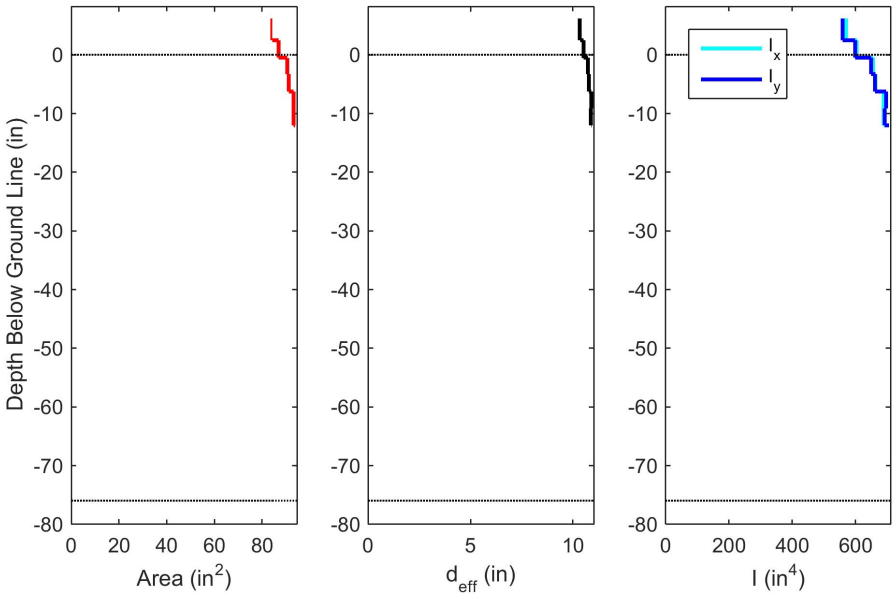
Depth Below Ground Line (in)
0
-10
-20
-30
-40
-50
-60
-70
-80
0
20
40
60
80
Area (in^2)
0
5
10
d_{eff} (in)
0
200
400
600
I (in^4)
I_x
I_y

Pole 7

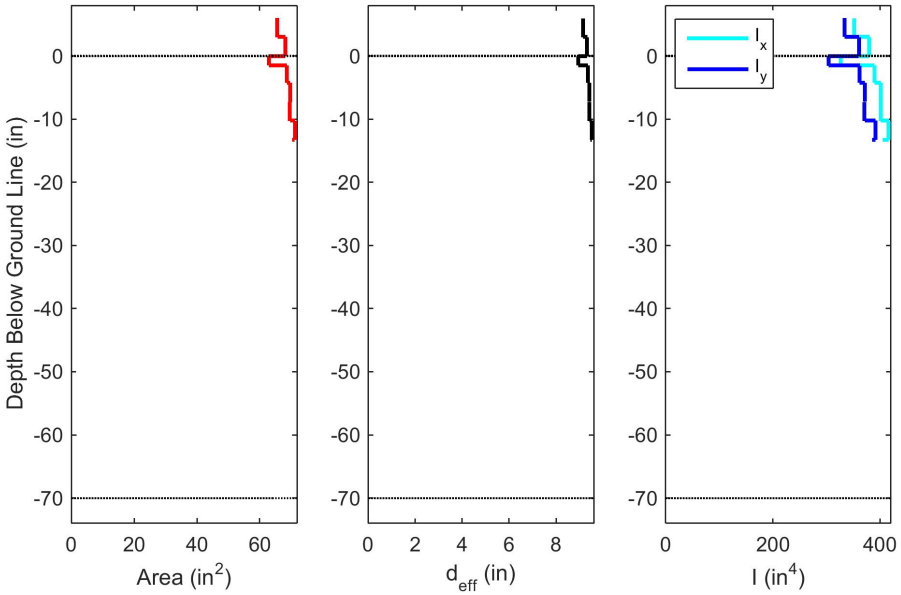
Depth Below Ground Line (in)
0
-10
-20
-30
-40
-50
-60
-70
0
20
40
60
Area (in^2)
0
2
4
6
8
d_{eff} (in)
0
200
400
I (in^4)
I_x
I_y

Pole 8

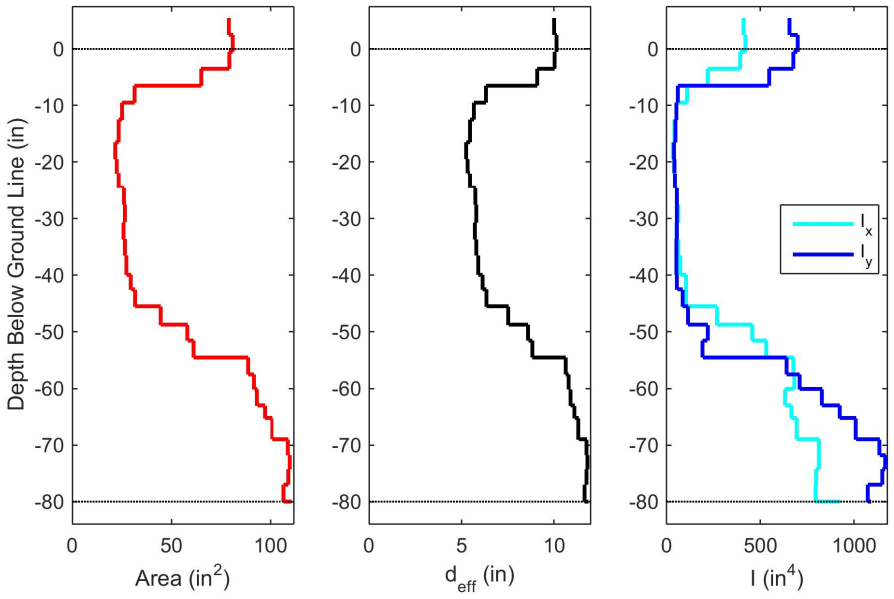
Depth Below Ground Line (in)
0
-10
-20
-30
-40
-50
-60
-70
-80
0
50
100
Area (in^2)
0
5
10
d_{eff} (in)
0
500
1000
I (in^4)
I_x
I_y

Pole 9

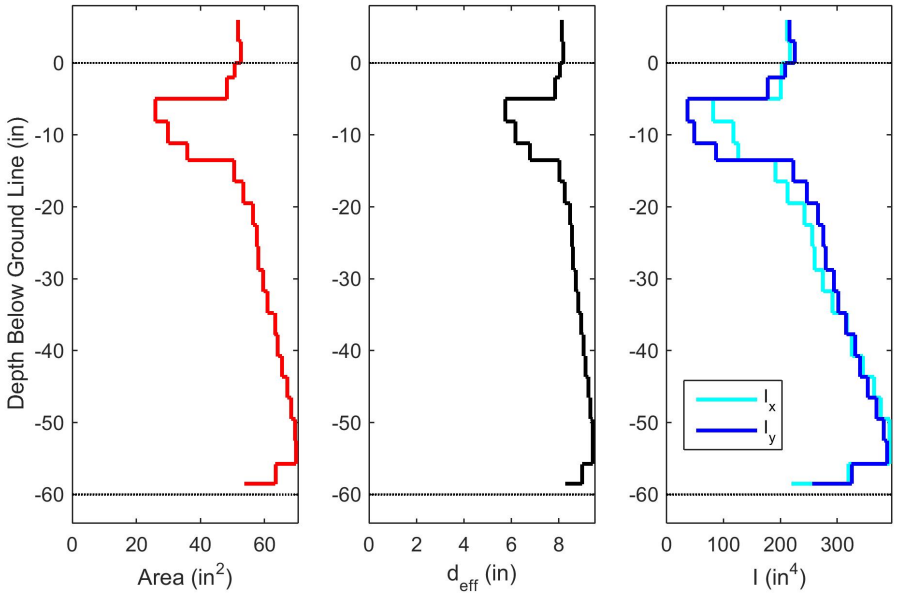

Pole 10